CREEP AND EROSION RESISTANCE OF NITRIDE BASED NANOSTRUCTURED COATINGS DEPOSITED BY CATHODIC ARC

BY

NESTOR KODZO ANKAH

A Thesis Presented to the
DEANSHIP OF GRADUATE STUDIES

KING FAHD UNIVERSITY OF PETROLEUM & MINERALS
DHAHRAN, SAUDI ARABIA

In Partial Fulfillment of the
Requirements for the Degree of

MASTER OF SCIENCE

In

MATERIALS SCIENCE & ENGINEERING

MAY, 2015

KING FAHD UNIVERSITY OF PETROLEUM & MINERALS

DHAHRAN- 31261, SAUDI ARABIA

DEANSHIP OF GRADUATE STUDIES

This thesis, written by **NESTOR KODZO ANKAH** under the direction of his thesis advisor and approved by his thesis committee, has been presented and accepted by the Dean of Graduate Studies, in partial fulfillment of the requirements for the degree of **MASTER OF SCIENCE IN MATERIALS SCIENCE & ENGINEERING.**

Dr. Zuhair Mattoug Gasem
(Advisor)

Dr. Zuhair Mattoug Gasem
Department Chairman

Bekir Sami Yilbas

Dr. Bekir Sami Yilbas
(Member)

Dr. Salam A. Zummo
Dean of Graduate Studies

Dr. Mohammed Abdul Samad
(Member)

30/7/2015
Date

Dedicated to my mother, Bertha Ankah, my wife, Mawutor Hoenyekor, my children, Seyram and Kafui Ankah, my siblings and to the memory of my beloved father, Pius Yao Ankah.

ACKNOWLEDGMENTS

My first and foremost thanks go to Almighty God for his constant protection, love, guidance, strength, wisdom and understanding. To my advisor, Dr. Zuhair Mattoug Gasem, who provided me with the privilege and opportunity to work on this fascinating project. Without his guidance and insight, the results presented in this thesis could not have been obtained. My profound gratitude also to Professor Bekir Sami Yilbas and Dr. Abdul Samad Mohammad, for contributing their invaluable time in providing additional intellectual guidance as committee members. I would like to acknowledge and thank the National Science, Technology & Innovation Plan (NSTIP), of King Fahd University of Petroleum & Minerals for funding this work. I thank Mr. Hakeem Adesina for providing me with many insightful discussions and collaborations, to Mr. Lateef Hashmi and Mr. Ali Sadaqat for their assistance during my lab work. Special thanks to my mother, brothers, and sisters and the Ghanaian community in KFUPM for their friendship, help and moral support all this while. Finally, I would like to thank my wife, Mawutor and my children, Seyram and Kafui, for their love, patience, understanding, and inspiration. They provided me with a life outside of school and their continued support has been crucial to the successful completion of my degree.

TABLE OF CONTENTS

LIST OF TABLES

LIST OF FIGURES

THESIS ABSTRACT

NAME:	Nestor Kodzo Ankah
TITLE OF STUDY:	Creep and Erosion Resistance of nitride based nanostructured coatings deposited by cathodic arc
MAJOR FIELD:	Materials Science & Engineering
DATE OF DEGREE:	May, 2015

CrN, TiN, CrAlN and TiAlN coatings were deposited on AISI 304 stainless steel substrate using cathodic arc evaporation. Cr and Ti (99.99%) targets were used to deposit the binary coatings while 70Cr-30Al at.% and 45Ti-55Al at.% targets were used to deposit the ternary coatings. Scanning electron microscopy (SEM) and X-ray diffraction (XRD) were used to characterize the microstructure and phases present. Several mechanical and tribological properties of the coatings were evaluated including: scratch resistance, coefficient of friction, microhardness, indentation creep, and erosion. The average thickness of the coatings was approximately 1.8 μm. The hardness of the coatings ranged between 1230 HV for CrN to 2400 HV for CrAlN. TiN and CrN exhibited higher resistance to scratch compared to their counterpart ternary coatings. The predominant failure mechanism during *scratch test was tensile cracking for CrN, TiN and CrAlN while it was conformal cracking for TiAlN. The creep parameters of the nitride coatings were evaluated at* 50^oC*,* 75^oC*, and* 100^oC *with 60 seconds dwell time. The activation energies for CrN, TiN, CrAlN, and TiAlN coatings were* 10,16,21,*and* 17 kJ/mol*, respectively. Erosion resistance of the coatings was investigated using the incremental mass loss for four impingement angles:* 30^o*,* 45^o*,* 60^0*, and* 90^0*. The results indicated that ternary nitride coatings exhibited higher resistance to erosion as compared to the binary counterparts for all attack angles. TiN, CrAlN and TiAlN coatings exhibited relatively low erosion rates whereas CrN coating showed higher erosion rate under similar testing conditions. The predominant erosion mechanism observed in the coatings was plastic deformation with indentation cutting for all attack angles. The erosion performance showed good correlation with coating parameters (hardness and* H^3/E^2*).*

ملخص الرسالة

الاسم الكامل: نيستو انكا كوزو

عنوان الرسالة: زحف تآكل والمقاومة من نيتريد استنادا الطلاء ذات البنية النانومترية التي أودعتها قوس الكاثودية

التخصص: قسم علوم وهندسة المواد

تاريخ الدرجة العلمية: مايو, 2015

هدفت هذه الرسالة لدراسة خصائص طلاءات مرسبة بطريقة البخار الفيزيائي بواسطة تقنية (cathodic arc) على عينات من الحديد الغير قابل للصدأ. شملت الدراسة طلاءات ثنائية من تفاعل النيتروجين مع الكروم والتايتنيوم (CrN, TiN) وثلاثية من تفاعل النيتروجين والألمنيوم مع الكروم والتايتنيوم (TiAlN , CrAlN). استخدم في عملية الطلاء الثنائي كاثود بدرجة نقاوة 99.99% من Ti ,Cr اما في عملية الطلاء الثلاثيى فقد استخدم (Cr30Al70 و Ti55Al45) كنسب ذرية.
استخدم في هذه الدراسة المجهر الإلكتروني (SEM) و الأشعة السينية (XRD) لمعرفة المركب المجهري ومعرفة الطور. العديد من الخصائص الميكانيكية والاحتكاك تم دراستها في هذا البحث مثل مقاومة الخدش، ومعامل الاحتكاك، والصلادة والتآكل الجاف.
كان متوسط سمك الطلاءات ما يقرب من 1.8 ميكرون. اما بالنسبة لصلابة الطلاءات فكانت ما بين صلابة (CrN) HV1230 وصلابة (CrAlN) HV 2400. أظهرت هذه الدراسة ان طلاءات (TiN و CrN) افضل في مقاومة الخدش من الطلاءات الثلاثية (TiAlN , CrAlN). كما أشارت النتائج أن الخدش في طلاءات (CrN, TiN) هو خدش بسبب الشد بينما الخدش في طلاء (CrAlN) هو خدش بسبب الضغط. نتائج اختبارات مقاومة الإنسياب الحراري (creep) عند درجة حرارة 50 ,75, و100 درجة مئوية بينت أن طاقات التنشيط الخاصة بطلاءات CrN و TiN و CrAlN وTiAlN كانت على النحو التالي 10, 16, 21 و 17 kJ/mol. مقاومة التآكل الجاف (Erosion) تم اختبارها بواسطة فقدان الوزن الناتج عن اصطدام حبيبات صلبة مع سطوح الطلاءات عند أربع زوايا هجومية 30 , 45 , 60 و 90 درجة. أظهرت النتائج ان الطلاءات الثلاثية كانت أفضل مقاومة للتآكل مقارنة بالطلاءات الثنائية عند كل الزوايا في ظل ظروف اختبار مماثلة. أظهر أداء التآكل علاقة جيدة مع خصائص الطلاءات (H^3 / E^2).

CHAPTER 1

INTRODUCTION

Nitride based coatings were first used on cutting tools as wear resistant coatings to reduce the wear rate and hence prolong tool life. These nitrides are brittle, and vulnerable to fracture when used on their own. However, when applied as thin film on to a substrate such as stainless steel, they lose their brittleness and conforms to the toughness of the substrate. As a result, various entities such as the military, academic and research institutions are undertaking extensive research into nitride based coatings.

Manufacturers of metallic components such as compressor and turbine blades are experimenting with coatings in an attempt to prolong the lifespan of their compressor blades operating in particulate laden environments. These nitride coatings are usually deposited at low temperatures using physical vapor deposition(PVD). PVD is a process in which a target metal is evaporated or sputtered onto another metal to be protected known as the substrate. For atoms to be dislodged from the target metal, enough kinetic or thermal energy needs to be supplied. The dislodged atoms are subsequently transported from the target to the substrates in a controlled low pressure atmosphere containing either reactive or non-reactive gases. In this technique, coatings can be deposited at temperatures that are relatively low thereby producing metastable phases that provide unique and desirable properties.

The commonly used techniques to deposit nitride based coatings are electron beam evaporation, cathodic arc evaporation, and magnetron sputtering. In addition to the common PVD techniques, ion beam techniques such as ion implantation and ion beam assisted deposition have also been used to deposit hard nitride coatings [1]. Another deposition technique, chemical vapor deposition (CVD), can also be used to grow hard nitride coatings, but this technique requires higher deposition temperatures making it difficult to coat temperature sensitive substrates.

Cathodic arc evaporation will be the focus of this study.

1.1 Motivation

Nitride coatings have been widely used in many industrial applications especially in aerospace, automotive, energy and machine tools. The aerospace industry is increasingly faced with constant erosion and corrosion of compressor blades as illustrated in Figure 1.1 . Solid particle damage commonly encountered when operating in arid environments. This menace frequently leads to decreased efficiency, reduced power and reduced availability culminating in increased fuel consumption and cost of maintenance of the aircraft engines.

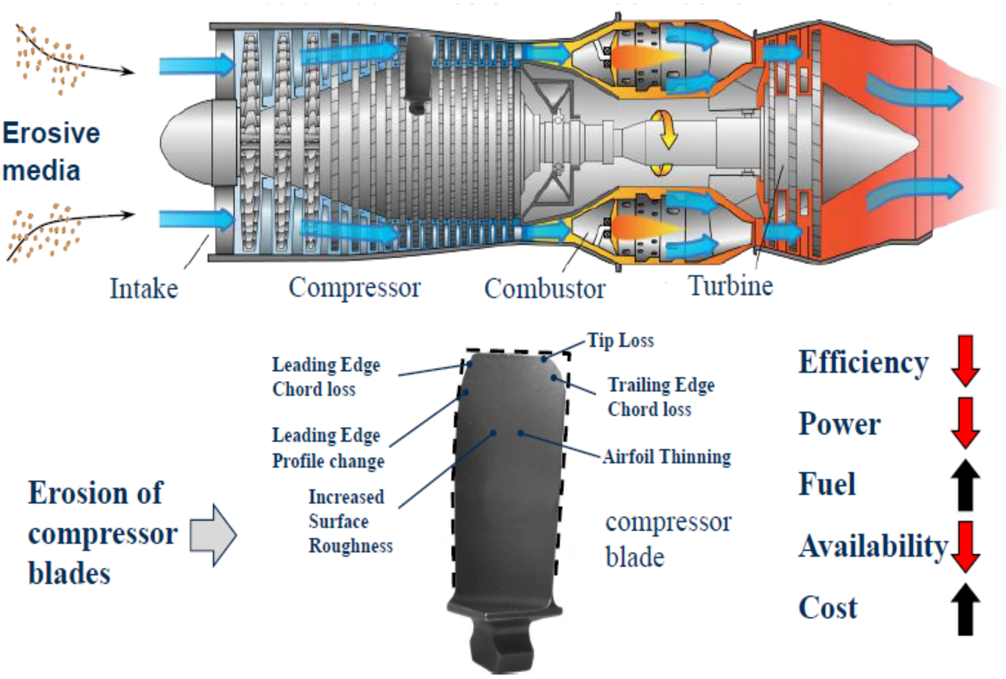

Figure 1.1: Aircraft gas turbine engine showing the effect of erosion on compressor blade.[2]

The quest to produce high performance and lightweight materials by the aerospace industry led to extensive research into thin films and surface coatings in recent times. The application in harsh environments require materials with excellent tribological and mechanical properties.

Nitride based coatings can enhance many of these desired properties without recourse to composition modification of the base material. Hard coatings are being employed in many applications, however there is a great demand for improved mechanical properties and high erosion resistances as observed in Figure 1.2, where the structural integrity of the coated blade was intact even after 40 months of service as compared to uncoated blade that was damaged after 3 months of service.

Uncoated blade at
113 hours (3 months)

Coated blade at
2023 hours (40 months)

Figure 1.2: Coated and uncoated compressor blades after field test in desert conditions.[2]

CrN, $CrAlN$, TiN, and $TiAlN$ coatings are increasingly studied as these coatings present prospects of exceptional erosion, corrosion and oxidation resistance properties even at elevated temperatures [2, 3]. The high hardness values of these coatings made them viable nitride based coatings over the years [4]. This combination of properties makes nitride based coatings especially appealing in applications where parts are routinely exposed to high temperatures and aggressive atmospheres.

1.2 Objectives and Scope

The main objective of this study to characterize and compare indentation creep behavior and erosion resistance of four nitride based nanostructured coatings deposited by cathodic arc : CrN, TiN, $CrAlN$ and $TiAlN$.

Important properties that would be tested include: microhardness, modulus of elasticity, creep parameters, scratch resistance, coefficient of friction and erosion resistance. The coatings were characterized using the following techniques: Micro indentation to determine the hardness and elastich modulus, indentation creep to determine the creep parameters at elevated temperatures, scratch to determine the scratch resistance and the critical load that induced failure of the coatings, X-ray diffraction (XRD) to determine the crystal structure, crystallographic orientation and phases present, Scanning electron microscopy (SEM) to study the morphology and microstructure and Energy dispersive spectroscopy (EDX) to determine the elemental composition of the coatings. Solid particle erosion tests were conducted to determine the erosion resistance of the coatings.

CHAPTER 2

LITERATURE REVIEW

2.1 Cathodic Arc Evaporation

Cathodic arc is a highly versatile PVD technique which is commonly used in a wide variety of applications including decorative, wear and erosion resistant coatings. The vacuum arc deposition dates back to 1877 and the first patent to 1892 [5]. The last century has seen tremendous growth in researches and industrial advancements of arc technologies, especially in the deposition of hard coatings for tribological applications. The prospect of thick, dense and adherent coating properties coupled with the high efficiency of ionizing the target metal are the fundamental tenants that led to much focus on cathodic arc.

Cathodic arc evaporation is a direct current glow discharge involving the explosive emission of plasma from the surface of a conductive electrode. A typical configuration for a cathodic arc deposition process is illustrated in Figure 2.1 [6].

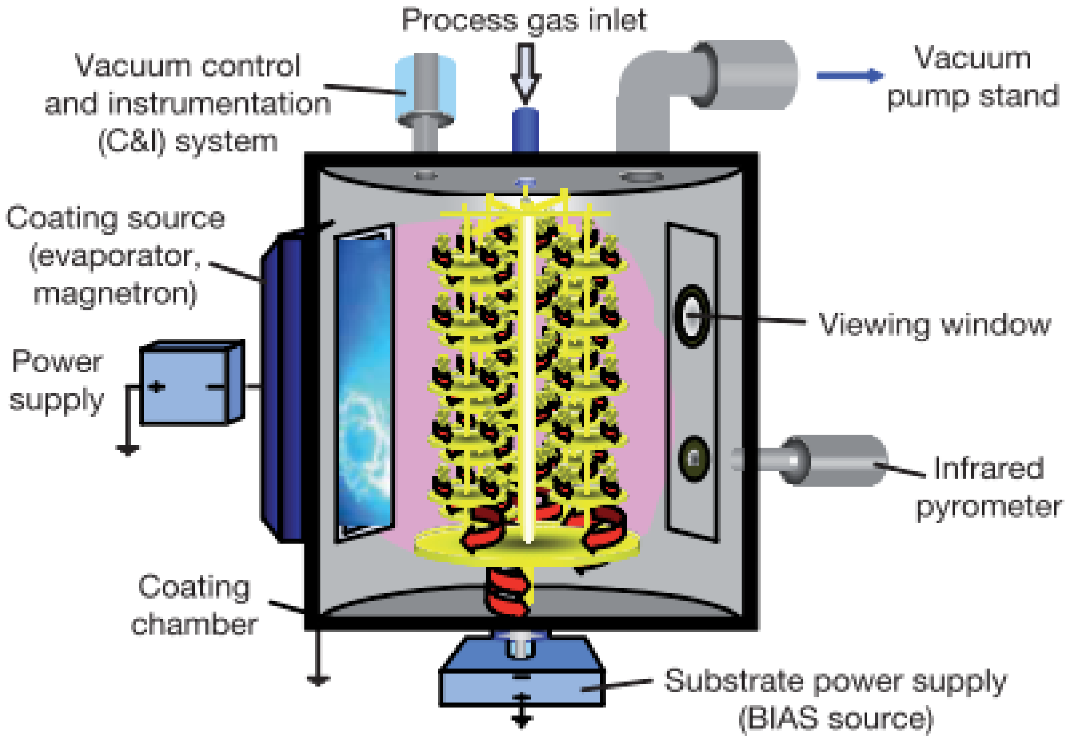

Figure 2.1: Typical cathodic arc system [6]

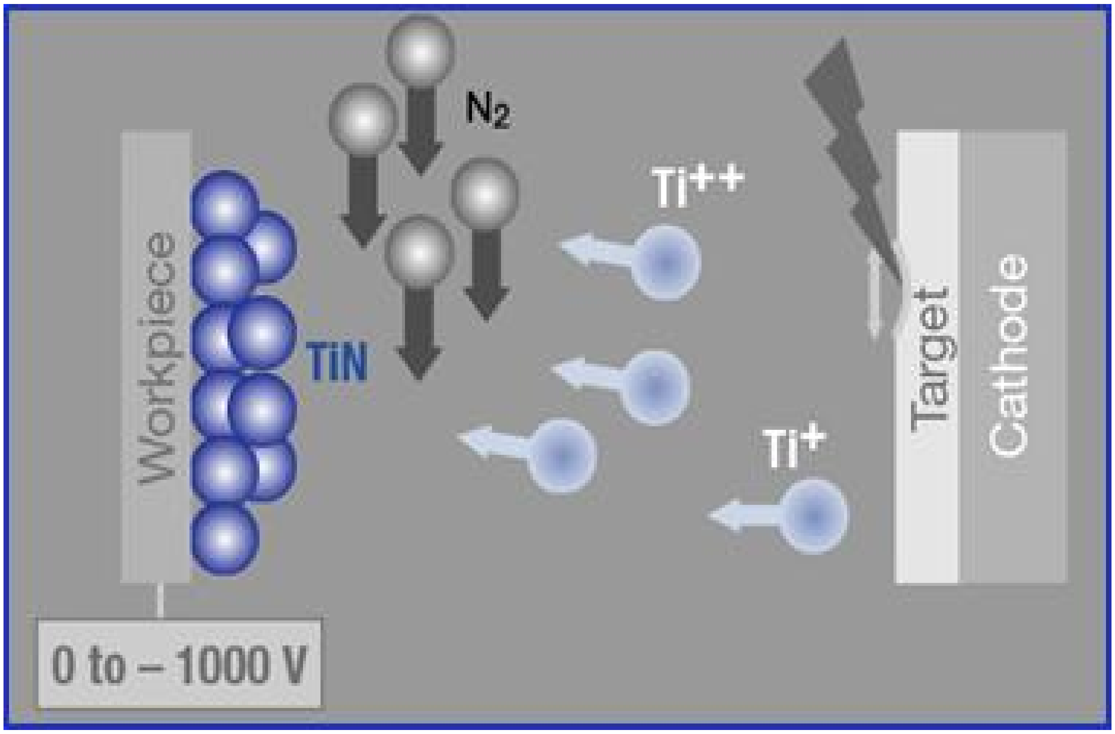

Figure 2.2: Schematic view of the cathodic arc process [6]

During the arc process, high current, low voltage arc is initiated on the surface of the target (cathode) by creating a small amount of plasma to provide current continuity between the electrodes. This can be achieved by a number of different methods. Physical contact with the cathode by a mechanical trigger electrode held at anode potential is a common method. Other methods such as high voltage flash-over from a trigger electrode or laser ablation of the cathode material are also utilized [5, 7].

A stream of electrons of a few 10 to 100 A is generated and flows through the cathode generating small, highly energetic emitting area known as cathode spot. The integral electron flux is composed of fractal individual fluxes, with such an effect that the cathode (target) is melted locally [6]. The localized temperature at the cathode spot is extremely high resulting in the emission of high velocity jet of vaporized cathode material.

The emitted cathode material leaves a crater on the surface of the cathode as shown in Figure 2.2. The cathode spot is usually active for a short duration, then extinguishes and re-ignites in a new area close to the previous crater. This leads to the movement of the cathode spot. The tendency of the arc to conduct current made it possible for the cathode spot to be influenced by applying an electromagnetic field to rapidly move the arc over the entire surface of the cathode in order to achieve uniform depletion with time.

The power density of the arc is extremely high resulting in a high level of ionization, multiple charged ions, atoms and macro particles. The ionized species are accelerated in the electric field towards the negatively biased substrate as shown in Figure 2.2. Ceramic nitride and carbide coatings are produced by running the arc in a reactive gas such as nitrogen or ethylene gas [8].

The ions generated in the process usually possess very high kinetic energies in the range of $20 - 200$ electron volts, leading to enhanced mobility on the surface during deposition. The high energies of the ion are responsible for the different properties of the film obtained in cathodic arc evaporation deposition [5, 7]. High energies during deposition of the target material are essential in the growth of the film to enhance adhesion and stifling columnar structure.

An important trademark of the cathodic arc process is the formation of a considerable amount of ions of the cathode material as compared to other physical vapor deposition techniques such as magnetron sputtering in which the depositing species forming the coating are neutral atoms [9].

A notable disadvantage limiting the use of vacuum arc process for thin film deposition requiring a uniform microstructure such as in magnetic thin films for data storage is the contamination of the plasma by molten droplets of cathode material. These molten droplets are commonly referred to as macroparticles. There are several theories that discuss macroparticle contamination. One theory is that the high ionization at the cathode spot creates enough heat to melt the source material just below the surface [10]. The pressure of the expanding liquid metal then forcibly ejects material from the surface of the source. A second theory of macroparticle creation is that the dense ion current at the cathode arc spots creates localized melt pools. The force of the impacting ions then splatters molten metal out of the melt pool into the plasma. The size of macroparticles may range from $0.1 - 100\mu m$. [7, 10]. Macroparticles may be indulged in ordinary machine tools or metallurgical coatings such as CrN, TiN, $CrAlN$ and $TiAlN$ coatings but usually prevents the use of cathodic arc technique to fields such as optics and electronics [11].

2.2 Creep Mechanism

The mechanical performance of materials at elevated temperature depends greatly on creep behavior since it is activated by thermal processes as a result of high mobility of atoms [12].

In this work the time dependent plastic deformation in which the creep strains are permanent after unloading would be considered. Earlier works on indentation creep were usually performed using hot hardness [13, 14, 15]. Mulhearn and Tabor [16] were credited to have performed the first experiment in indentation creep on lead and indium using spherical indenter at room temperature. They used an approach based on an earlier work in which the indentation strain was compared to uniaxial flow strain by equation 2.1:

$$\epsilon_i = B(\frac{a}{r}) \tag{2.1}$$

Where B is a constant, a is the radius of contact, and r is the spherical tip radius.

A significant milestone was reached in creep research in the early 1990s with the introduction of depth sensing indentation techniques such as micro and nanoindentation [12, 17]. This made it possible to investigate creep in a systematic order by analyzing load-penetration depth curve.

Sharp indentations involves the use of sharp pyramidal indenters (Berkovich or Vickers) in which there is self-similarity in the mean stress and the strain rate and are given as below:

$$\sigma \propto H = \frac{F_{max}}{A_p} \tag{2.2}$$

$$\dot{\varepsilon} = \frac{1}{h}\frac{dh}{dt} \tag{2.3}$$

Here A_p is the projected contact area, F_{max} is the maximum load and h is the penetration depth.

The method discussed above assumed the plastic deformation to occur entirely at steady state thereby following the steady state creep equation:

$$\dot{\varepsilon} = C\sigma^n exp(-\frac{Q}{RT}) \tag{2.4}$$

2.3 Indentation Creep Methods

The four main methods usually utilized in indentation creep experiments are constant displacement, constant loading rate, constant strain rate, and constant load

[17, 12]. These methods would be elaborated briefly as the main focus of this study is constant load method.

2.3.1 Constant Displacement

In constant displacement method, the indenter is held at a predetermined penetration depth, and the subsequent fluctuations in load are recorded with time [18]. This method is not usually used for creep test because it is virtually impossible to keep the penetrated depth constant hence there is continuous variation in both the load and penetration depth leading to error in results analyses.

2.3.2 Constant Loading Rate Method

The constant loading rate method was utilized by Mayo et al [16] in their work on determining the strain rate sensitivity of lead, tin, and lead-tin alloy. This method was based on the premise that, for a specific increase in loading rate, the penetration depth will increase at steady state. Therefore the stress exponent can be obtained by combining the equations for the mean stress and the strain rate (equations 2.2 and 2.3).

2.3.3 Constant Strain rate Method

In this method, the load is increased exponentially with time in each test such that the loading rate increases with the load by a constant ratio thereby maintaining the strain rate constant [17].

2.3.4 Constant load Method

This method is the most widely used due to simplicity in taking measurements and analyzing results. It is the actual focus of this work. Mayo et al. [16, 17] were the first to use this method. A hold period beyond $50s$ was suggested. During this extended hold period, the penetration depth is recorded with time. The value of the stress exponent can be obtained by plotting the change in penetration depth during the hold period with hold time as illustrated in Figure 2.3 [17]. Finally, by plotting a logarithm graph of σ against $\dot{\varepsilon}$, the stress exponent n is obtained.

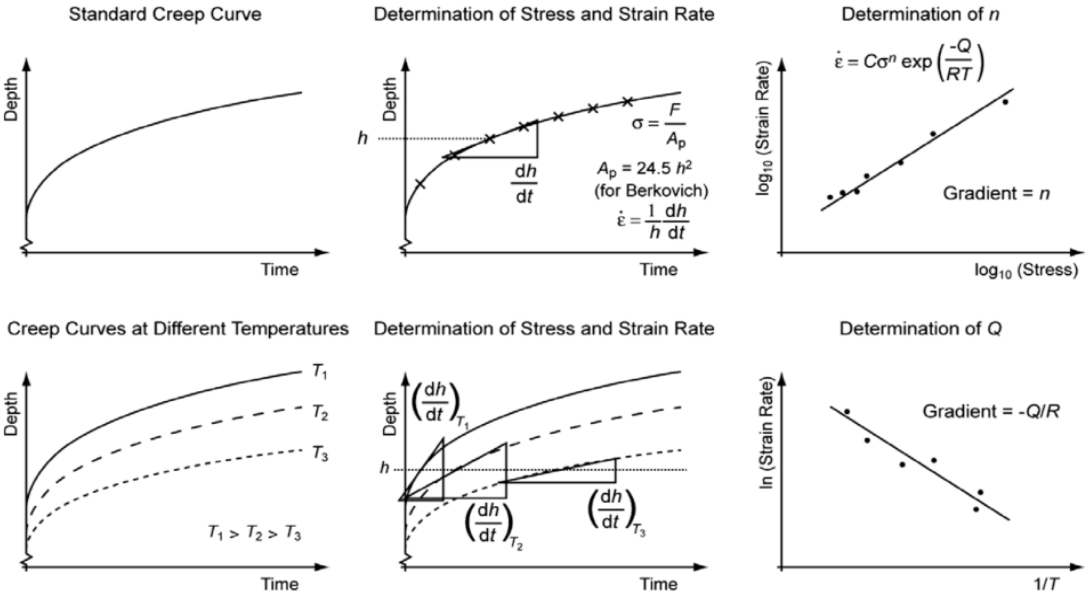

Figure 2.3: Schematics of creep curves obtained under constant load.[17]

2.4 Mechanism of Erosion

Erosion is a complex phenomenon and there has been at least five separate or synergetic mechanisms proposed regarding the removal of material due to hard solid particle impacts and are as follows: (a) Abrasion, (b) Surface fatigue, (c) Brittle fracture, (d) Surface melting, (e) Macroscopic erosion.

Plastic deformation is one of the most widely discussed erosion mechanism that is applicable to ductile materials. Micro-chipping on the other hand is the most discussed erosion mechanism widely associated with brittle materials [19, 20, 21, 22]. Ductile and brittle erosion mechanisms are considered to be the most relevant to the current problems associated with erosion of compressor blades and will be discussed in more detail in Sections 2.4.1 and 2.4.2 respectively.

A low impingement angle favors erosion processes similar to abrasion because the particles tend to track across the worn surface after impact as illustrated in Figure 2.4a. The velocity of the erodent has a significant effect on the erosion. At high angle and low velocity, the stresses at impingement are inadequate for plastic deformation to take place and hence erosion proceeds by surface fatigue as illustrated in Figure 2.4b.

A fourth mechanism discussed in the literature is relevant to multiple phase composite materials that have hard particles embedded in a more ductile matrix. For these materials, it is proposed that porosity around the particle-matrix interface can act as nucleation sites for cracks. Subsequently, crack coalescence occur leading to removal of the hard particles from ductile matrix [23].

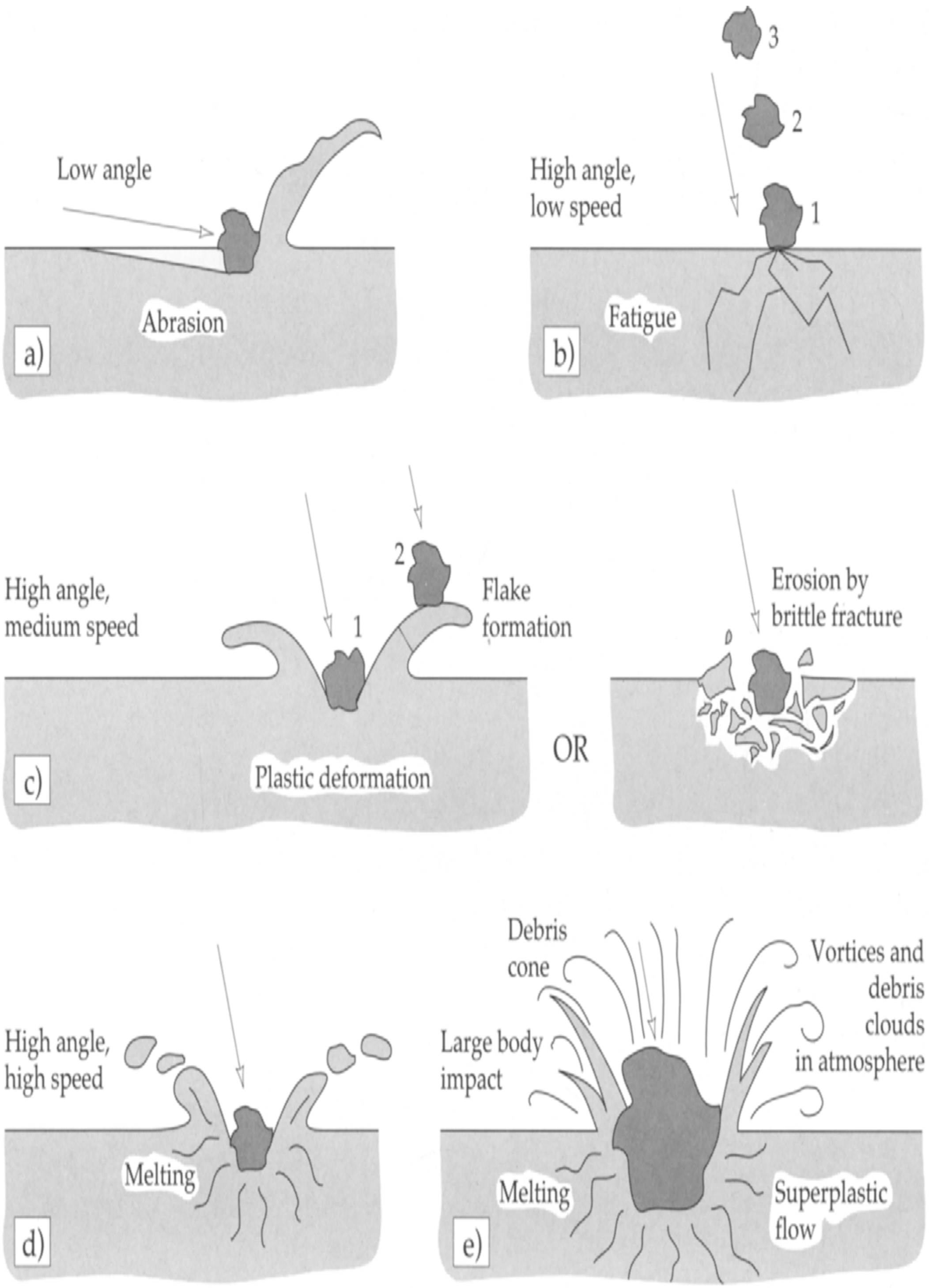

Figure 2.4: Mechanisms of erosion; (a) abrasion, (b) surface fatigue, (c) brittle fracture, (d) surface melting, (e) macroscopic erosion.[22, 24]

2.4.1 Solid Particle Erosion through Plastic Deformation

The predominant theory for the solid particle erosion of ductile materials is that material loss occurs through a plastic deformation process. If the erodent is harder than the surface it is striking, material will be ploughed in the direction of the impinging particle as illustrated in Figure 2.4c showing a hard particle impinging a metallic surface causing plastic deformation. Multiple impacts cause the deformed material to pile up at the edge of the impact craters where subsequent impacts cause the material to break free from the surface resulting in erosion [20, 21]. Erosion rates are usually calculated as the mass loss of the material compared to the total mass of erodent. For ductile metals, such as aluminum alloys, the maximum erosion rate has been found to occur when particles strike the surface at angles between 20^o and 30^o [25].

2.4.2 Solid Particle Erosion of Brittle Materials

In materials with high Youngs modulus values, such as most ceramics, plastic deformation is no longer a valid erosion model. In brittle materials, an impacting particle can cause a very small crater surrounded by a Hertzian strain field. If the force of the impact is large enough, lateral cracking can occur as depicted in Figure 2.4c (brittle fracture). After enough cracks have been formed and with subsequent crack propagation, crack coalescence results in brittle material erosion as material breaks and chips off near the cracks (micro-chipping)[26]. For brittle materials, the primary contributor to erosion rate is related to how much energy is transferred in the particle-surface collision. Maximum energy transfer should occur at 90^o, and correspondingly, experiments from literature confirm that erosion rates are highest at 90^o for brittle materials.[19, 21].

2.5 Effect of Impingement Angle on erosion

Impingement angles can range from $0^o - 90^o$. Figure 2.5 illustrates an impingement angle. At 0^o impingement angle there is negligible wear because the eroding particles do not impact the surface, although even at relatively small impingement angles of about 20^o, severe wear may occur if the particles are hard and the surface is soft. Erosion similar to abrasive wear prevail under these conditions. If the surface is brittle then severe erosion by fragmentation of the surface may occur, reaching its maximum rate at impact angles close to 90^o. The relationship between erosion rate and impingement angle for ductile and brittle materials is illustrated in Figure 2.6. In cases when maximum erosion occurs at low impact angles, the 'ductile mode of erosion' is said to prevail whereas if the maximum erosion occurs at high impact angles the 'brittle mode' is assumed.

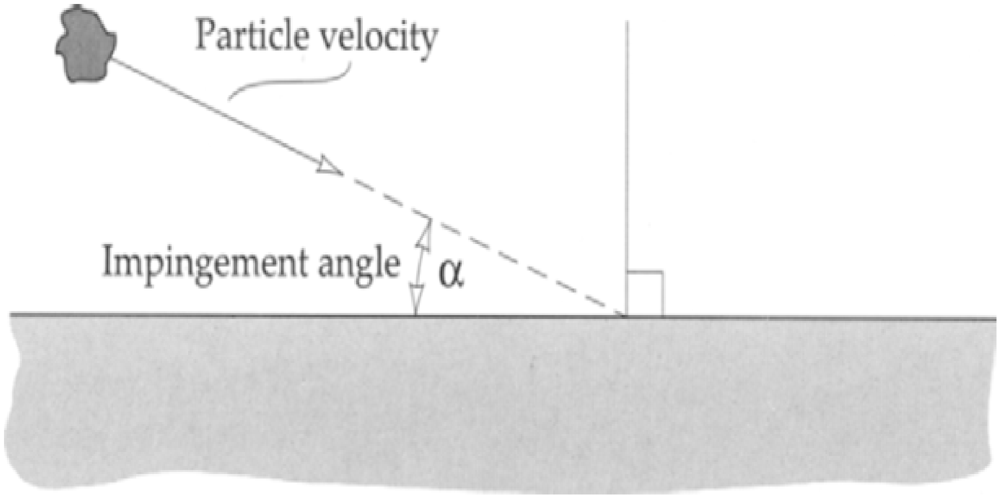

Figure 2.5: Impingement angle of an erodent causing erosion of a surface[22, 24]

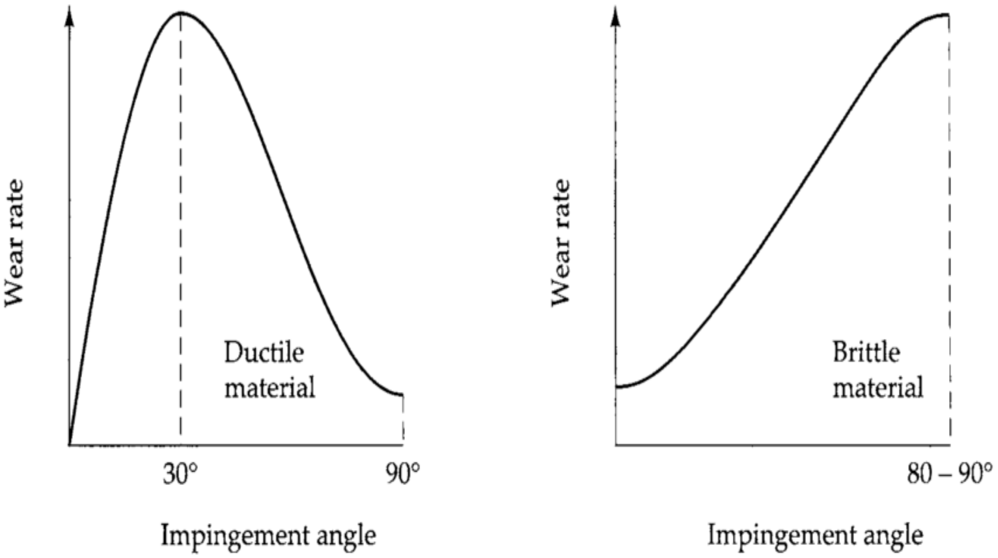

Figure 2.6: Schematic representation of the effect of impingement angle on erosion rates of ductile and brittle materials.[22, 24]

2.6 Erosion Resistant Coatings

The angle of impact for sand particles in aircraft engine may occur over the entire range of $0^o - 90^o$. The wide range of impact angles makes compressor blades particularly vulnerable to erosion since most engineering materials fail with either the previously mentioned micro-chipping mechanism for high angle erosion of brittle materials or the low angle plastic deformation mechanism which is typical of ductile materials.

For metallic compressor blades, the plastic deformation mechanisms leads to significant roughening of the leading and trailing edges of the blades which results in decreased engine performance and efficiency. Leading edge damage of a compressor blade from a General Electric (GE) T-64 series engine is shown in Figure 2.7 [2]. The damage is a result of a combination of erosion (plastic deformation) and large particle impacts which result in the observed deformation of the leading edge.

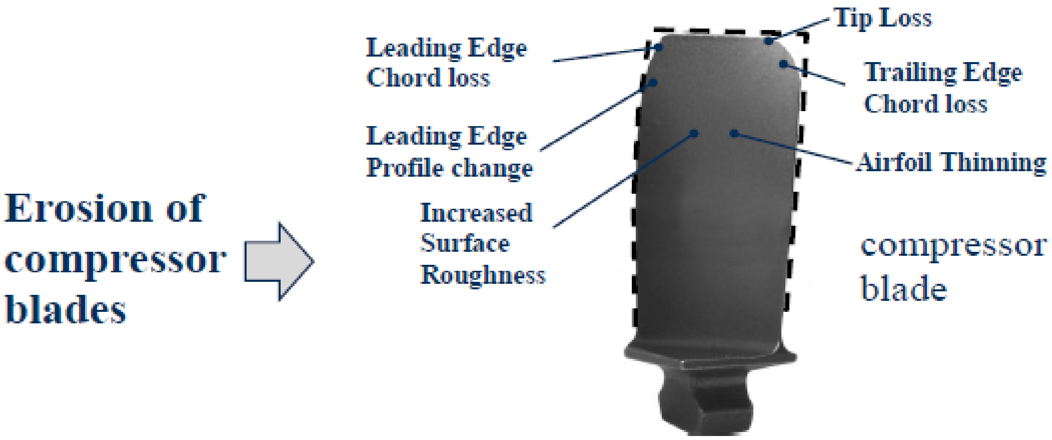

Figure 2.7: Leading edge damage to compressor blade due to solid particle erosion[2]

Since the primary degradation mechanism for the blade is related to plastic deformation, a logical starting point is to design a coating which exhibits high resistance to this type of erosion behavior.

Previous works from literature on nitride and carbide coatings, show that low angle erosion damage can be decreased significantly through the application of ceramic nitride and carbide coatings [4]. However these monolithic ceramic based systems do not provide significant high angle erosion resistance. The protective coating system must also withstand hard particle impacts at a 90^o impingement angle without large scale micro-chipping.

In past studies of hard materials and coatings such as nitrides there has been several microstructural properties identified as important to mitigating hard particle erosion, and includes small grain size, low degree of porosity, absence of cracks [27], high hardness, good toughness[26, 28], and excellent coating adhesion [29]. In addition, the preferred crystallographic orientation of a coating can significantly affect erosion performance [30].

Furthermore, for coating systems, it has been shown that the substrate properties such as composition and toughness can affect the erosion performance since the substrate can affect the stress state, orientation, microstructure and adhesion of the coating [31].

The hardness of a material is a measurement of the resistance to plastic deformation. This relates to the bond strength of the material and also the crystalline structure. The coating hardness and particle impact relationship is related to the plastic deformation that occurs when a single particle impacts the surface. Yang et al showed that for TiAlN coatings, erosion resistance generally increased with increasing hardness[28].

Another important material property for erosion is toughness which is the ability of a coating to resist cracking and crack growth. In terms of erosion, it has been well established that brittle materials fail through micro-chipping and crack coalescence mechanisms.

One way to increase the toughness of hard coatings is to use a multilayer design which has compliant interlayer materials in between the hard ceramic layers. These compliant layers can theoretically act as barriers to crack propagation.

2.7 CrN, TiN, CrAlN, and TiAlN coatings

CrN, TiN, $CrAlN$ and $TiAlN$ coatings were chosen as erosion resistant coatings due to their excellent mechanical and wear properties and their versatile deposition technique using cathodic arc evaporation. The important properties of these coatings are summarized in the Table 2.1. The listed properties in Table 2.1 are characteristic to the deposition technique and process parameters used in their respective studies.

Table 2.1: Summary of typical coating properties of arc evaporated CrN, CrAlN, TiN and TiAlN from the literature.[3, 32, 33, 34, 35]

Coating Property	CrN	TiN	CrAlN	TiAlN
Lattice Parameter(nm)	0.4140	0.4110	0.4242	0.4190
Grain structure	Columnar and equiaxed	Columnar or densely packed	Columnar or densely packed	Columnar or densely packed
Vickers Hardness (HV)	2600 - 3200	2274-3300	2400 - 3700	2783-4200
Modulus of Elasticity (GPa)	318	377	313-394	370 -590
Critical load (N)	31.4,45-55	45.9	20-90,38.1	33.4 -48
Residual Stress (GPa)	Compressive:-2.8 to -9	Compressive:-2 to -6	Compressive: -2 to -9	Compressive: -9.46

2.8 Research Gap

In light of the literature it was observed that, there has been enormous amount of work on the microstructural, mechanical and tribological properties of CrN, TiN, $CrAlN$ and $TiAlN$ arc evaporated coatings. Few researchers did comparative study on the erosion resistance of these coatings. There are limited published studies on comparative characterization of indentation creep and erosion resistance of these coatings.

This work aims to investigate indentation creep and erosion resistance of CrN, TiN, $CrAlN$ and $TiAlN$ arc evaporated coatings for application in the aircraft industry.

CHAPTER 3

EXPERIMENTAL PROCEDURE

The first section of the experimental procedure focuses on the deposition procedures for applying CrN, TiN, $CrAlN$ and $TiAlN$ coatings using cathodic arc evaporation system. The second section discusses the various experimental procedures for coating characterization and analysis.

The primary characterization techniques used for this study includes X-ray diffraction (XRD) for crystallographic structure and preferred crystallographic orientation, microindentation for microhardness, modulus of elasticity and creep behavior, scanning electron microscopy (SEM) for morphology, calotest to determine thickness of the coatings. In addition, coating erosion performance was determined using air jet erosion tester at room temperature.

3.1 Coating Process

3.1.1 Cathodic Arc Deposition Equipment

The various coatings for this study were deposited using a cathodic arc deposition system in the Advanced Coating Laboratory at the Center of Research Excellence in Corrosion, King Fahd University of Petroleum and Minerals, Saudi Arabia. The Domino-mini system was manufactured by Sulzer Metaplas (Germany). Figure 3.1 shows the image of the cathodic arc evaporation equipment used for this work. The functional layout of the PVD coating chamber is illustrated in Figure 3.2.

Figure 3.1: Cathodic arc evaporation equipment

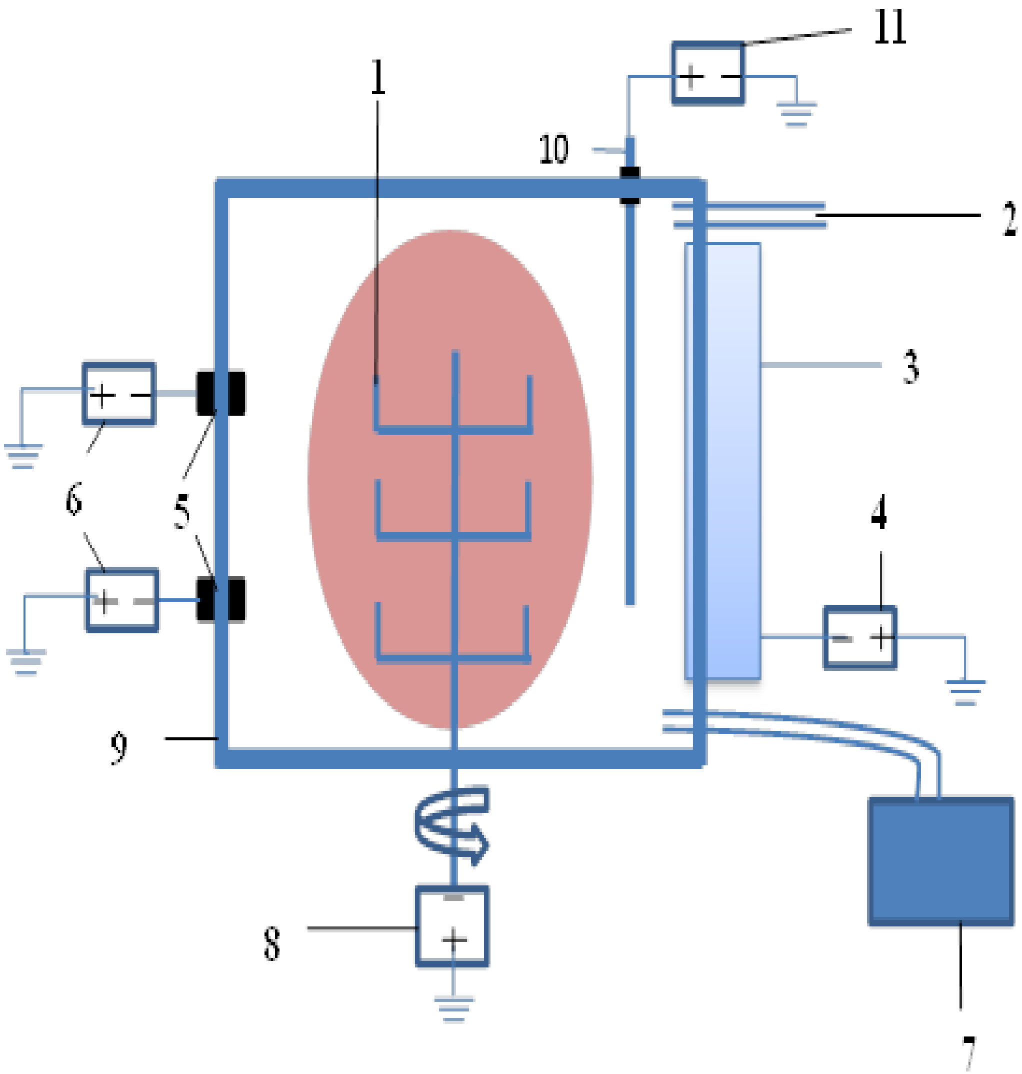

Figure 3.2: Functional layout of the PVD coating chamber (Domino-mini)

1. Work pieces in substrate fixture
2. Gas input (N_2,Ar)
3. Magnetron (option)
4. Power supply (magnetron)

5. Arc evaporators
6. Power supply (arc evaporators)
7. Vacuum pumping station
8. BIAS power supply for substrate
9. Coating chamber
10. Arc Enhanced Glow Discharge (AEGD) anode
11. Power supply for AEGD anode

3.1.2 Substrate Preparation

The substrate material investigated during this project is AISI 304 stainless steel. AISI 304 stainless steel is a commonly used material for various components hence was selected for this work. In particular, AISI 304 stainless steel sheet stock with a $3mm$ thickness was cut into $25 \times 25mm$ coupons. The coupon surfaces were then ground with silicon carbide paper of grit sizes of $180, 240, 320, 400, 600$ and 800 respectively. The ground coupons were then polished on emery cloth with $0.03\mu m$ alumina paste which produced surface finish of approximately 0.06 ± 0.001 Ra. After surface preparation, the coupons were cleaned in ethanol and dried with N_2 after which the coupons were ultrasonically cleaned in acetone for 20 minutes. After the ultrasonic cleaning the samples were once again rinsed with ethanol and dried with N_2. All substrates were then loaded the same day into the cathodic arc chamber. Figure 3.3 shows the loaded substrates on the planetary.

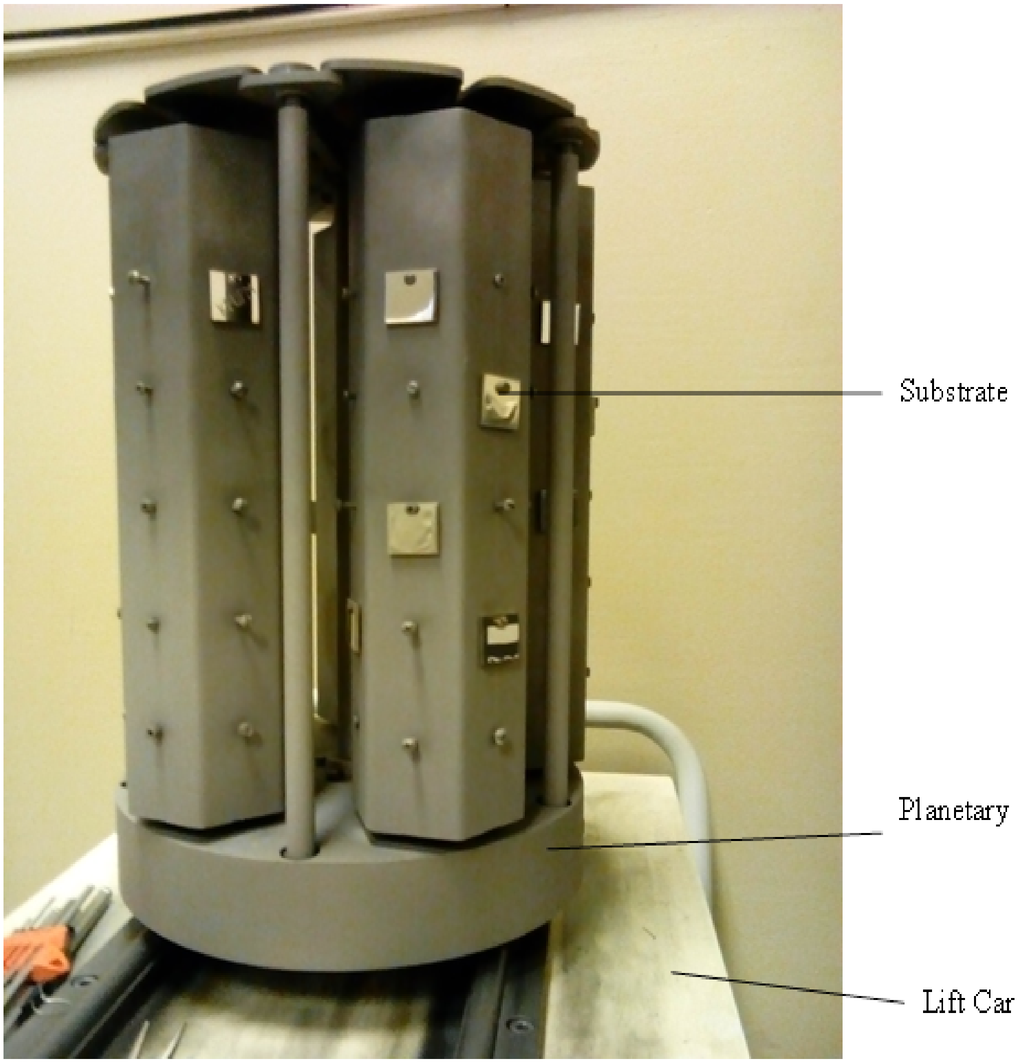

Figure 3.3: Work pieces in substrate fixture ready to be loaded in to the chamber

3.1.3 Cathodic Arc Deposition Procedure

The solvent cleaned samples are loaded onto the planetary, that is then loaded in to the deposition chamber using the planetary lift car as illustrated in Figure 3.3. After the planetary is loaded in to the chamber, the chamber is evacuated to a pressure of $4 \times 10^{-5} mbar$. The vacuum pumping system is illustrated in Figure 3.4. Once the desired base pressure was achieved, a rate-of-rise test was conducted in which the system seals were evaluated by closing the system gate valves and measuring the rise in chamber pressure over a two minute period. A pressure rise of less than an order of magnitude was necessary in order to proceed to the next step in the deposition procedure which was the arc enhance glow discharge etching process (AEGD). The progress of the process is monitored on the process screen. The process screen is illustrated in Figure 3.5.

Prior to initiating the AEGD etching process the IR heater was set to 500^oC and the substrate rotation was started. For this study the planetary rotation was clockwise at $2rpm$. The loaded work piece is heated for one hour.

Pretreatment of the substrates is done using Arc Enhanced Glow discharge (AEGD) process in which Ti ions are extracted from a special cathode called AEGD cathode made from pure Ti grade 2. Figure 3.6 shows AEGD cathode made from pure Ti.

A metal plate in front of the evaporator absorbs the positively charged Ti ions resulting in a surplus electrons generated in the chamber. Argon gas is introduced in to the chamber. Due to the high velocity of the argon gas admitted to the chamber, they are ionized by electrons. The positively charged argon ions are accelerated by the bias voltage in direction of the negative substrate. By hitting the substrate surface with high impact energies, the surfaces are cleaned from residual dust, native oxide layers and other remaining impurities which could affect coating adhesion. The electrons are accelerated and attracted by the AEGD anode. The AEGD process removes surface layer to about $200 - 400nm$.

Following the AEGD etching, the next step was coating deposition starting with the bond layer. The bond layer is a thin metallic layer deposited on the substrate in a limited nitrogen pressure to enhance adhesion of the coating to the substrate. During the bond layer deposition, the charge on evaporator was set to a value of 20 ampere hours (Ah) and nitrogen pressure of $8.5 \times 10^{-2} mbar$. The two evaporators, A and B as illustrated in Figure 3.7 were then supplied with a current of 130A.

Deposition of the nitride based coatings immediately followed the bond layer deposition. The evaporator charge (ampere hours) was increased to $150Ah$ at a nitrogen pressure of $7.5 \times 10^{-2} mbar$. The charge was further increased to $200Ah$ and the pressure to $6.5 \times 10^{-2} mbar$ in order to achieve a coating thickness of approximately $1.8 \mu m$. The complete deposition parameters are shown in Table 3.1. The process parameters were optimized in order to obtain a coating with an approximate thickness of $1.8 \mu m$.

For CrN evaporator A and B was fitted with 99.99% Cr cathodes, for TiN, evaporator A and B was fitted with 99.99% Ti cathode. $Cr - Al$ alloy of $30Cr - 70Al$ at% compositions was used for $CrAlN$ and $Ti - Al$ alloy of $45Ti - 55Al$ t% composition was used for $TiAlN$.

Cooling down of the substrate and the chamber takes place for one hour and the substrates are finally unloaded.

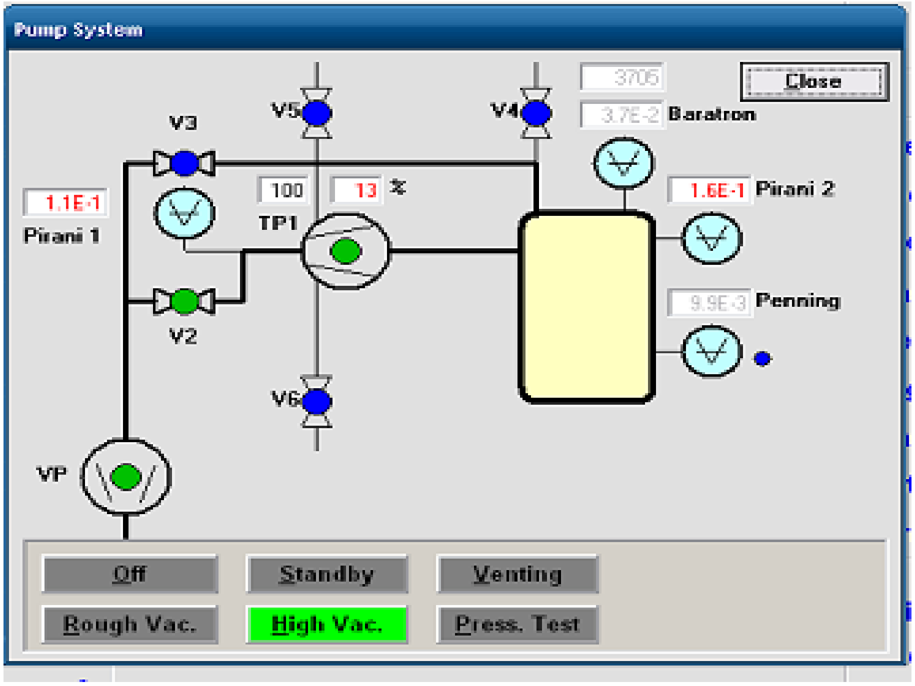

Figure 3.4: The pump system indicating the level of evacuation

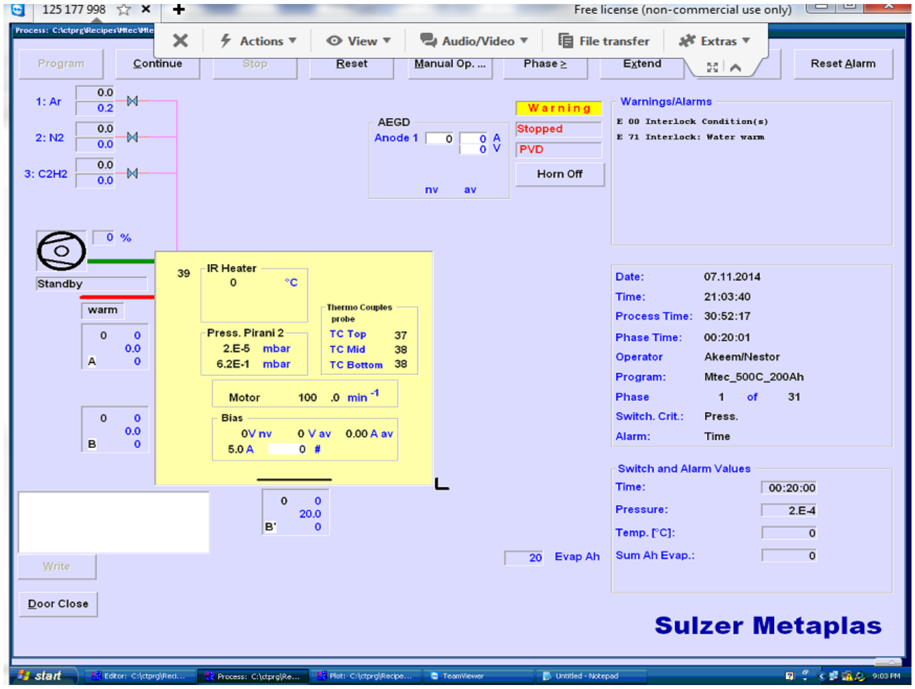

Warnings/Alarms

```
E 00 Interlock Condition(s)
E 71 Interlock: Water warm
```

Press. Pirani 2: 2.E-5 mbar, 6.2E-1 mbar

TC Top 37
TC Mid 38
TC Bottom 38

Motor 100 .0 min $^{-1}$

Bias: 0V nv, 0 V av, 0.00 A av, 5.0 A, 0 #

Date: 07.11.2014
Time: 21:03:40
Process Time: 30:52:17
Phase Time: 00:20:01
Operator Akeem/Nestor
Program: Mtec_500C_200Ah
Phase 1 of 31
Switch. Crit.: Press.
Alarm: Time

Switch and Alarm Values
Time: 00:20:00
Pressure: 2.E-4
Temp. [°C]: 0
Sum Ah Evap.: 0

Figure 3.5: Process screen for monitoring and control of the deposition process

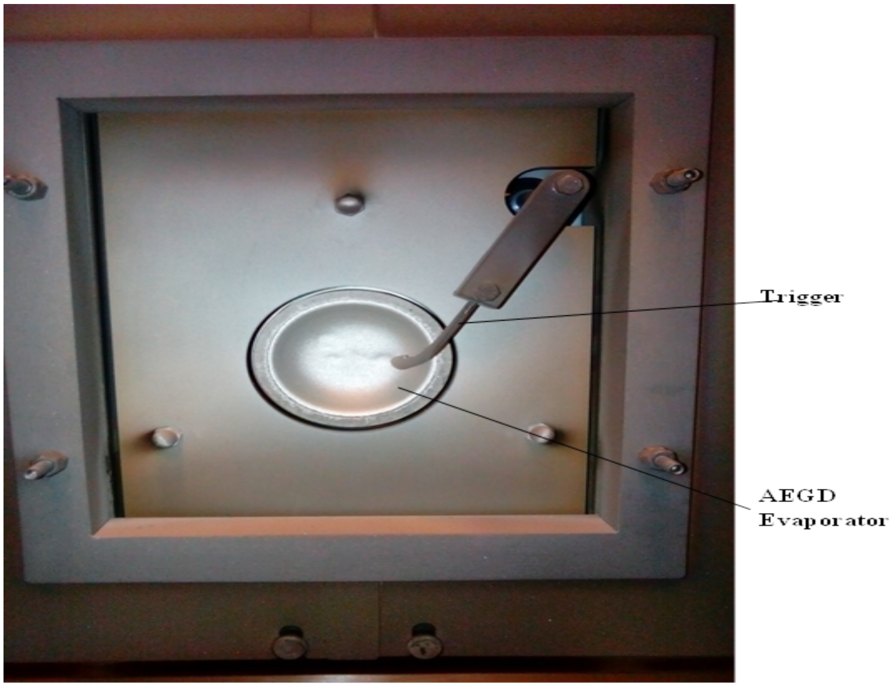

Figure 3.6: Arc Enhanced Glow Discharge cathode (pure Ti grade 2)

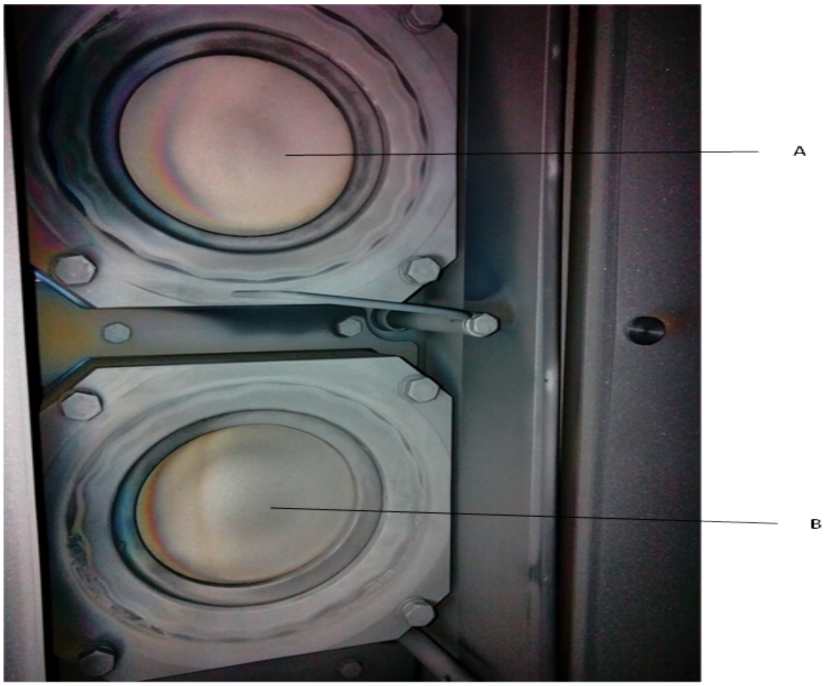

Figure 3.7: Evaporator A and B

Table 3.1: Deposition parameters for the four nitride coatings

Program Name		CrN	TiN	CrAlN	TiAlN
Substrate		AISI 304 SS	AISI 304 SS	AISI 304 SS	AISI 304 SS
AEGD etching process	IR Heater (^oC)	500	500	500	500
	Evaporator (AEGD)	Ti(99.99%)	Ti(99.99%)	Ti(99.99%)	Ti(99.99%)
	Evaporator Current (A)	85	85	85	85
	Substrate bias (V)	-250	-250	-250	-250
	Duration (min)	40	40	40	40
	Argon Pressure $mbar$	1×10^{-2}	1×10^{-2}	1×10^{-2}	1×10^{-2}
Parameters	IR Heater (^oC)	500	500	500	500
	Evaporator	Cr(99.99%)	Ti(99.99%)	$70Al - 30Cr\ at\%$	$55Al - 45Ti\ at\%$
	Evaporator Current (A)	130	130	150	150
	Substrate bias (V)	-100	-100	-80	-80
	Duration (min)	60	60	60	60
	Nitrogen Flow-bond coat(sccm)	50	50	50	50
	Nitrogen Flow-Coating(sccm)	215	215	215	215

3.2 Coating Characterization and Evaluation

In this section various characterization techniques were employed to evaluate the quality and the performance of the coatings.

3.2.1 X- ray diffraction (XRD)

Bruker D8 advance X-ray diffractometer was used for phase analysis of all the coated samples. X-ray diffraction patterns were obtained by irradiation of the coatings using a copper anode incident through a cross-slit collimator ($1.2mm \times 1.0mm$) at an angle of theta parallel to the substrate surface. At specific incident angles, the periodicity of the samples crystallographic structure results in X-rays scattering coherently and the constructive interference is referred to as diffraction. The diffraction of the X-rays can be predicted according to Braggs law:

$$n\lambda = 2d_{hkl}\sin\theta \tag{3.1}$$

Where λ is wavelength of the incident X-ray, d_{hkl} is the interatomic spacing between the planes defined by hkl, θ is the angle of diffraction, and n is the order of the reflection.

By scanning the sample over a wide range of diffraction angles (θ), the crystallographic structure of the coating can be determined by measuring the angles where diffraction occurs and comparing these values to the standards published by the International Center for Diffraction Data (ICDD).

All the coated samples in this study were subjected to a $\theta/2\theta$ scan in which the incident beam is held at a fixed angle and the sample and the detector are continuously rotated θ and 2θ, respectively. The copper $K\alpha$ radiation of wavelength $\lambda = 0.154186nm$ was used and $\theta/2\theta$ values in the range of $10 - 100^o$.

3.2.2 Scanning electron microscopy (SEM)

JEOL scanning electron microscope (JSM 6460LV) was used to examine both the top surface and cross sections of the coatings. An electron microscope bombards the sample surface with a focused beam of electrons which interact with the sample structure, topography, and elementary composition to produce secondary electrons (SE).

The incident electrons can also be scattered away from the sample surface and these electrons are referred to as back scattered electrons (BS).

In addition to SE and BS electrons, the incident electron beam can produce X-ray emissions which have characteristic wavelengths dependent on the elemental composition of the coated sample. These characteristic X-ray emission lines were used in energy dispersive spectroscopy (EDS) to quantify the coating elemental composition.

3.2.3 Coating Thickness

During the calotest measurement a rotating sphere, with a $20mm$ diameter was pressed on the coating surface with a predetermined load. Both the position of the sphere relative to the sample and the contact load were kept constant. Upon adding $0.3\mu m$ diamond paste to the contact zone, a depression with the shape of a spherical cap was abraded into both the coating and the substrate as illustrated in Figure 3.8.

Optical inspection of the depression reveals the projected surfaces of the abraded coating and substrate sections. By measuring the parameters X and Y, the thickness of the coating can be evaluated by the geometrical equation 3.2 below.

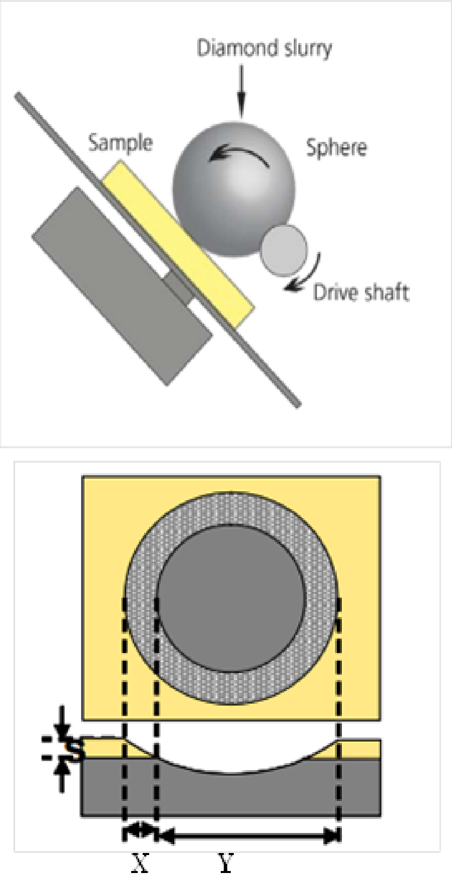

Figure 3.8: Schematic representation of calotest measurement

$$Thickness, S = \frac{X \times Y}{ball - diameter} \tag{3.2}$$

3.2.4 Microindentation Test

Microindentation tests were performed using CSM micro combi tester, fitted with Vickers indenter VH 85. The Vickers indenter uses a four sided square based diamond pyramid tip with 136^o between faces and an applied load to plastically deform the sample. The modulus of elasticity and the microhardness (Vickers) are determined from the loading and unloading curve using the Oliver & Pharr ($O\&P$) [36, 37] method of analysis.

The indenter-sample contact is analyzed as illustrated in Figure 3.9 below. Vickers hardness (HV) is calculated from equation 3.4 below and is directly related to the material resistance to plastic deformation:

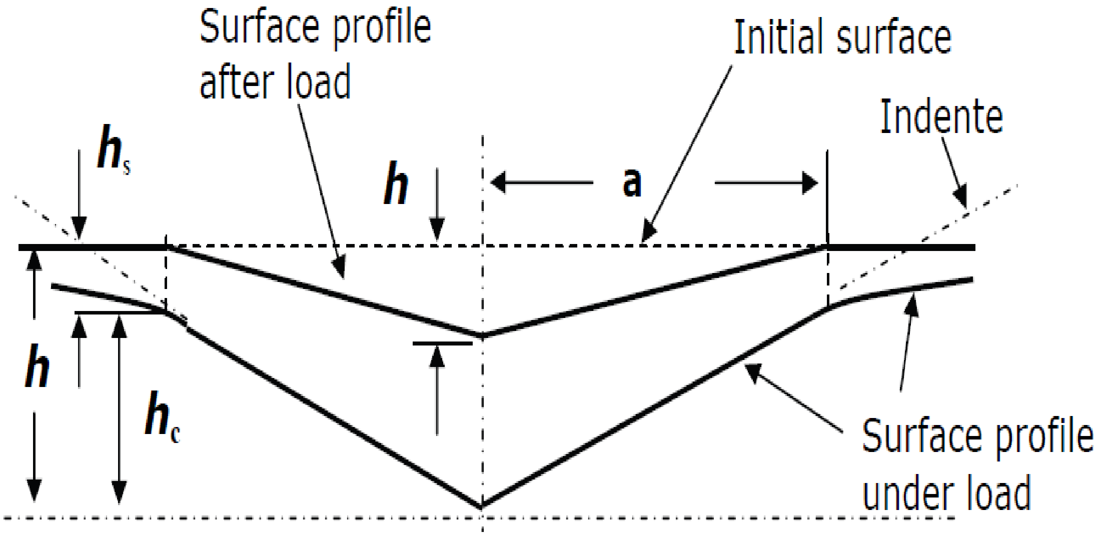

Figure 3.9: Schematic representation of indenter - sample contact [37]

$$A_p = C_o h_c^2 + C_1 h_1^{\frac{1}{2}} + \ldots \cdots + C_8 h_8^{\frac{1}{128}} \tag{3.3}$$

$$HV = \frac{F_{max}}{A_p} \tag{3.4}$$

Where h_c is the contact depth of the indenter with sample at maximum force, A_p is the projected contact area, F_{max} is the maximum test force, $C_o \ldots\ldots C_8$ are constants depending on indenter geometry.

The load used for the HV measurements was $20mN$. This load was selected in order to get a penetration depth less than 10% of the coating thickness thereby reducing the effect of the substrate on the hardness readings. The modulus of elasticity was evaluated from the slope of the initial portion of the unloading curve. The slope at this point termed the stiffness is then substituted into equations 3.5, 3.6, 3.7 below to arrive at the indentation modulus of the coatings.

$$E_r = \frac{\sqrt{\pi S}}{2\beta\sqrt{A_p}} \tag{3.5}$$

$$E_r = \frac{1}{\frac{1}{E_r} - \frac{1-v_i^2}{E_i}} \tag{3.6}$$

$$E_{IT} = E^* \times (1 - v_s^2) \tag{3.7}$$

Where E_r is the reduced modulus, S is the stiffness from the loading and unloading curve, β is indenter geometry constant,A_p is the projected contact area, E^* is the plain strain modulus, V_i is Poisson ratio of the indenter (0.07), E_i is the elastic modulus of the indenter (diamond, $1141GPa$), V_s is the Poisson ratio of the specimen and E_{IT} is the modulus of elasticity of the specimen.

3.2.5 Scratch Test

Scratch resistance measurements were made using CSM micro combi tester fitted with a diamond tipped stylus (Rockwell $I-176$ indenter) to scratch the coatings with linear increasing load as the stylus tip traversed along the coating surface.

The load is linearly progressive until the coating fails and/or delaminates in the scratch track. The load required to cause crack or delamination from the substrate is referred to as the critical load, L_c. The coating failure under constant loading conditions is often determined by an acoustic emission signals (caused by the high frequency associated with crack or detachment).

3.2.6 Creep Test

The creep parameters of the coatings were determined from indentation creep test. The constant load method was used whereby the load applied was held at maximum value for $60s$. CSM micro-combi tester coupled with Linksys 32 heating stage (Linkam Scientific Instruments) were used. The tests were performed at temperatures of $50^oC, 75^oC$ and 100^oC.

The creep parameters were evaluated using equations 2.2, 2.3 and 2.4 in section 2.2 for mean stress, strain rate and activation energy, respectively. The stress exponent, n, was determined from the slope of a logarithm plot of strain rate with the mean stress using equation 2.2.

The activation energy for creep was estimated from the plot of natural log of the strain rate with the inverse of temperature. The gradient from which the activation energy was evaluated.

3.2.7 Erosion Test

Room temperature solid particle erosion testing was performed on the coatings using room temperature air jet erosion test rig manufactured by KOEHLER Instruments Inc. The nozzle diameter, length and other specifications of the equipment conform to ASTM G76-95 [38]. The specifications are shown in Table 3.2. Particle flow rate was accurately controlled by the rotation frequency of the discharge wheel located at the outlet of the erodent hopper. The mass of erodent flowing through the nozzle for 10 minutes at a $7.5Hz$ wheel frequency was collected from which the particle flow rate was calculated.

Angular alumina with average particle size of $50\mu m$ was used as an erodent. Alumina is hygroscopic; hence care was taken to ensure moisture free erodent by baking in an oven at 110^oC for 24 hours, while stirring at regular intervals. Compressed air stream used to accelerate alumina particles was first passed through moisture trap and then through air filter to ensure clean and dry air.

Particle velocity was measured using double disk rotation method [39]. It consists of two metal disks (A and B) mounted on a common shaft and caused to rotate in front of the particle jet. A single radial slit in disk B permits particles to pass through and eventually erode a mark on disk A.

The measurement process begins by mounting the motor to which the double disk assembly has been attached in a rigid position with respect to the nozzle of the erosion test apparatus. The slit in disk B is positioned opposite the jet and exposure is made with the motor operating at a constant speed for 10 minutes. The exposure time is a function of the width of the slit in B. The diameter of the scar mark on disk A is measured. The speed of the disk, the time of exposure, the diameter of the erosion scar on disk A and the angular displacement of the erosion scar are substituted in equation 3.7 below to determine the particle velocity.

$$v = 2\pi r V \frac{L}{S} \tag{3.8}$$

Where v is the particle velocity, r is the radius of the erosion scar, V is the angular velocity of the disks, L is the distance of separation between the two disks and S is the angular displacement.

The velocity was measured with an accuracy of $\pm 2m/s$ and was correlated with air pressure. The particle flow rate and velocity calibrations were checked after every 00 experiments.

Four different impingement angles were used: $30^o, 45^o, 60^o$ and 90^o. The dimensionless steady state erosion rates were calculated from the slope of the average mass loss versus erodent mass. By choosing these impact angles, the coatings would be evaluated at both low and high incident angles.

The erosion performances of the coatings were studied at 150 seconds and 600 seconds. This was done in order to assess the initial stages and intermediate stage of erosion. For the initial assessment of the coatings at 150 seconds, the coatings were weighed every 30 seconds whereas for the intermediate performance, the coatings were weighed every 120 seconds to determine the mass losses respectively. The incremental erosion rate method was utilized.

Tests were carried out at 60m/s velocity corresponding to a pressure of 0.9 bar. Particle flow rate of 2g/min and 2.5g/min (corresponding to 5.5 and 7.5Hz wheel frequency) was kept constant for the initial and long term assessments respectively. The erosion rig is shown in Figure 3.10.

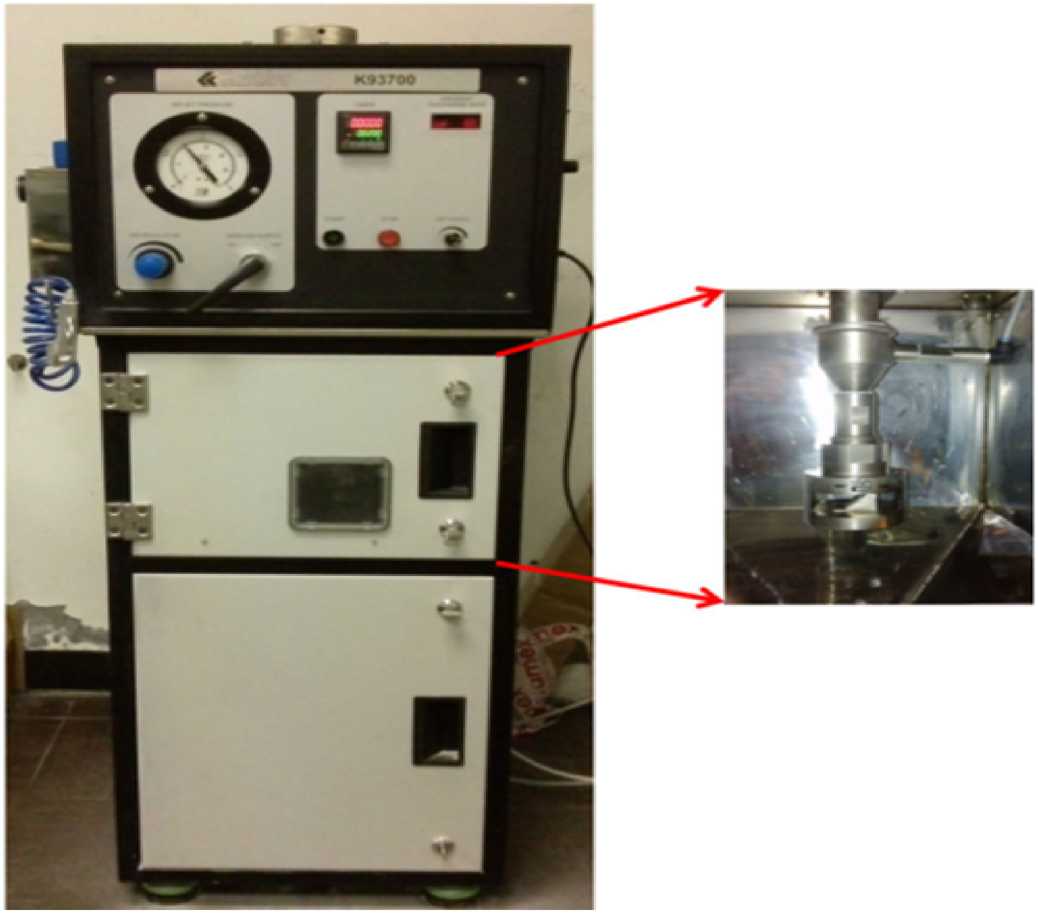

Figure 3.10: Room temperature air jet erosion tester

The samples were cleaned and then weighed using a four significant digit scale (0.0001g). A minimum of two measurements were taken, and the standard deviation for the values were typically less than 0.0005g. The parameters used are illustrated in Table 3.2.

Table 3.2: Deposition parameters for the four nitride coatings

Test Parameter		Detail
Air	Temperature	Ambient
	Pressure	0.9 bar
	Velocity	$60m/s$
Specimen	Size	$25 \times 25 \times 3mm^3$
	Material	CrN, TiN, CrAlN & TiAlN
	Temperature	Ambient
	Angle of Impingement	$30^o, 45^o, 60^o \& 90^o$
Erodent	Material	Alumina (angular)
	Size	$50\mu m$
	Discharge Rate	2g/m & 2.5 g/m
Nozzle	size	Inner diameter = 1.5 mm, outer diameter = 12 mm × 50 mm long

3.2.8 Residual Stresses

The coatings were annealed at 800^oC for two hours in order to relief residual stresses present after deposition. XRD analysis was performed on the annealed coatings from which the average crystallite size and residual stresses were evaluated. Microhardness and scratch resistance of the coatings were evaluated after annealing. Microhardness was evaluated at $20mN$ load. Scratch was performed with a linearly progressive load of $0.03 - 30$N over $15mm$ distance across the surface. The influence of residual stress on the mechanical properties were investigated.

CHAPTER 4

RESULTS

4.1 Microstructural Characterization

This section presents the results of the compositional and microstructural characteristics of the various coatings deposited by cathodic arc evaporation using XRD and SEM.

4.1.1 Morphology

SEM analysis provide qualitative information on the morphologies of the coatings. The characteristic X-ray emission lines were used in Energy Dispersive Spectroscopy (EDS) to quantify the coating elemental composition. The morphologies of the coatings are illustrated in Figure 4.1.

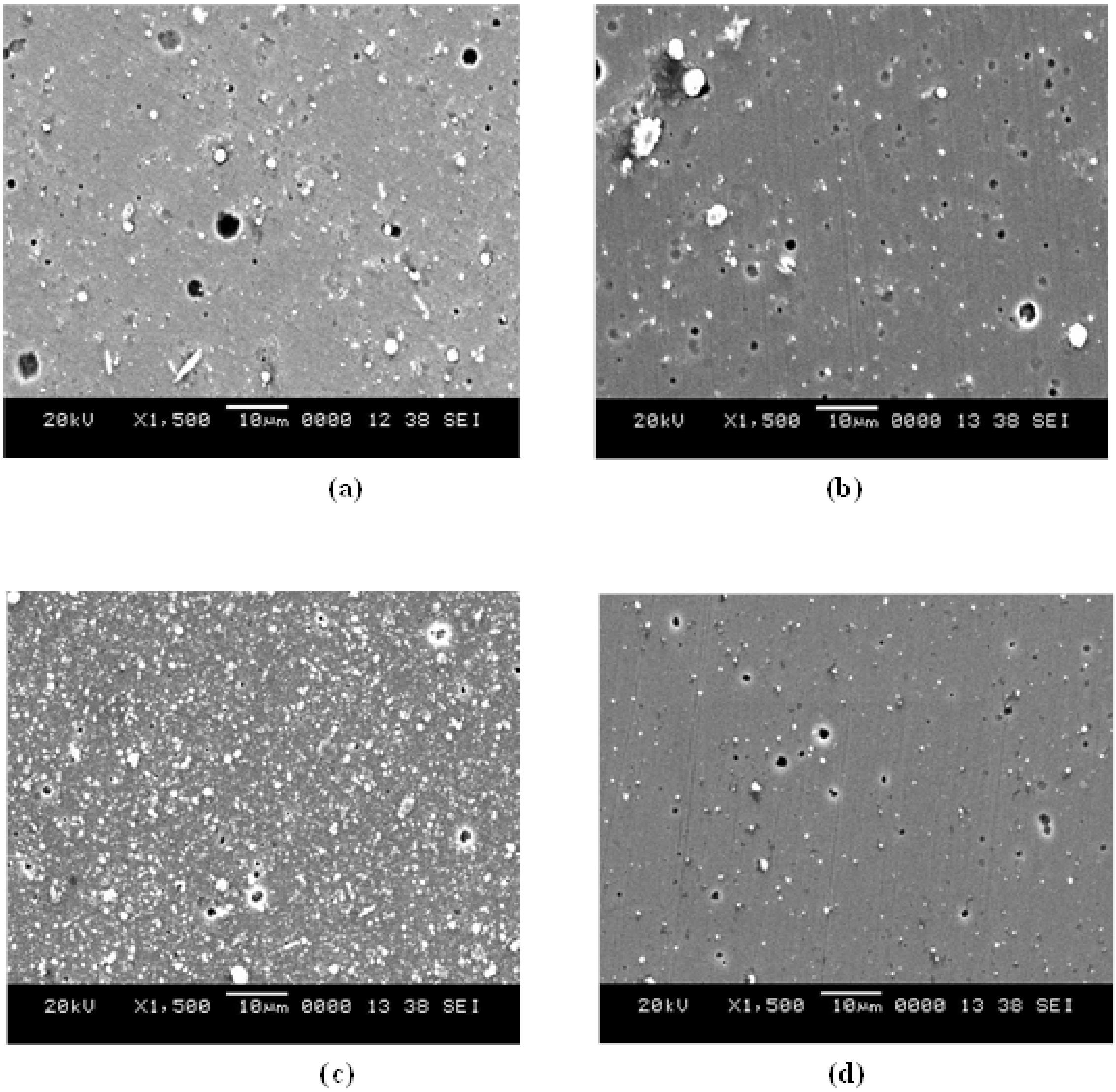

Figure 4.1: SEM micrographs showing the morphologies of : (a) CrN (b) TiN (c) CrAlN and (d) TiAlN coatings.

4.1.2 Composition

Energy dispersive spectroscopy was used to investigate the elemental composition of the coatings. The elemental compositions of the four nitride coatings are shown in Table 4.1.

Table 4.1: EDX showing elemental composition of the four nitride coatings

	CrN	TiN	CrAlN	TiAlN
Element	*Atomic%*	*Atomic%*	*Atomic%*	*Atomic%*
N	47.4	48.6	49.2	47.8
Al	-	-	33.3	26.1
Ti	-	51.4	-	26.1
Cr	52.6	-	17.5	-

4.1.3 Crystallographic Structure

In order to determine the crystallographic structure of the coatings $\theta/2\theta$ XRD scans were performed as described in section 3.4.1, and compared to the Powder Diffraction Files published by the International Centre for Diffraction Data (ICDD). Additionally, an XRD pattern of a non-coated AISI 304 stainless steel substrate was obtained in order to distinguish diffraction peaks originating from the substrate. The $\theta/2\theta$ diffraction pattern for the CrN, TiN, $CrAlN$, $TiAlN$ coatings and the AISI 304 stainless steel substrate are shown in Figure 4.2. The XRD pattern of CrN reveals similar texture of $\{111\}$, $\{200\}$ and $\{311\}$ reflections while the {220} reflection is diminished. TiN shows strong reflection of {111}. Both ternary nitrides show strong reflection of {200}.

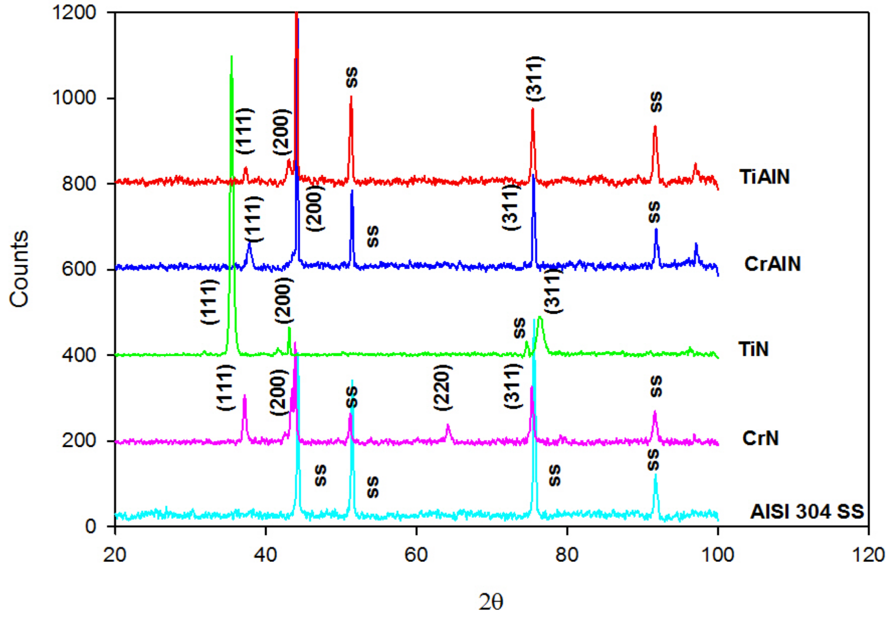

Figure 4.2: XRD pattern of CrN, TiN, CrAlN and TiAlN on AISI 304 Stainless steel.

4.1.4 Coating Thickness

The optical micrographs of the coatings during the ball crater operation to estimate the thickness are presented in Figures 4.3 and 4.4 for CrN, TiN, $CrAlN$ and $TiAlN$, respectively. The coating thicknesses are presented in Table 4.2.

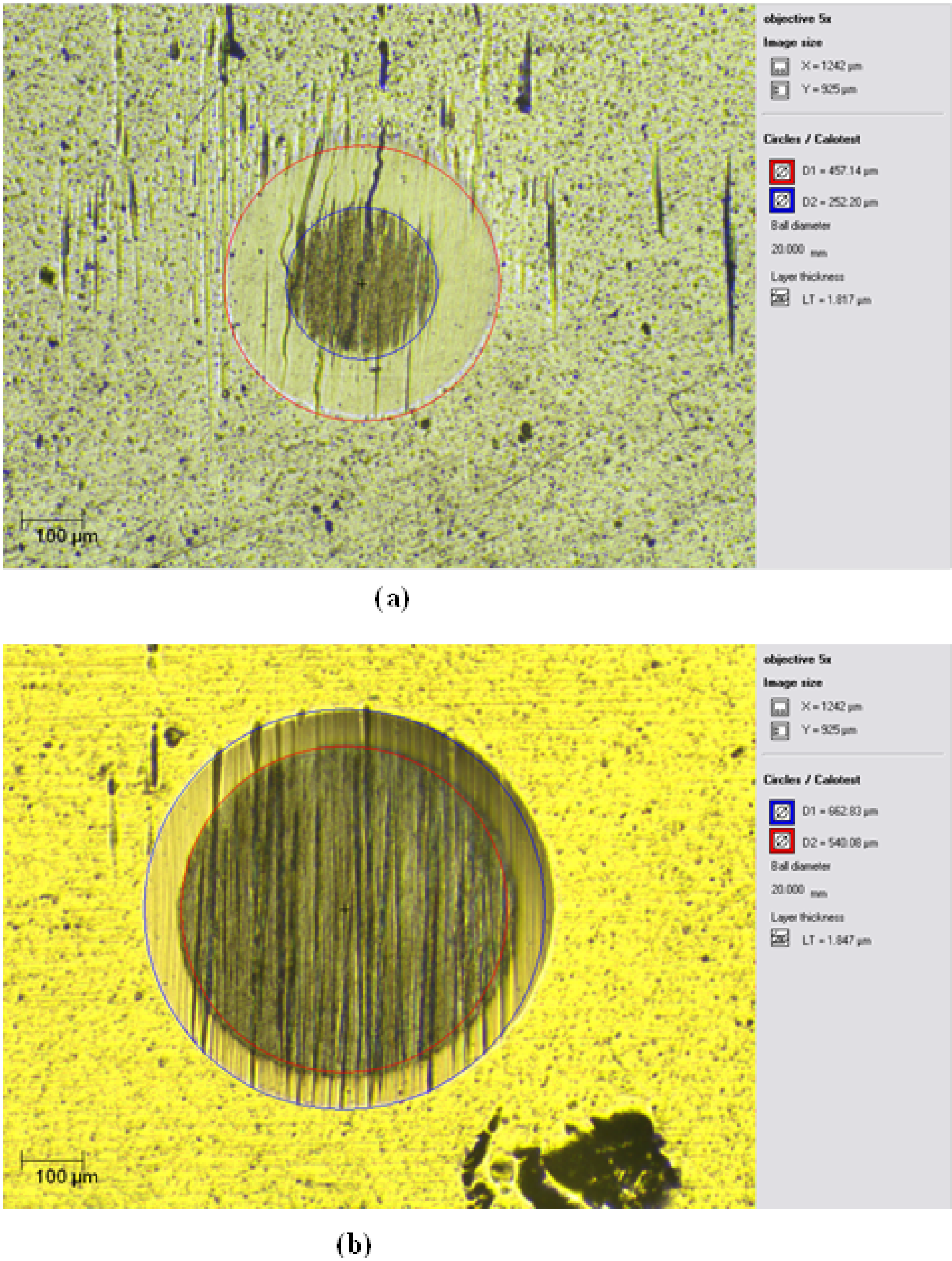

Figure 4.3: Optical micrograph illustrating calotest impression (a) CrN and (b) TiN

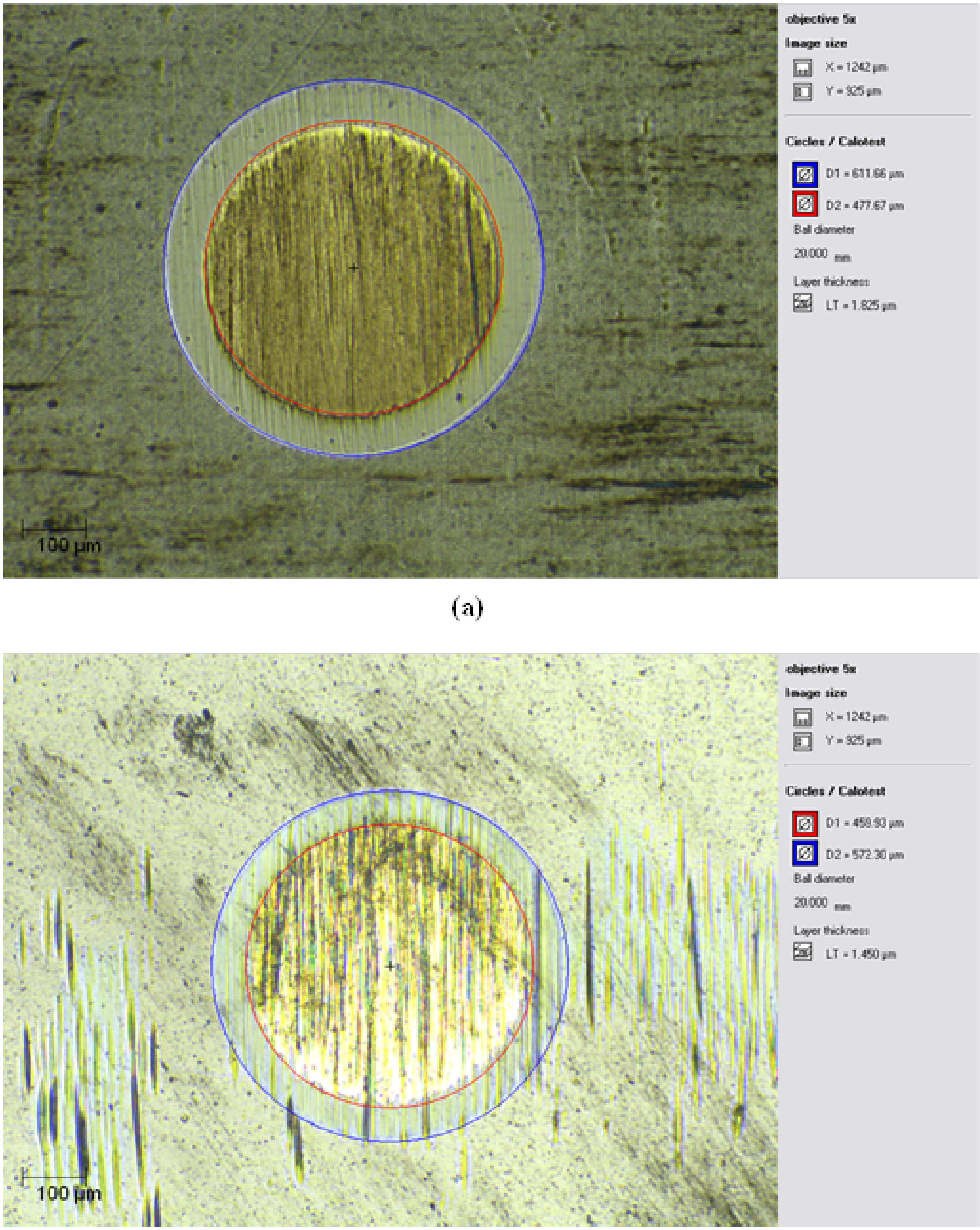

objective 5x
Image size
X = 1242 µm
Y = 925 µm
Circles / Calotest
D1 = 611.66 µm
D2 = 477.67 µm
Ball diameter
20.000 mm
Layer thickness
LT = 1.825 µm

(a)

objective 5x
Image size
X = 1242 µm
Y = 925 µm
Circles / Calotest
D1 = 459.93 µm
D2 = 572.30 µm
Ball diameter
20.000 mm
Layer thickness
LT = 1.450 µm

(b)

Figure 4.4: Optical micrograph illustrating calotest impression (a) CrAlN and (b) TiAlN

4.2 Mechanical and Tribological Characterization

This section presents the results of the microindentation test, scratch test, creep test and solid particle erosion of the coatings.

4.2.1 Microhardness

The results of microhardness, elastic modulus, crystallite size and thickness of the coatings are illustrated in Table 4.2.

Table 4.2: Mechanical Properties of the four arc evaporated nitride coatings.

	Microhardness (Hv)	Modulus (GPa)	Crystallite size (nm)	Thickness (μm)
AISI 304	329 ± 19	104 ± 6	-	-
CrN	1236 ± 92	187 ± 18	21 ± 3	1.82 ± 0.02
TiN	1591 ± 94	242 ± 10	22 ± 1	1.85 ± 0.04
CrAlN	2417 ± 65	313 ± 66	50 ± 2	1.83 ± 0.03
TiAlN	1926 ± 76	342 ± 36	39 ± 5	1.80 ± 0.02

4.2.2 Scratch

Scratch test was performed using linearly progressive load across the coated surface. The scratch resistance of the coatings was evaluated by utilizing acoustic emission signal. The increase in acoustic emission (AE) signal gives an indication of a crack event. The load at which the first crack event occurs is termed the critical load. This critical load is used as a means of characterizing the scratch resistance of the coatings.

The critical loads determined for the four nitrides coatings are shown in table 4.2. Figures 4.5 and 4.6 illustrates the critical loads and an optical micrograph of the entire scratch track for CrN, TiN, $CrAlN$ and $TiAlN$ coatings respectively.

The critical load (L_c) is a function of coating substrate adhesion, stylus tip radius, loading rate, mechanical properties of both the coating and the substrate, and the residual stresses in the coating.

The morphologies of the coatings after being scratched with a linearly progressive load of 10 N are illustrated in the SEM micrographs in Figure 4.7 and further magnified in Figure 4.8.

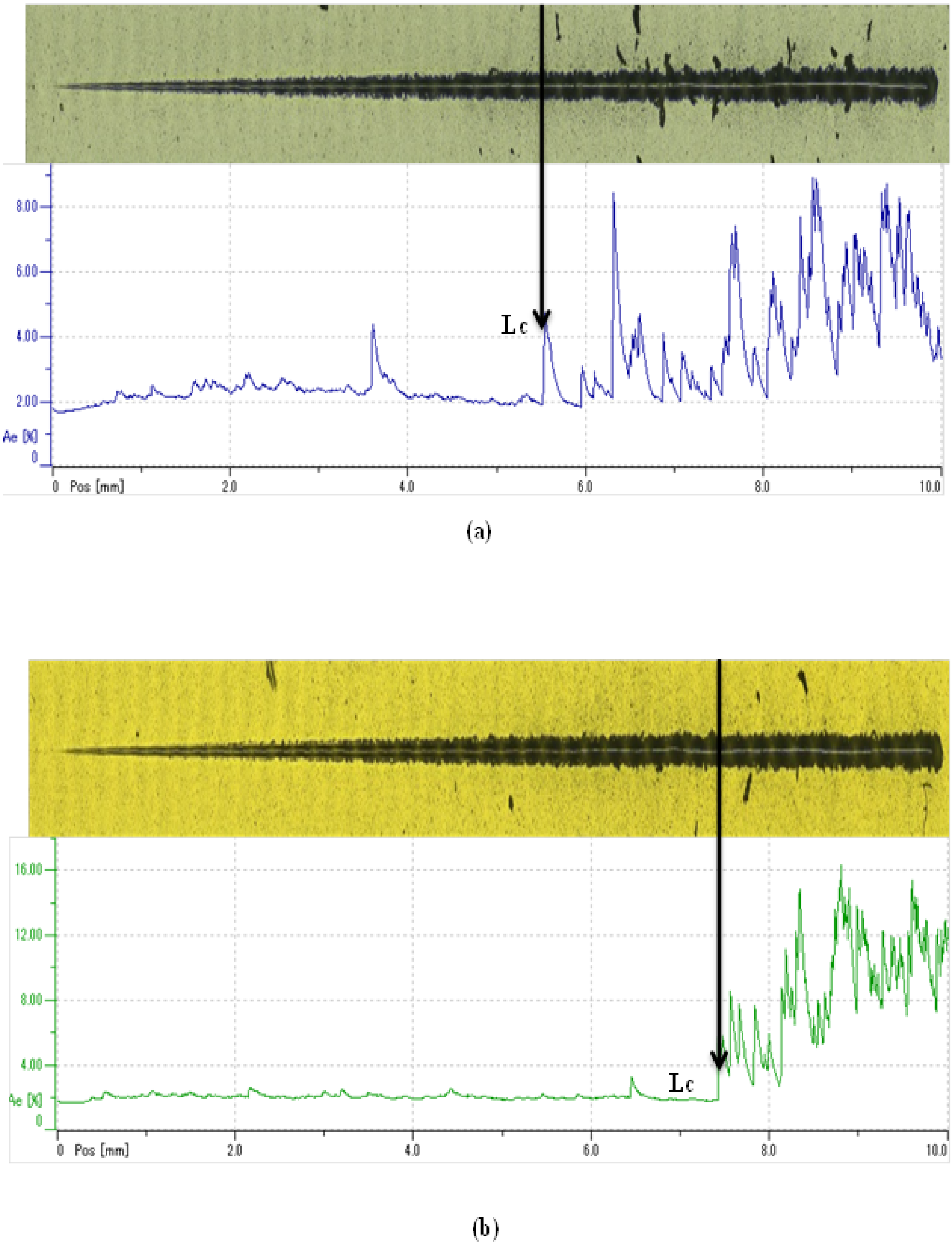

(a)

(b)

Figure 4.5: Scratch track with acoustic emission signal showing critical load (a) CrN and (b) TiN

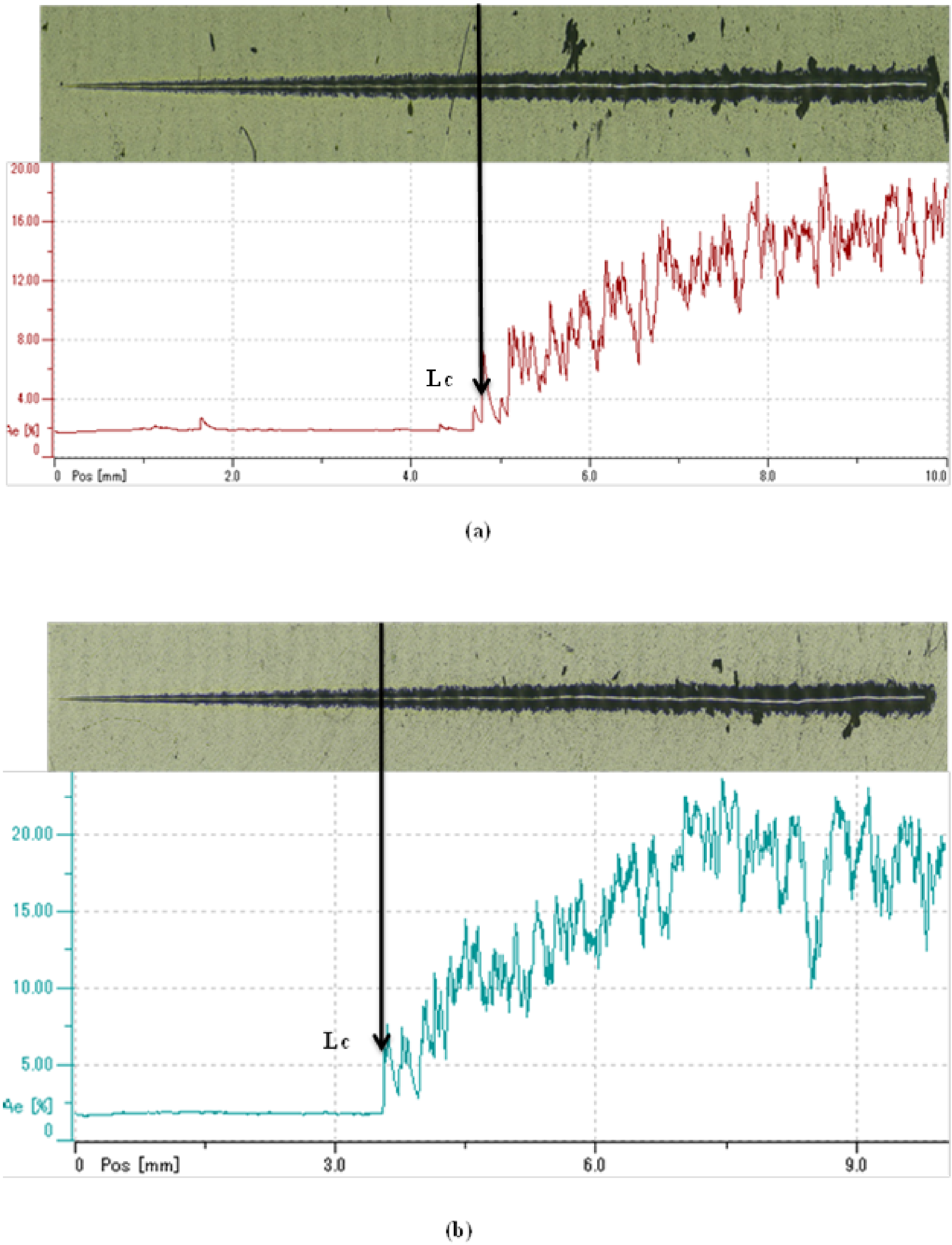

Figure 4.6: Scratch track with acoustic emission signal showing critical load (a) CrAlN and (b) TiAlN

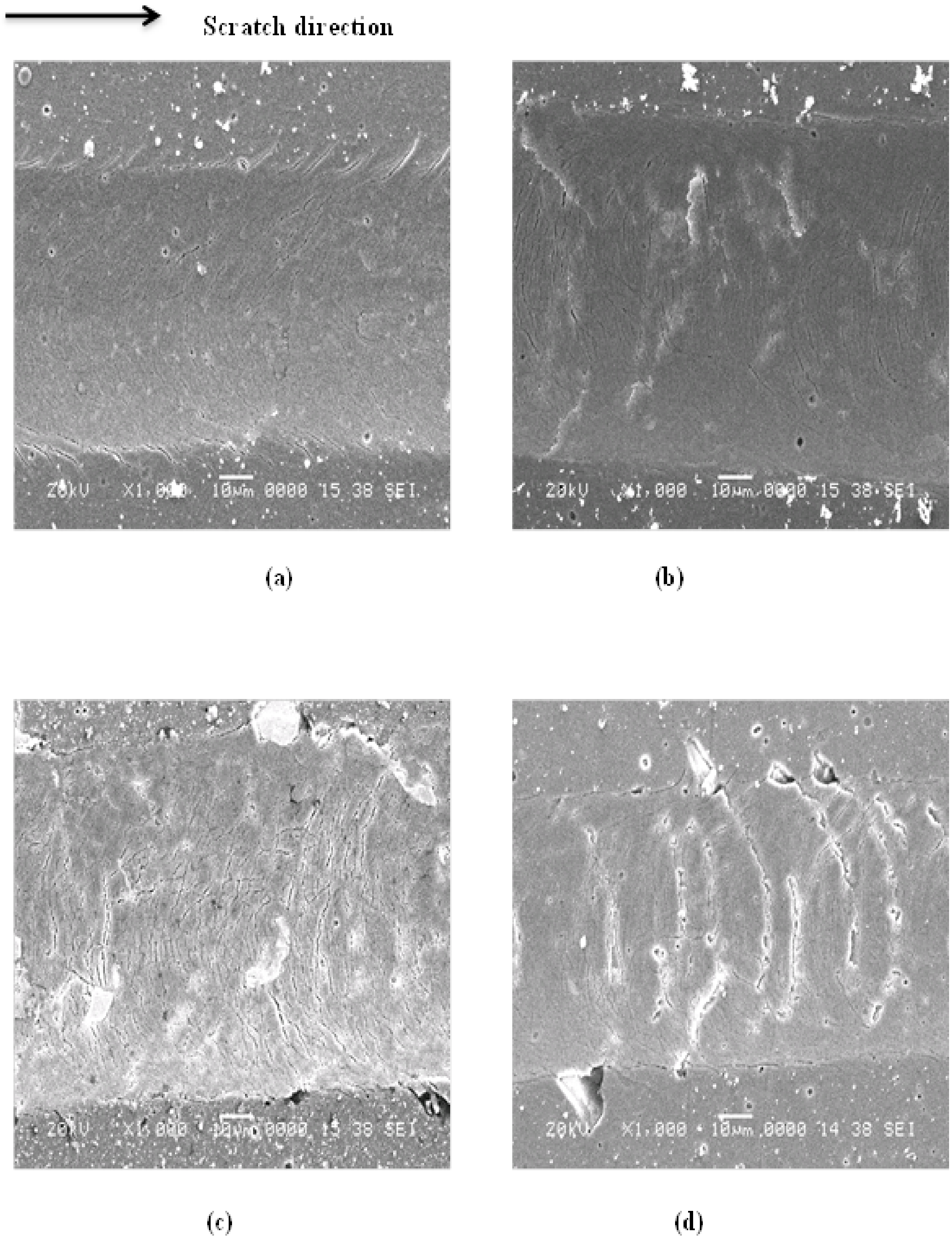

(a) (b)

(c) (d)

Figure 4.7: SEM micrograph showing the scratch track (a) CrN, (b) TiN, (c) CrAlN and (d) TiAlN

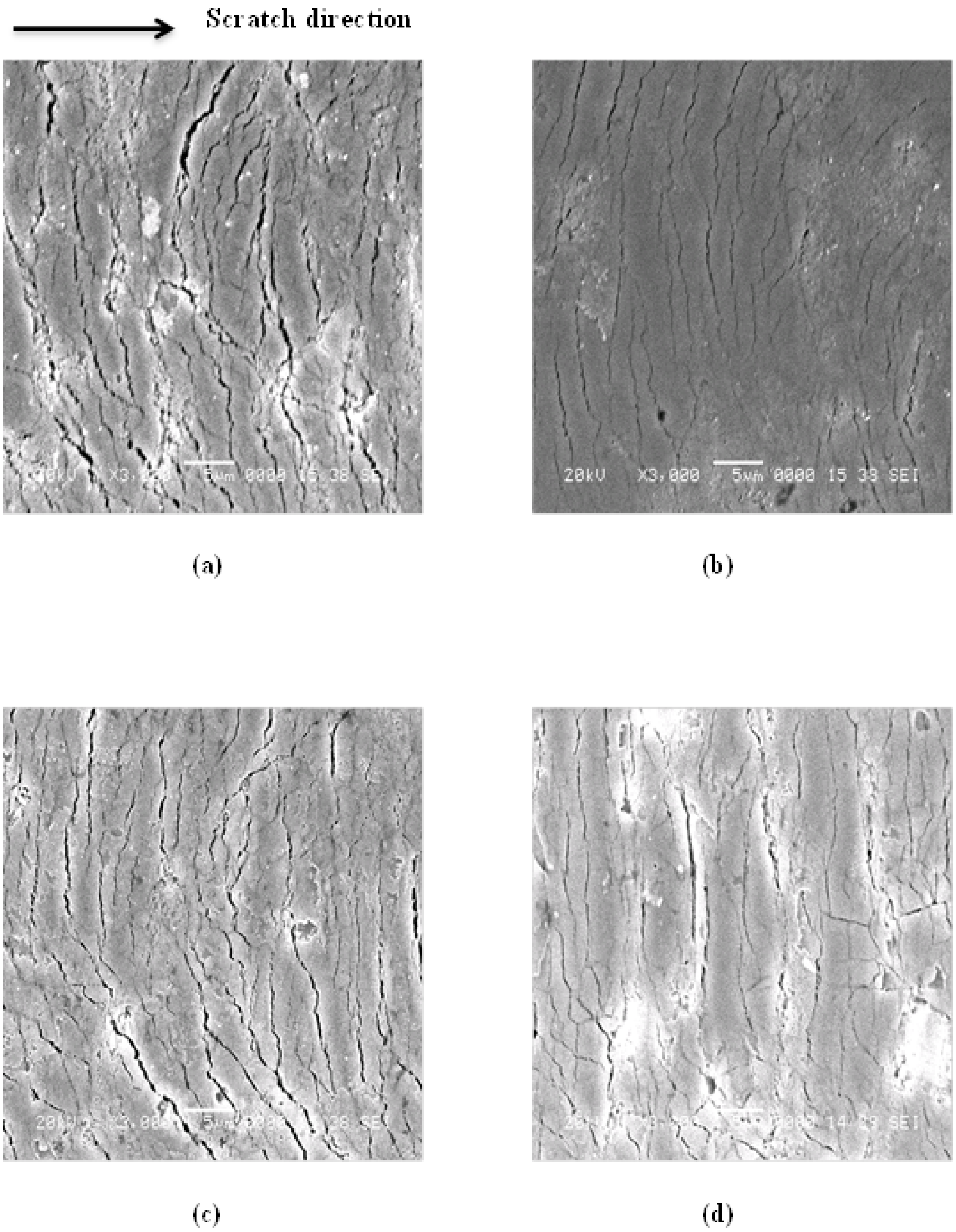

Figure 4.8: SEM micrograph at the critical load showing the various cracks (a) CrN, (b) TiN, (c) CrAlN and (d) TiAlN

The coefficient of friction was evaluated along the scratch track. The reported values were evaluated up to the critical load of each coating as illustrated in Figure 4.9.

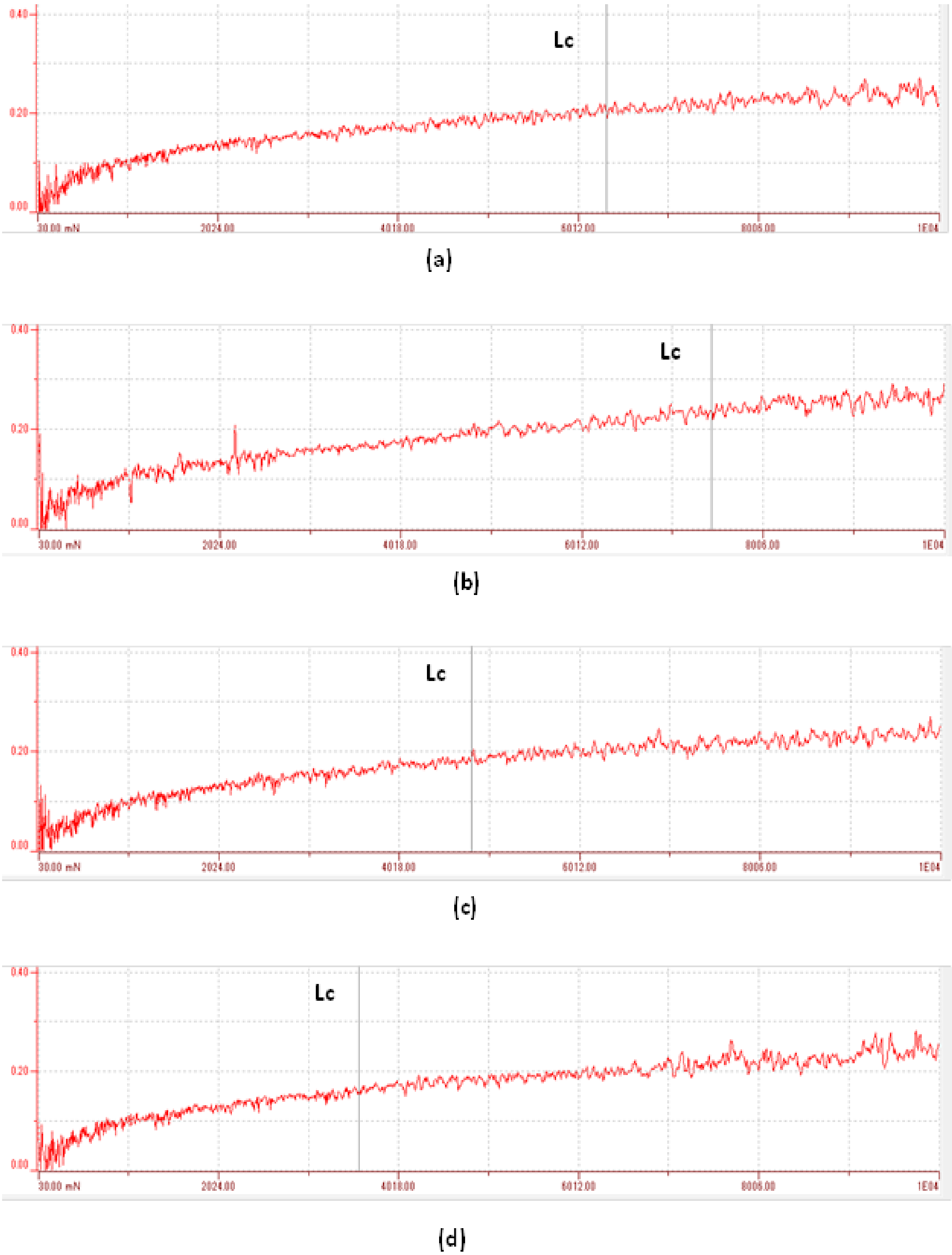

Figure 4.9: Coefficient of friction along the entire scratch track of (a) CrN, (b) TiN, (c) CrAlN, and (d) TiAlN coatings

Table 4.3: Critical loads and coefficient of friction for the coatings after scratch.

Coating	Critical load (N)	Friction Coefficient (μ)
CrN	5.67 ± 0.6	0.21 ± 0.01
TiN	6.60 ± 0.7	0.24 ± 0.03
CrAlN	4.80 ± 0.3	0.19 ± 0.03
TiAlN	3.57 ± 0.4	0.16 ± 0.01

4.2.3 Creep

Indentation creep measurements were taken at three different temperatures, $(50^oC, 75^oC, 100^oC)$. Three different loads $(15, 20$ and $25mN)$ were used at each temperature. Figures 4.10 and 4.11 illustrates a typical loading and unloading curves with penetration depth plots super imposed for CrN, TiN, $CrAlN$ and $TiAlN$ coatings respectively.

The variation in penetration depth during the hold period was extracted from the penetration depth plots and further plotted as shown in Figures 4.12 to **??** for all temperatures (50^oC, 75^oC, 100^oC) and loads (15, 20 and $25mN$).

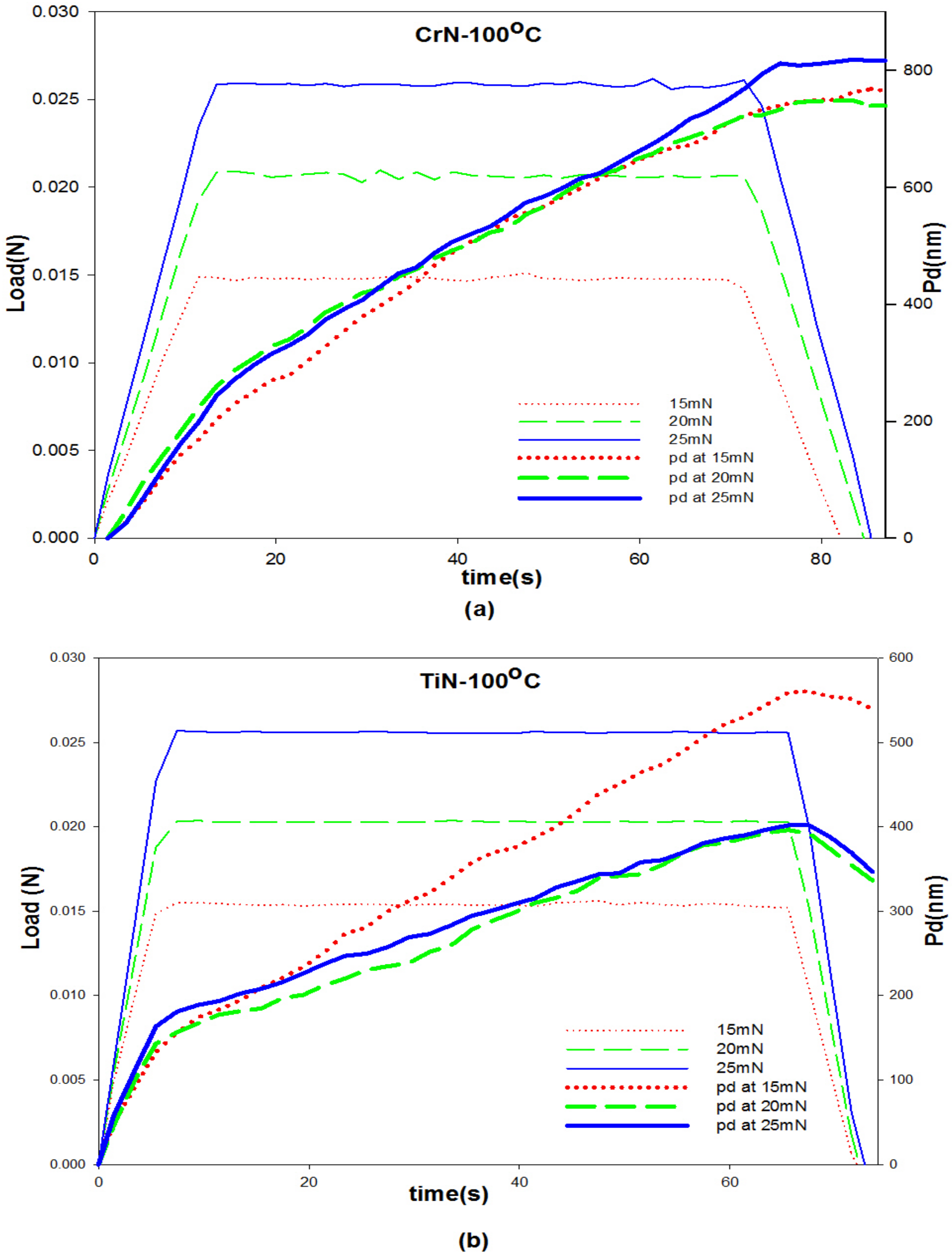

Figure 4.10: Typical penetration depth (Pd) with time, loading and unloading curve (a) CrN and (b) TiN

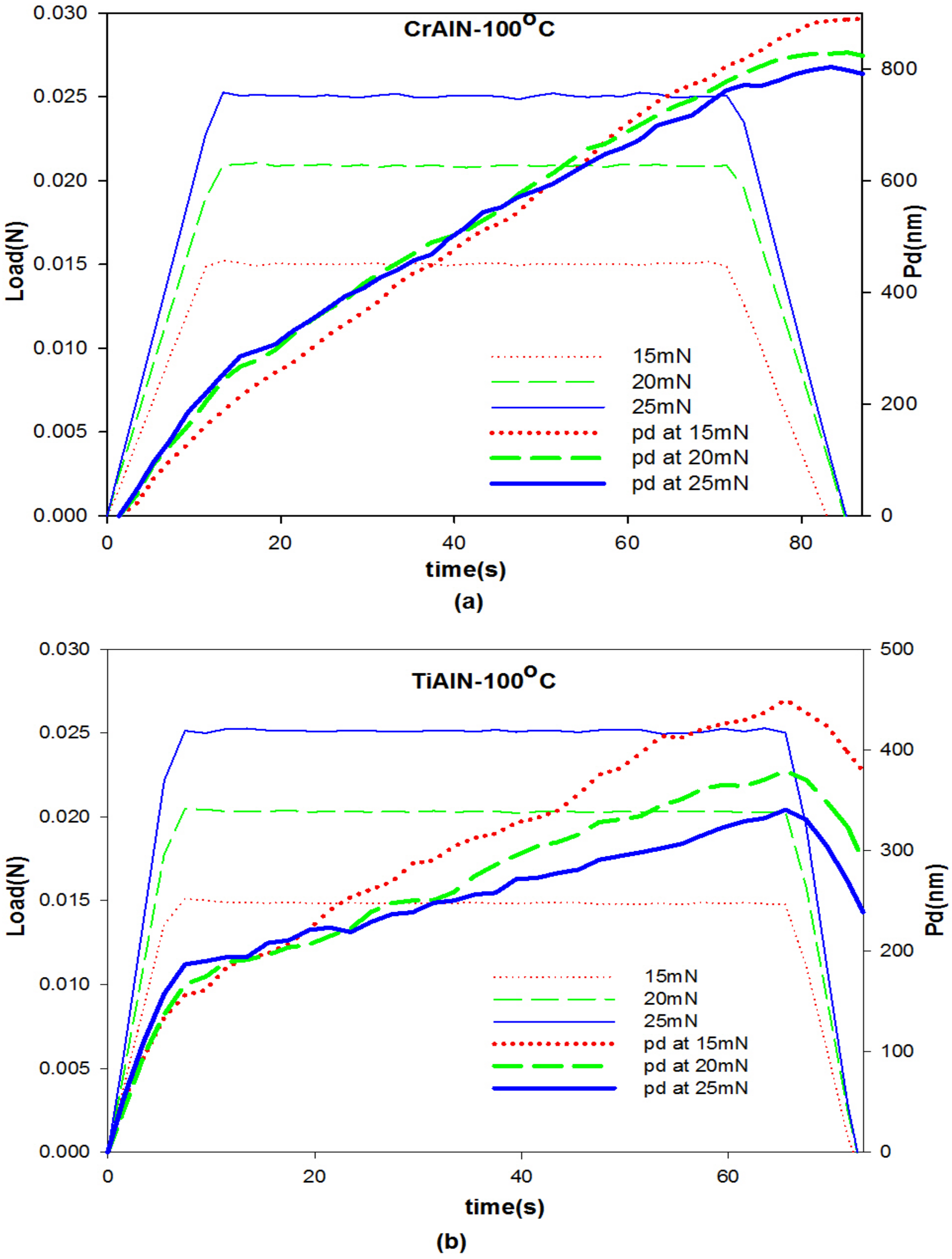

Figure 4.11: Typical penetration depth (Pd) with time, loading and unloading curve (a) CrAlN and (b) TiAlN

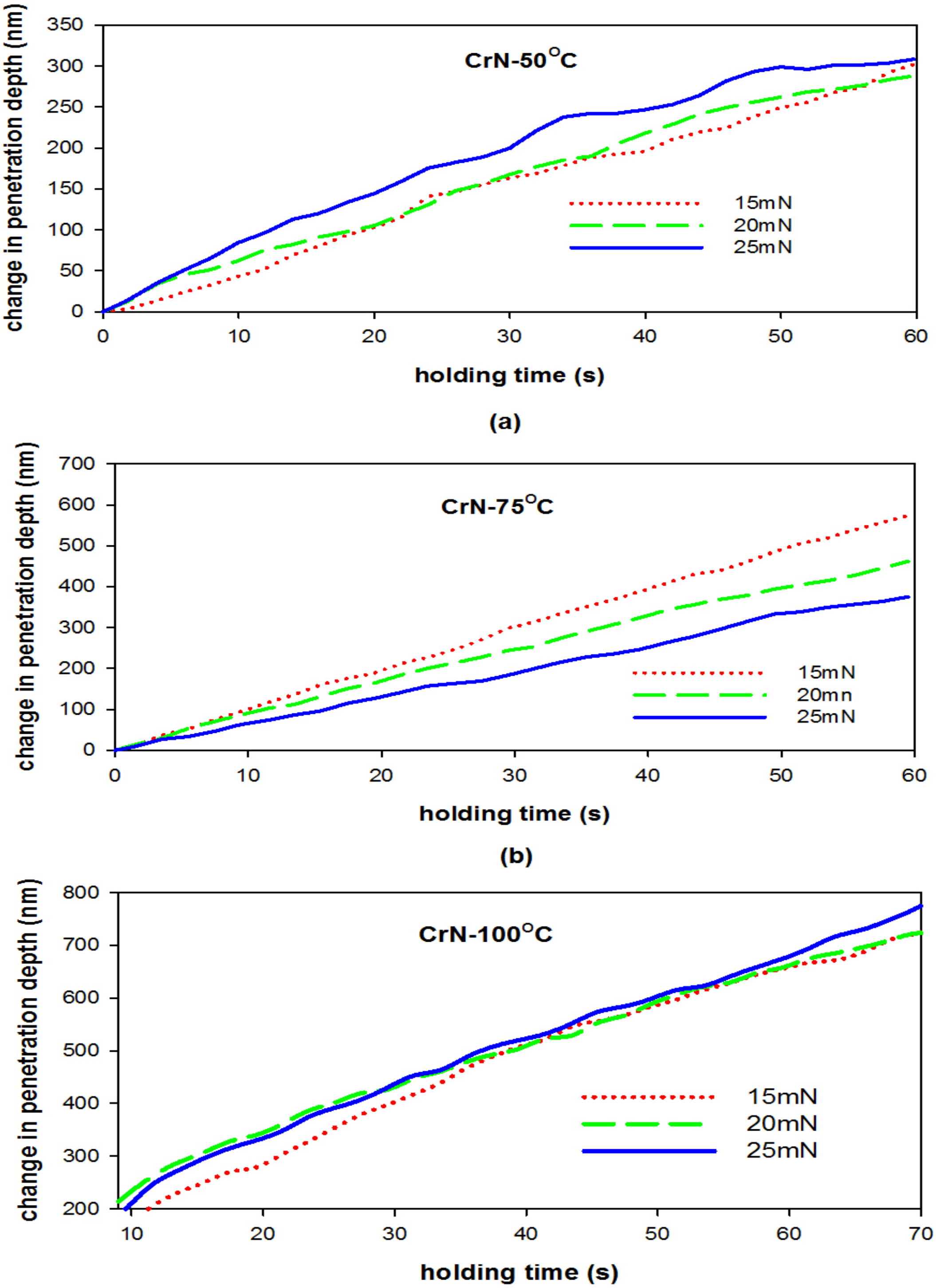

(a)

(b)

(c)

Figure 4.12: Variation of penetration depth with load- holding time of CrN at (a) 50^oC (b) 75^oC and (c) 100^oC

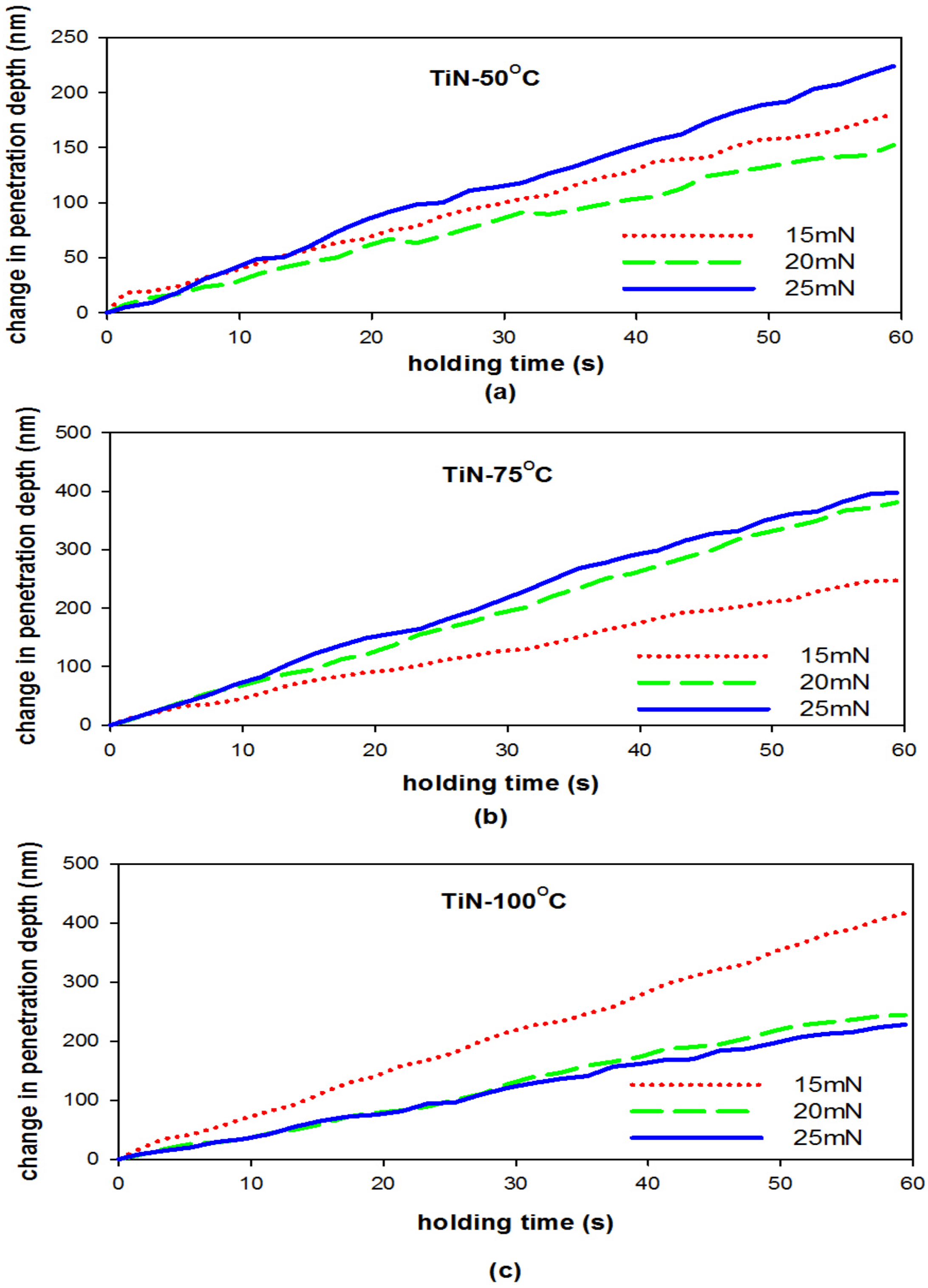

Figure 4.13: Variation of penetration depth with load -holding time of TiN at (a) 50^oC (b) 75^oC and (c) 100^oC

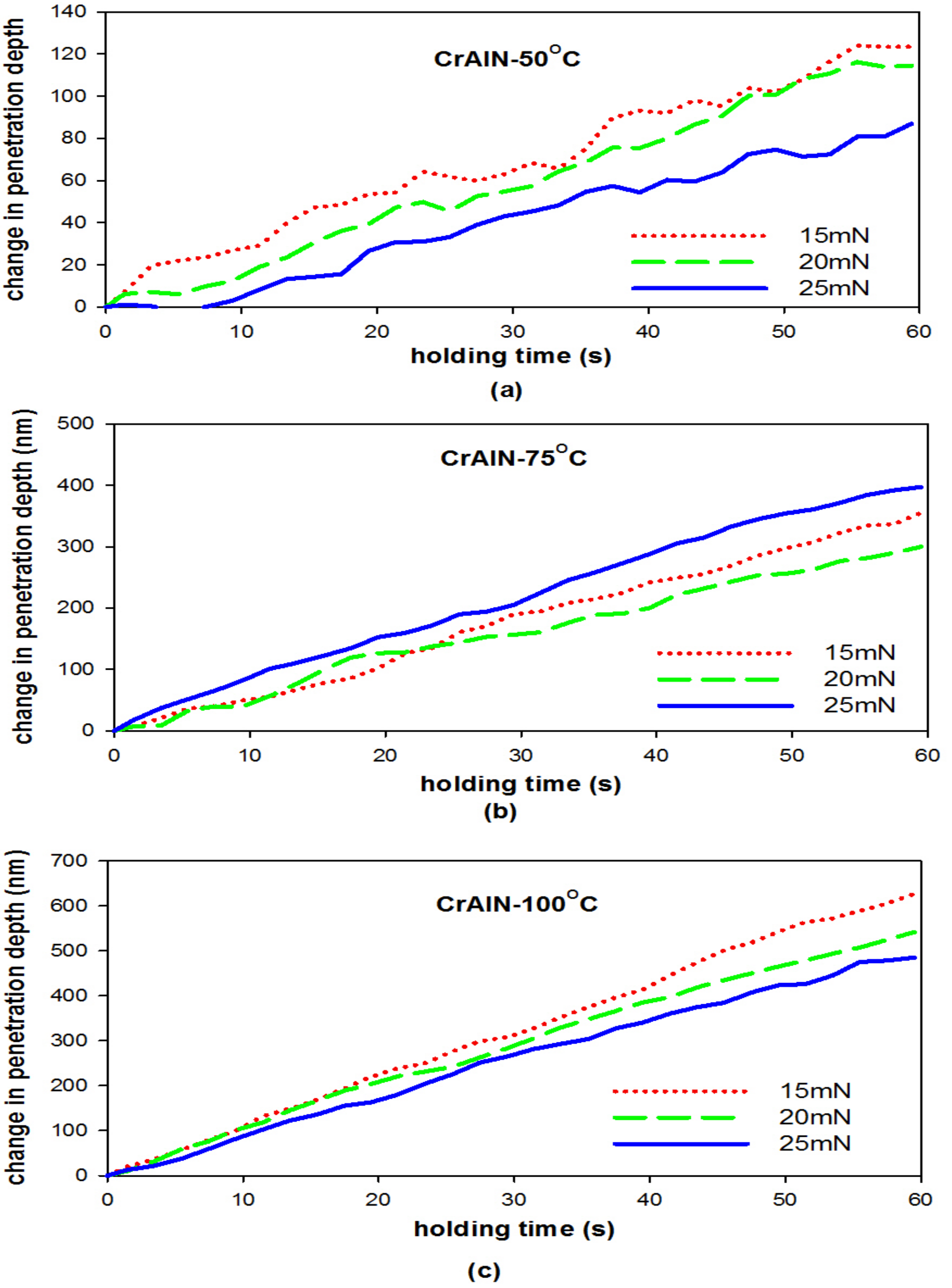

(a)

(b)

(c)

Figure 4.14: Variation of penetration depth with load-holding time of CrAlN at (a) $50^o C$ (b) $75^o C$ and (c) $100^o C$

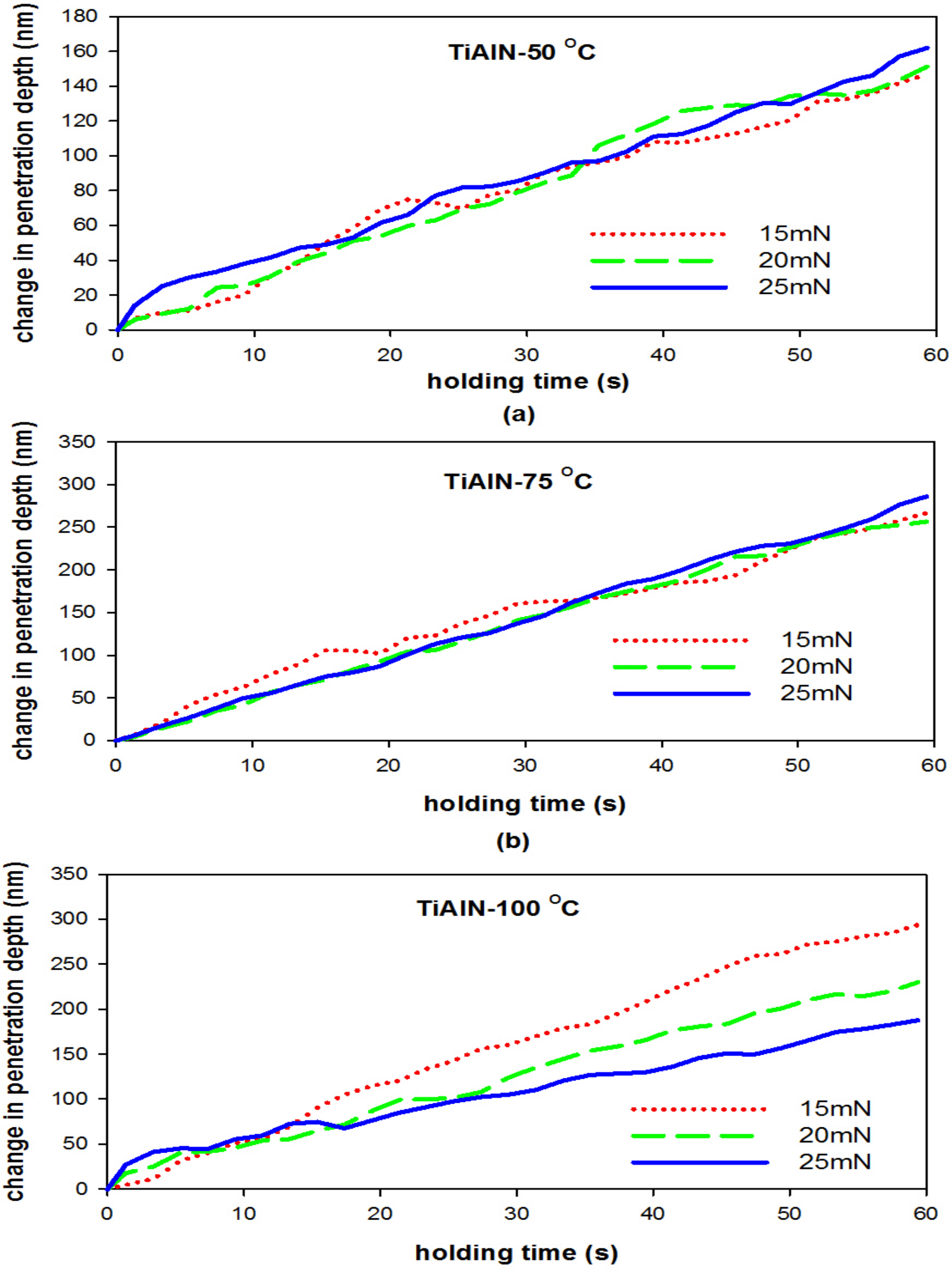

(a)

(b)

(c)

Figure 4.15: Variation of penetration depth with load-holding time of TiAlN at (a) 50^oC (b) 75^oC and (c) 100^oC

The strain rates evaluated from the creep curves above are summarized in Table 4.4. The strain rates were evaluated using equation 2.4 in section 2.2.

Table 4.4: Strain rate for the nitride coatings at loads of 15, 20 and 25 mN

Temperature (^oC)	Load (mN)	Strain Rate (s^{-1})			
		CrN	TiN	CrAlN	TiAlN
50	15	0.019	0.021	0.014	0.014
	20	0.018	0.019	0.012	0.018
	25	0.018	0.022	0.008	0.014
75	15	0.025	0.035	0.031	0.029
	20	0.023	0.035	0.019	0.032
	25	0.026	0.033	0.023	0.031
100	15	0.032	0.049	0.040	0.038
	20	0.029	0.045	0.028	0.039
	25	0.026	0.043	0.025	0.030

The activation energies for creep were estimated from a semi logarithm plot of strain rate and inverse temperature. These are illustrated in Figures 4.16 and 4.17 for the coatings respectively. The stress exponents were also evaluate by plotting strain rate with the mean stress using equations 2.3 and 2.4 in section 2.2. These are illustrated in Figures 4.18 and 4.19 for the coatings respectively.

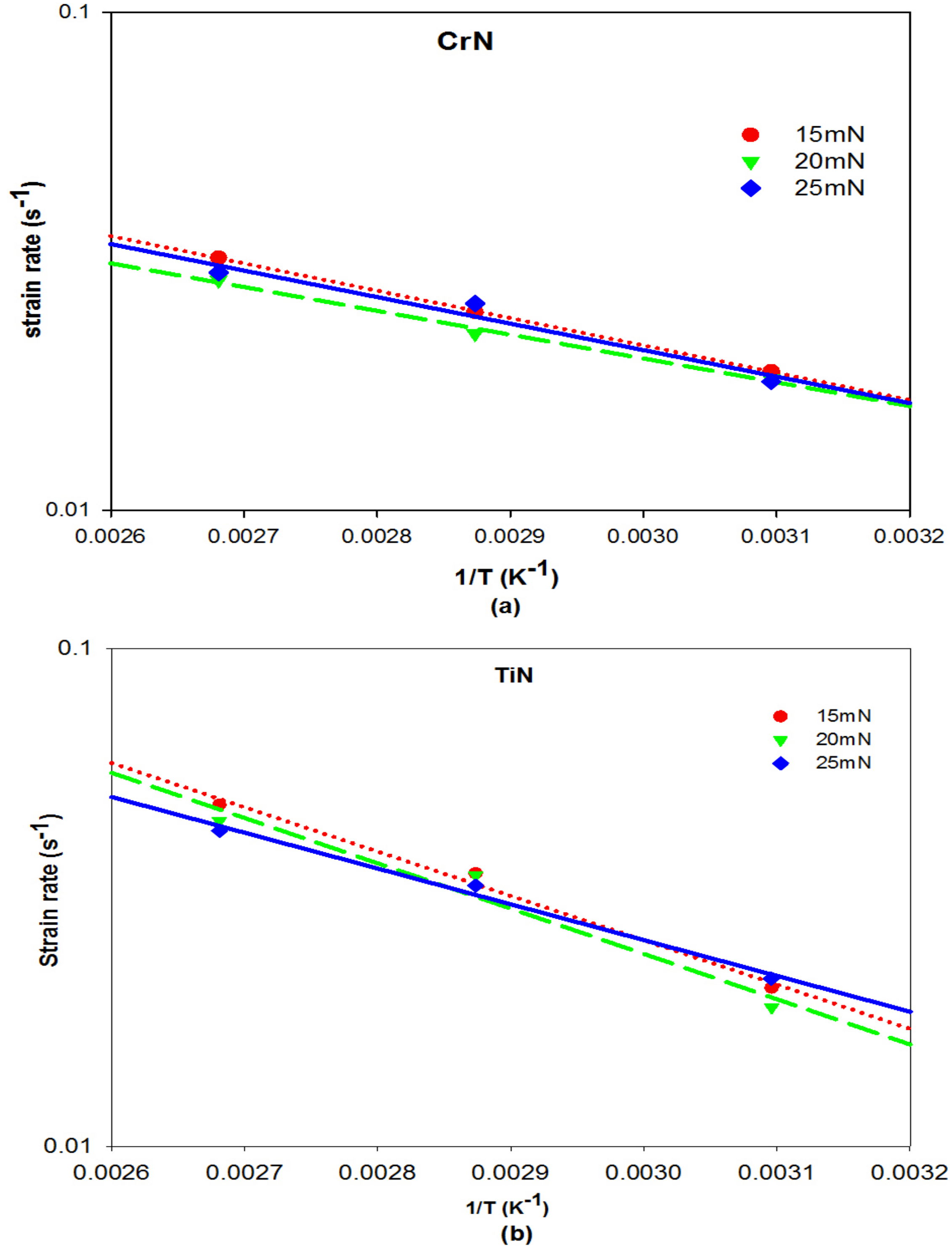

Figure 4.16: Determination of activation energy for creep from a plot of strain rate with inverse of temperature (a) CrN and (b) TiN

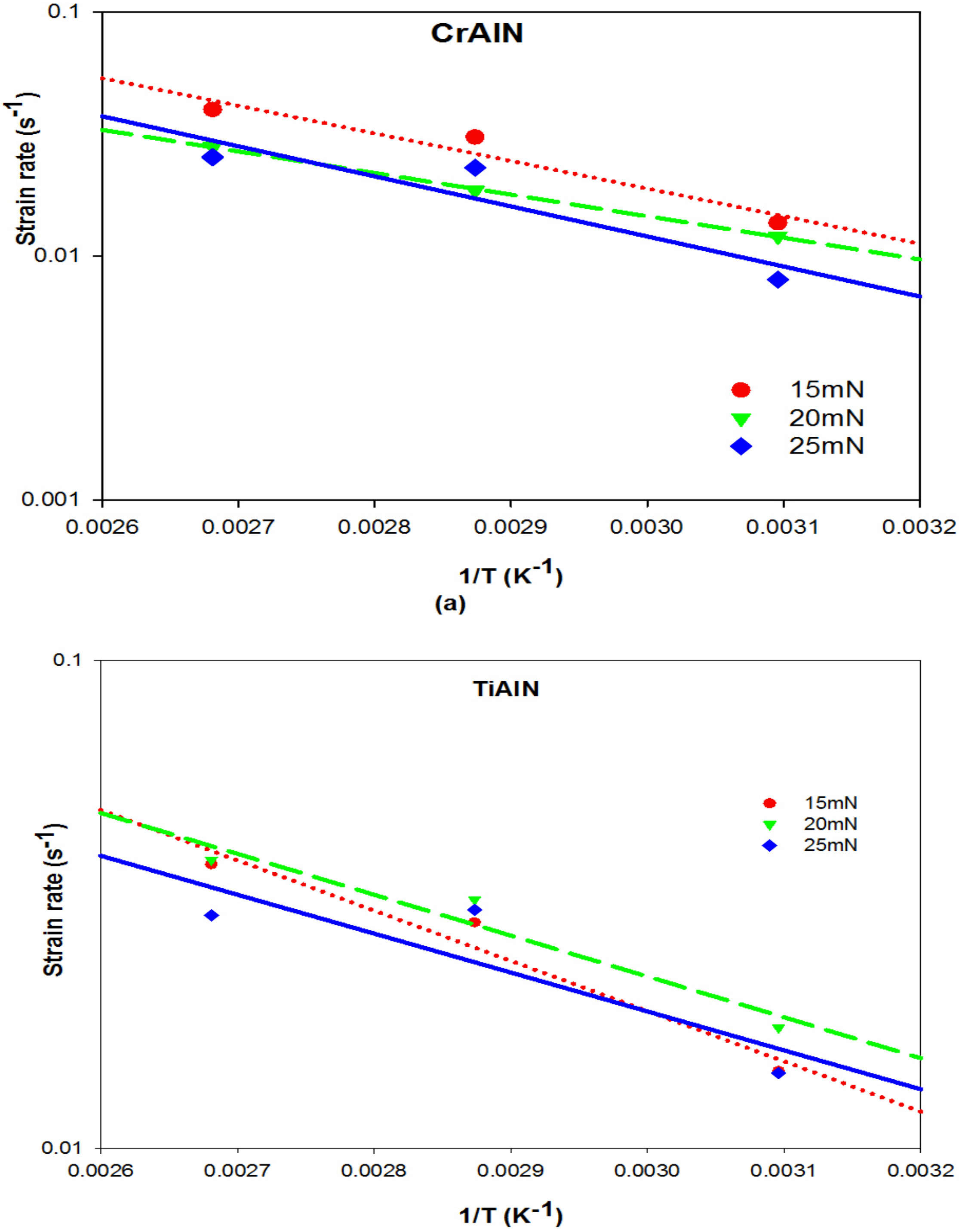

(a)

(b)

Figure 4.17: Determination of activation energy for creep from a plot of strain rate with inverse of temperature (a) CrAlN and (b) TiAlN

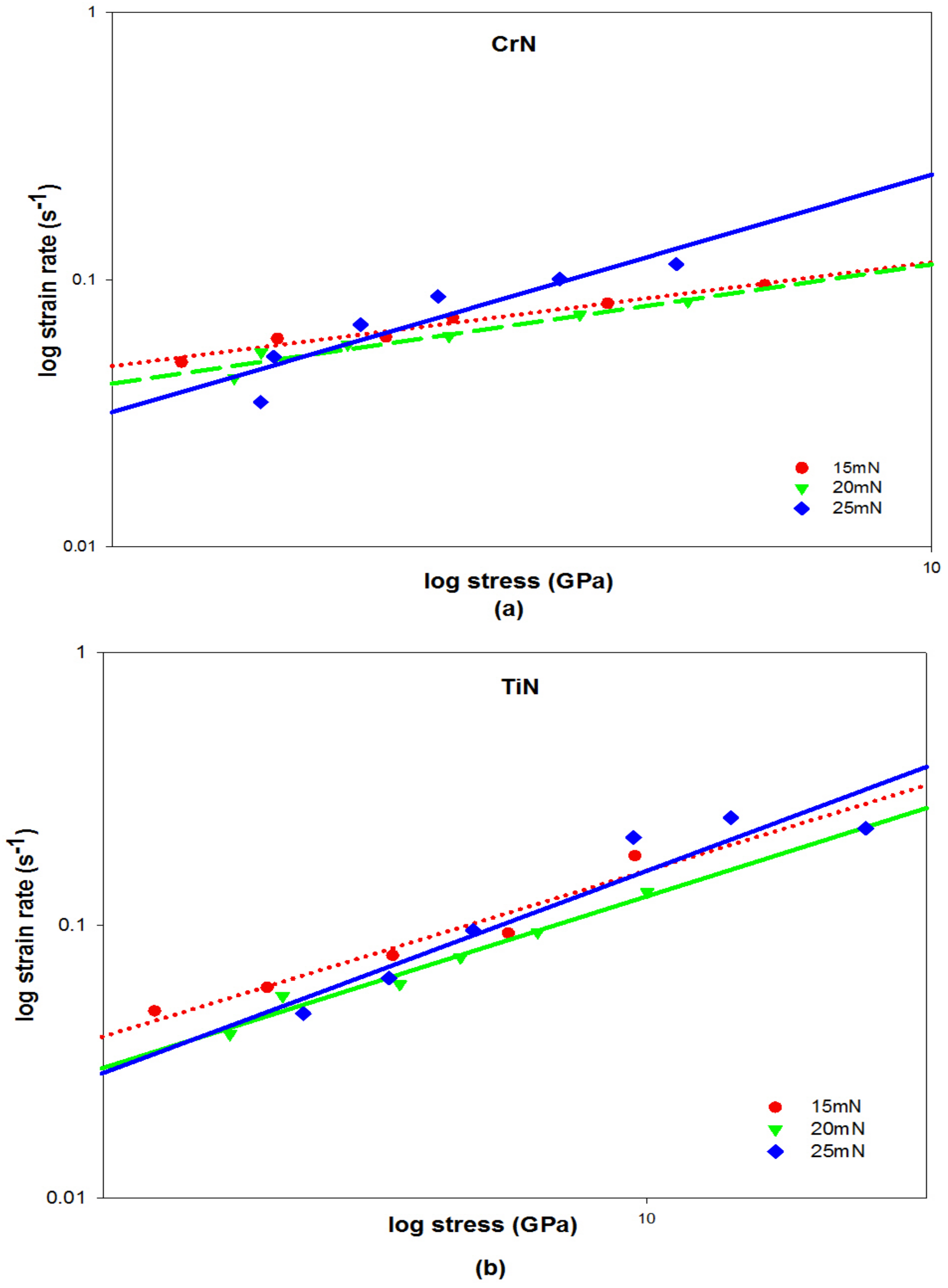

(a)

(b)

Figure 4.18: Stress exponent of (a) CrN and (b) TiN at 15, 20 and 25 mN respectively ($50^{o}C$)

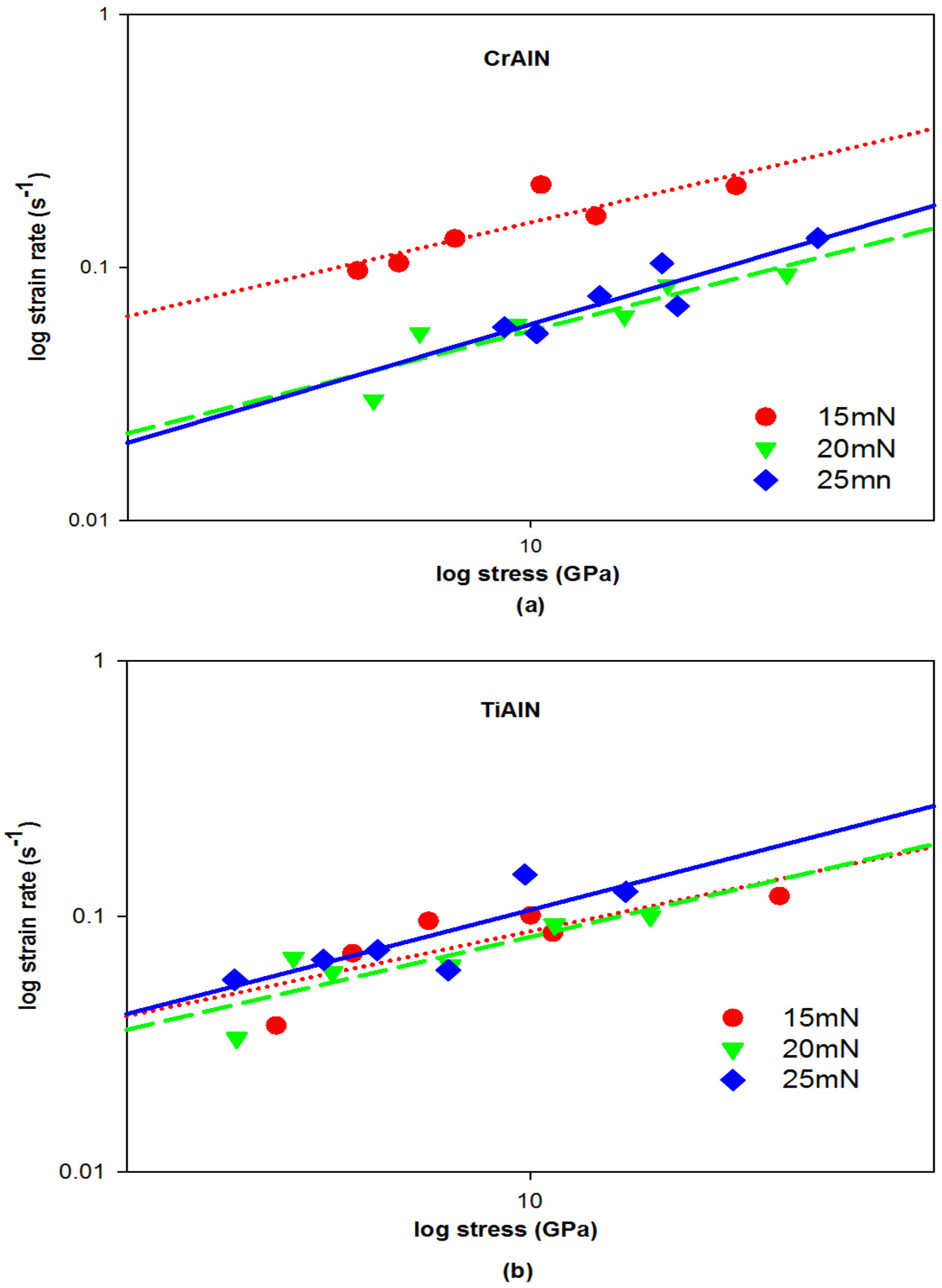

Figure 4.19: Stress exponent of (a) CrAlN and (b) TiAlN at 15, 20 and 25mN respectively $(50 - 100^{o}C)$

The activation energies and stress exponents evaluated are presented in Table 4.4.

Table 4.5: The activation energies and stress exponents calculated for the four coatings.

Coating	Activation Energy (KJ/mol)	Stress Exponent
CrN	10 ± 2	0.82 ± 0.2
TiN	16 ± 6	1.66 ± 0.4
CrAlN	21 ± 4	1.41 ± 0.6
TiAlN	17 ± 2	1.22 ± 0.3

4.2.4 Erosion

The results of the room temperature erosion test conducted using angular alumina particles are presented in this section. Figure 4.20 shows the SEM micrograph of the angular alumina particles used at low and high magnifications.

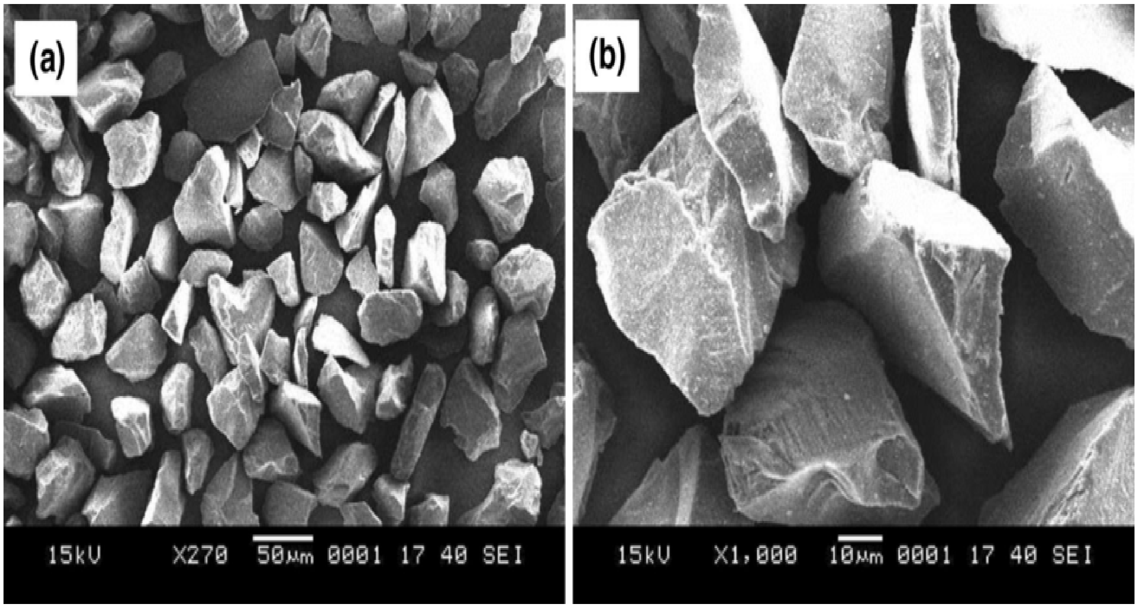

Figure 4.20: SEM micrograph of alumina particles $50\mu m$ averaged size used for solid particle erosion

Figures 4.21 and 4.22 illustrates the average mass losses of CrN, TiN, CrAlN and TiAlN coatings at four impingement angles for the $150s$ and $600s$ erosion operations respectively. The variation of erosion rate with impingement angles are illustrated in Figure 4.23 **a** and **b** for initial and intermediate erosion operations respectively. SEM morphology of the erosion scar for the four nitride coatings and 304 stainless steel are presented in Figure 4.24, 4.25 and 4.26 at 30^o and 90^o impingement angles respectively.

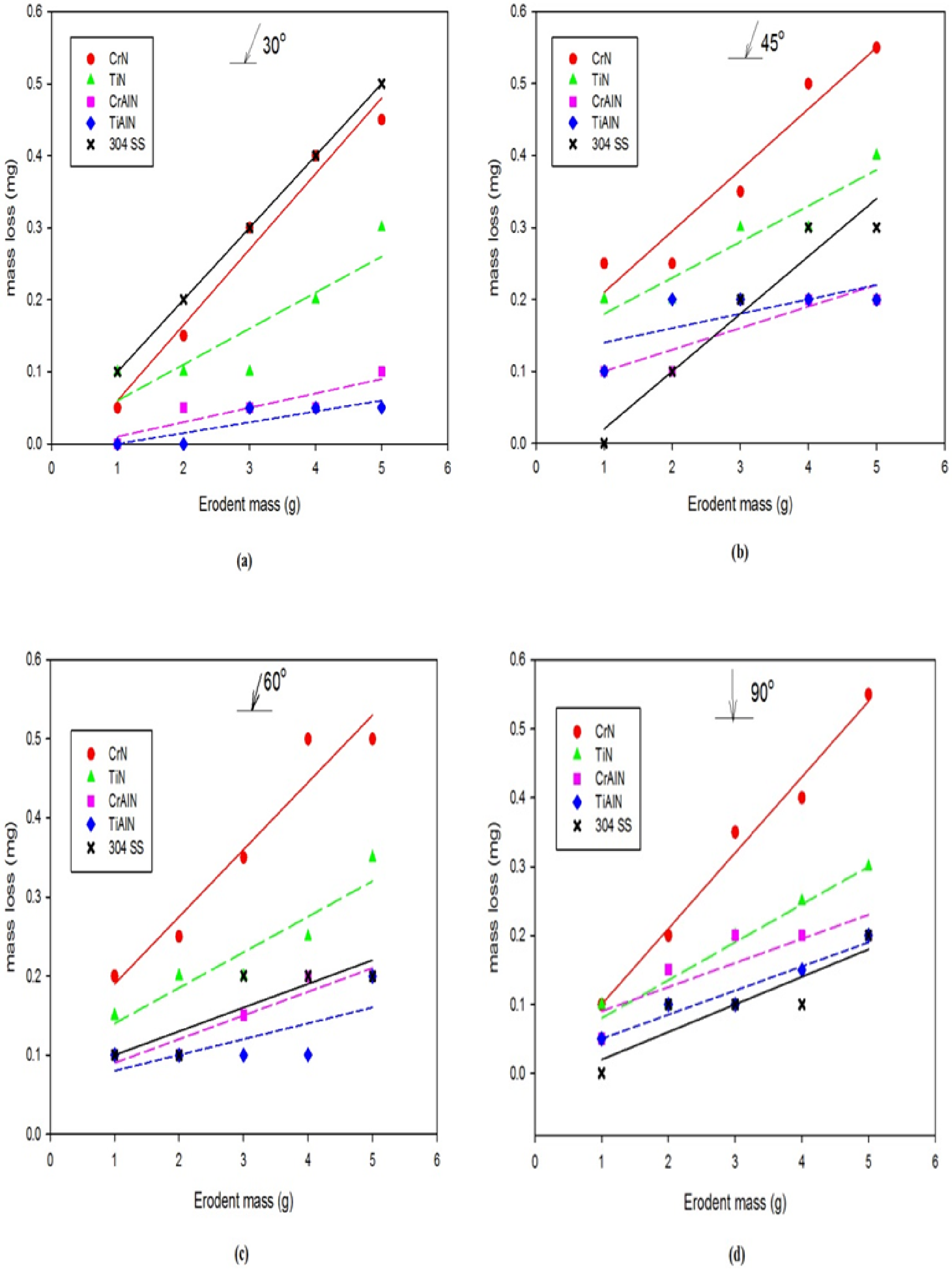

(a) (b) (c) (d)

Figure 4.21: Variation of mass loss with erodent mass at (a) 30^o, (b) 45^o, (c) 60^o, (d) 90^o after 150 seconds

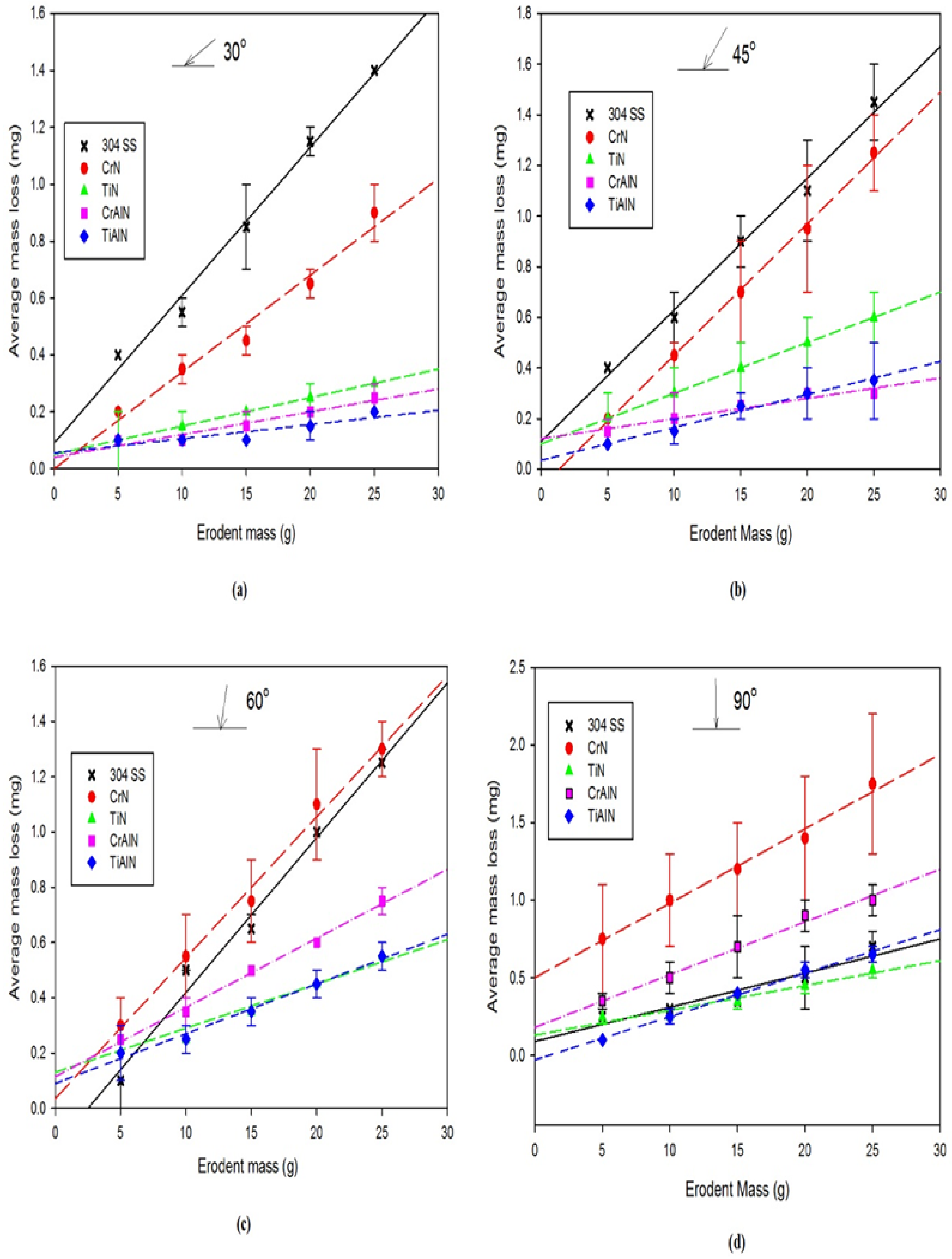

Figure 4.22: Variation of mass loss with erodent mass at (a) 30^o, (b) 45^o, (c) 60^o and (d) 90^o impingement angles after 600 seconds erosion operation.

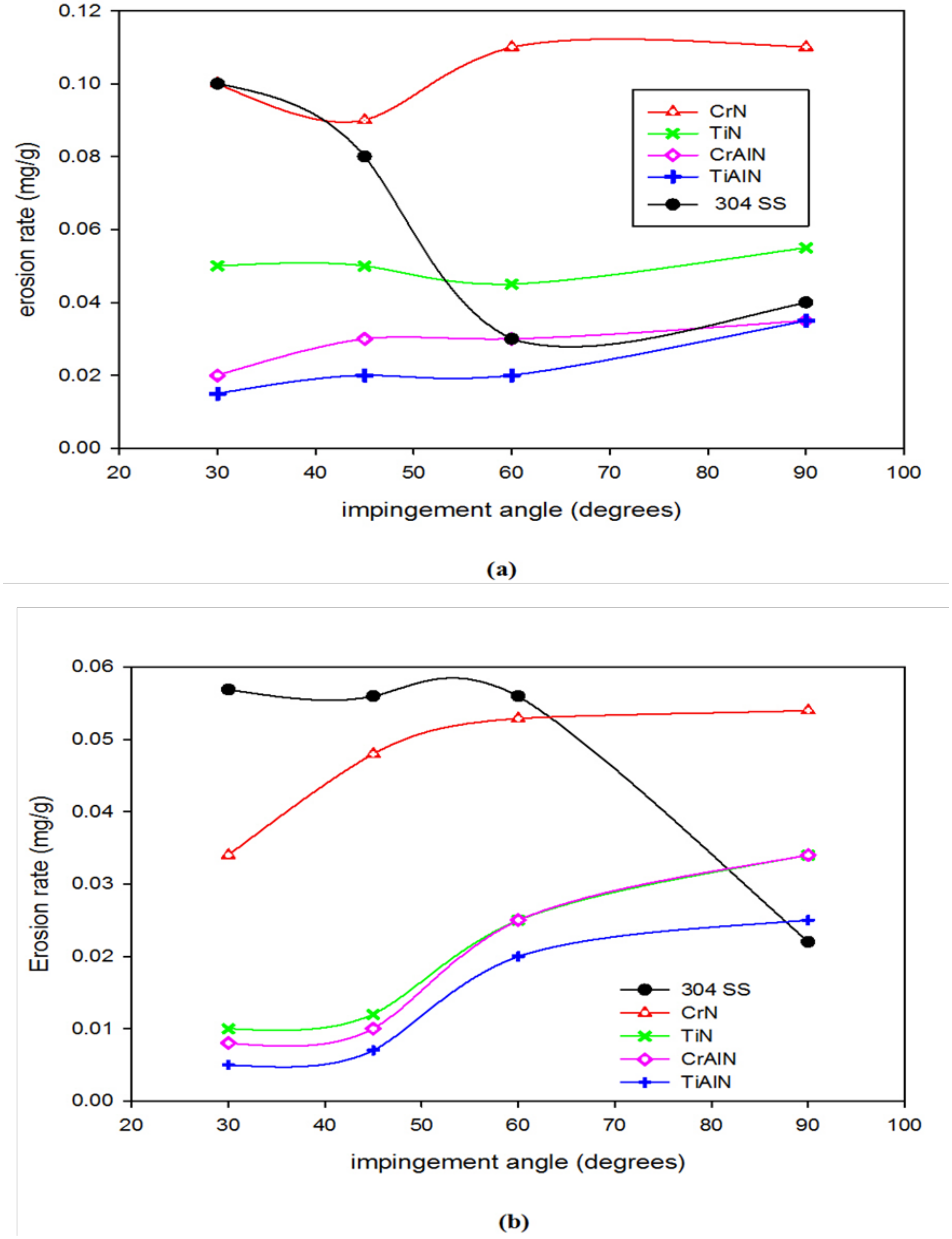

Figure 4.23: Variation of erosion rate with impingement angle after (a) 150 seconds and (b) 600 seconds erosion operation

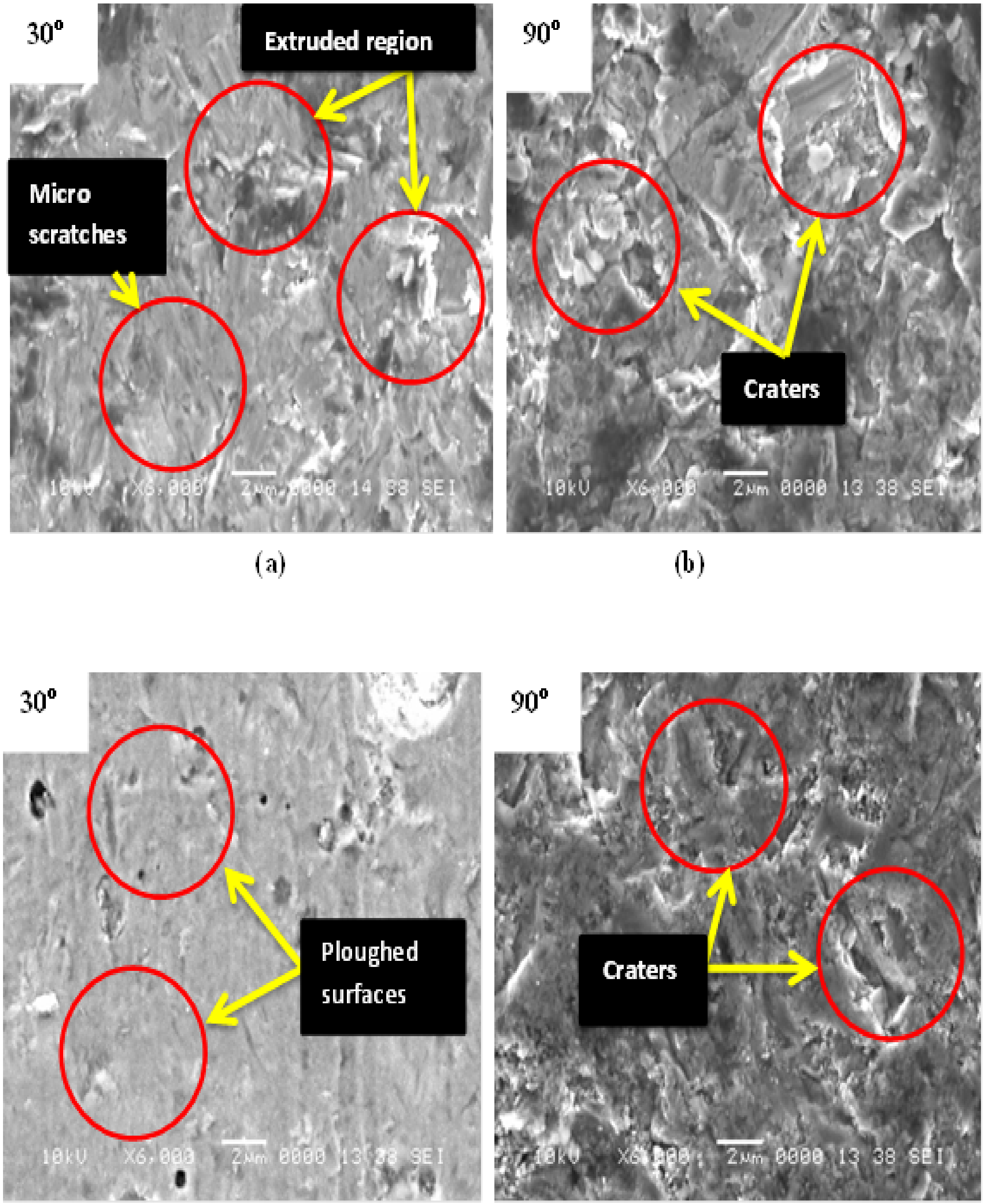

(a) (b)

(c) (d)

Figure 4.24: SEM micrograph of CrN at (a)30^o (b) 90^o and TiN at (c)30^o (d) 90^o after $150s$ erosion operations respectively.

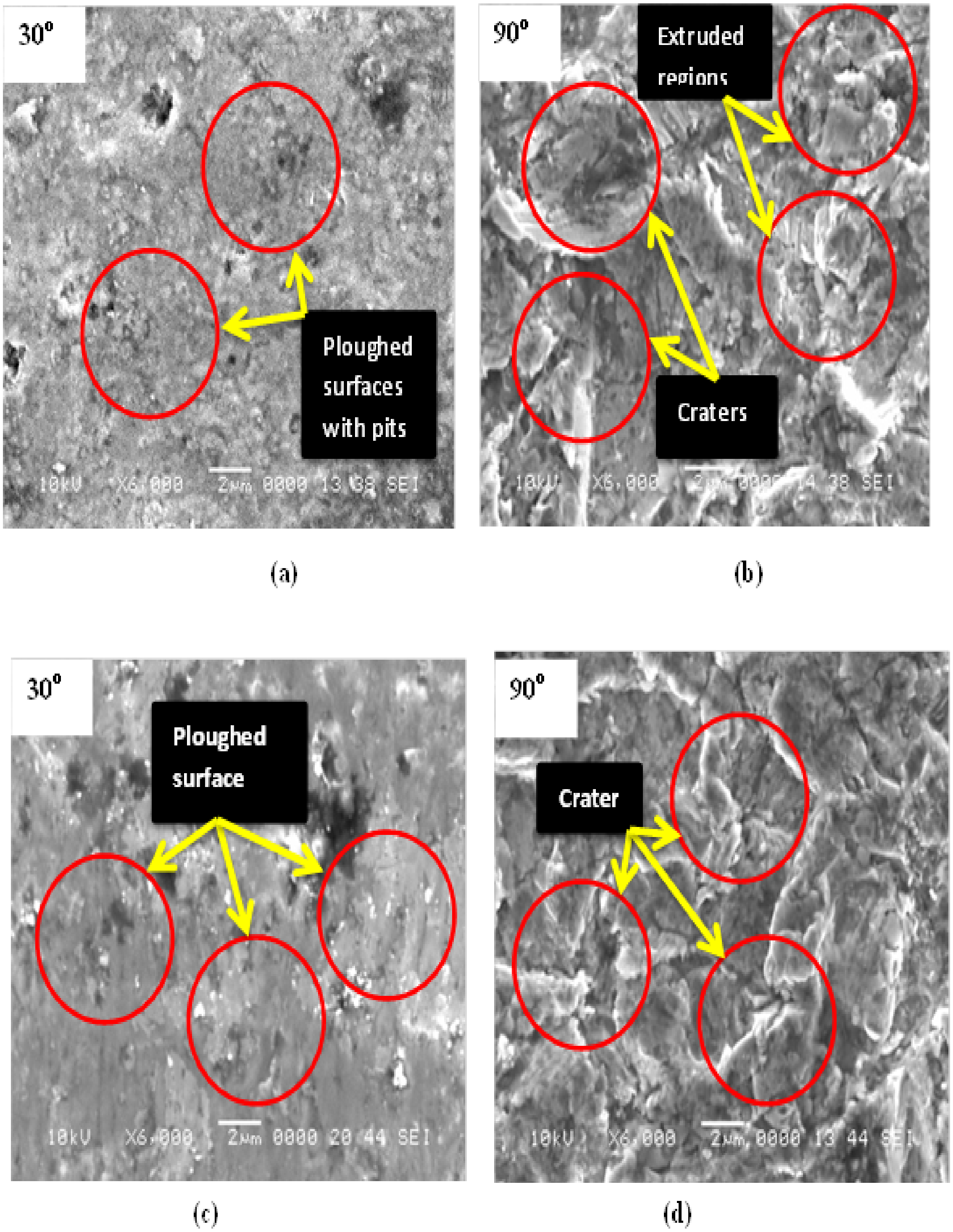

Figure 4.25: SEM micrograph of CrAlN at (a)30^o (b) 90^o and TiAlN at (c)30^o (d) 90^o after $150s$ erosion operations respectively.

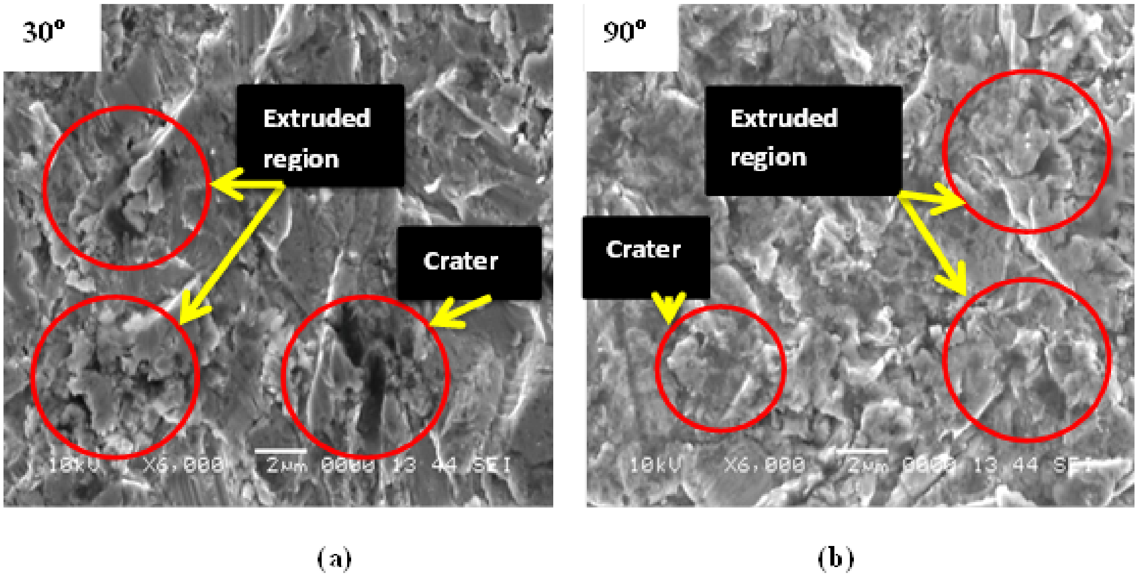

Figure 4.26: SEM micrograph of 304 stainless steel at (a) 30^o (b) 90^o after 150s erosion operation.

4.2.5 Effect of Residual Stress

The effect of residual stress on the hardness and scratch resistance of the coatings was evaluated after annealing. The XRD patterns of the annealed coatings are illustrated in Figure 4.27. Figure 4.28 and 4.29 illustrates the scratch and acoustic emission signal indicating the critical loads after annealing. The residual stress and mechanical properties of the annealed coatings are illustrated in Table 4.5.

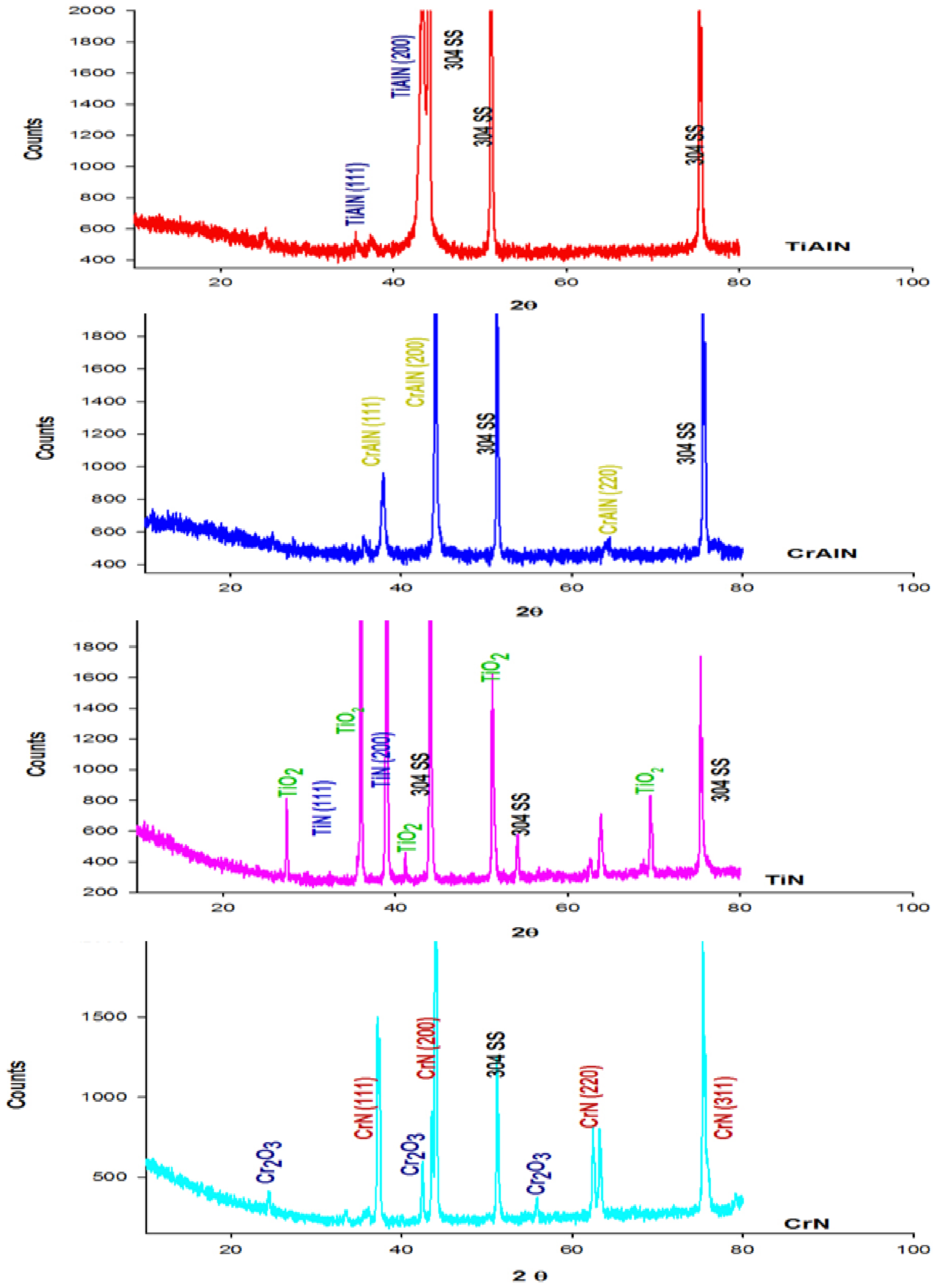

Figure 4.27: XRD pattern of the annealed coatings at 800^{o}C for 2 hours

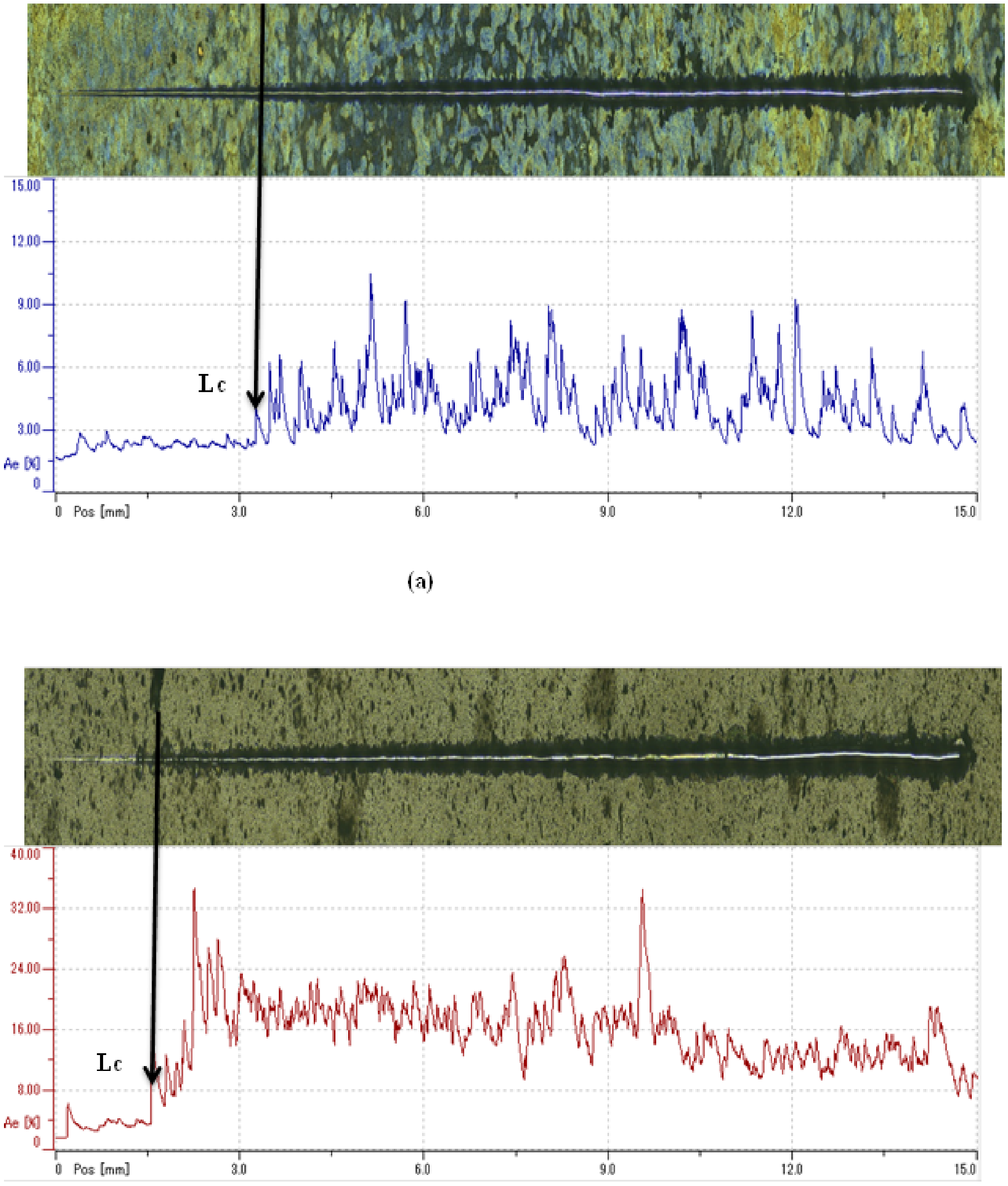

(a)

(b)

Figure 4.28: Scratch track of (a) CrN and (b) TiN coatings after annealing at 800^oC for 2 hours

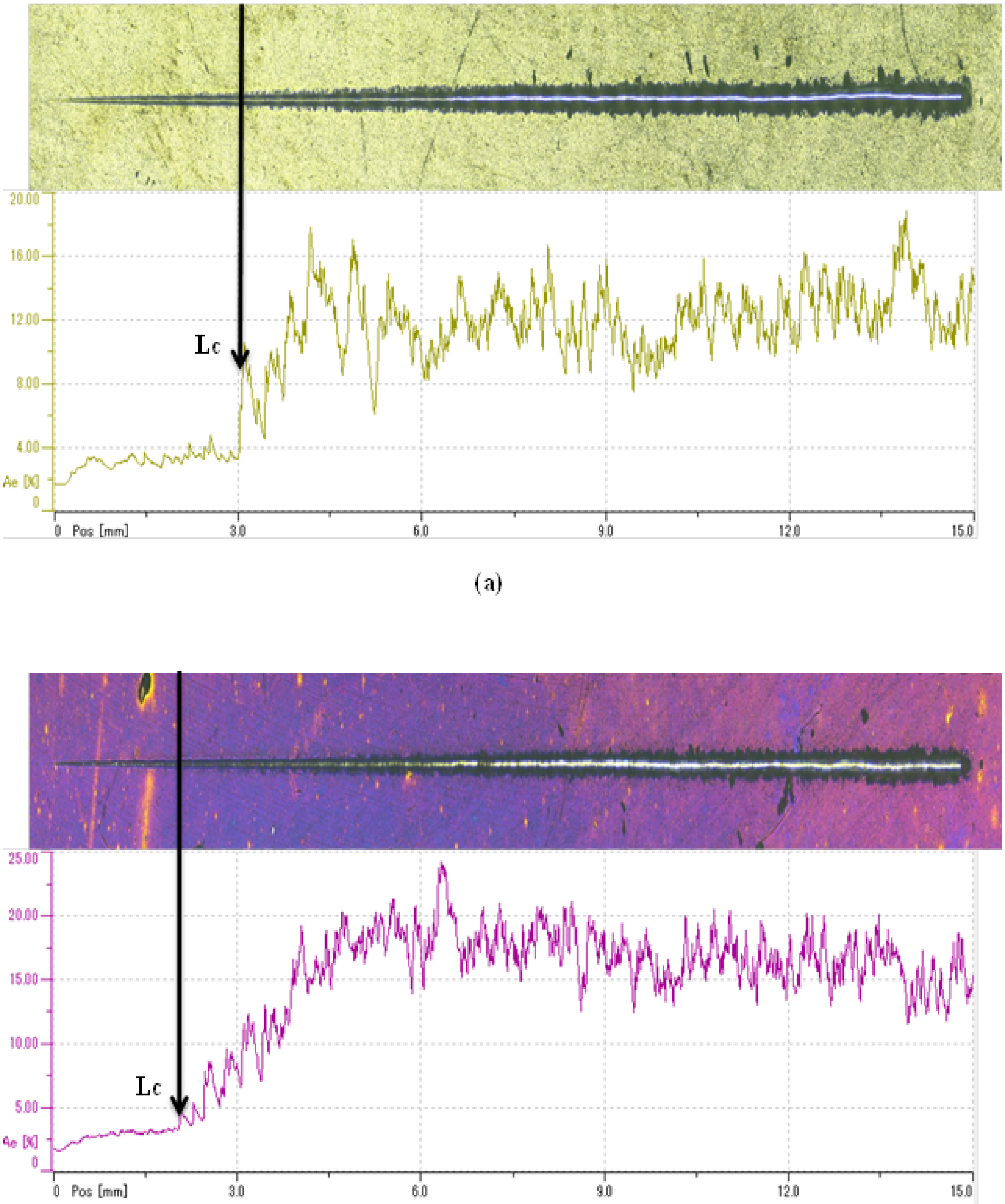

(a)

(b)

Figure 4.29: Scratch track of (a) CrAlN and (b) TiAlN coatings after annealing at 800^oC for 2 hours

Table 4.6: Mechanical Properties of the four nitride coatings after annealing at 800^oC for 2hours

	Hardness (Hv)	Modulus (GPa)	Critical load (N)	Friction Coefficient (μ)	Crystallite Size (nm)	Residual Stress (GPa)
CrN	1230 ± 37	228 ± 15	7.2 ± 0.2	0.22 ± 0.01	134 ± 6	-3.32
TiN	1558 ± 30	282 ± 32	3.0 ± 0.1	0.13 ± 0.02	166 ± 3	-8.20
CrAlN	2225 ± 102	277 ± 18	6.1 ± 0.5	0.20 ± 0.05	147 ± 6	-23.22
TiAlN	1778 ± 96	256 ± 6	4.9 ± 0.7	0.19 ± 0.03	119 ± 5	-43.08

CHAPTER 5

DISCUSSIONS

5.1 Microstructural Characterization

This section discusses the compositional and microstructural characteristics of the various coatings deposited by cathodic arc using the XRD and SEM. These analytical results were used to characterize the observed trends for microhardness, scratch, creep and solid particle erosion. From these correlations, general trends were observed that suggest how to optimize the cathodic arc deposition conditions for development of solid particle erosion resistant coatings with improved performance.

5.1.1 Morphology

Irregularities of surface (Figure 4.1) are typical for arc evaporation and they are due to the incorporation of macroparticles. Macroparticles are composed mainly of unreacted target material [11] and, in the case of TiN films, can range in size from a few hundred nanometers to several micrometers, depending on deposition conditions. These droplets are deleterious to the performance of the coating as they are poorly adhered and can extend through the coating [40].

SEM micrographs of the coated surfaces are shown in Figure 4.1. The mean resident time of the cathodic arc spot is very instrumental in macroparticle emission. Low resident mean time of the cathodic spot owing to the higher arc spot velocity causes individual evaporation events on the target surface to have insufficient time for any significant localized heating of material to be melted and thus emitted in the form of macro droplets. This is consistent with an observed pattern in performance of the arc source. Low melting point materials such as Al have been observed to emit relatively large number of macroparticles [41, 42].

5.1.2 Composition

The average elemental compositions of the coatings are presented in Table 4.1. The stoichiometric phases of the binary nitride coatings are CrN and TiN. The ternary nitride coatings have the stoichiometric ratios as $Cr_{0.33}Al_{0.67}N$ and $Ti_{0.5}Al_{0.5}N$ for $CrAlN$ and $TiAlN$ coating systems, respectively.

The atomic ratio Cr/Al was 1 : 2 whereas Ti/Al was 1 : 1. It was predicted by Chen et. al [32] that AlN shows the highest solubility in CrN among various transition metal nitrides with fcc crystal structure. The solubility of AlN in CrN was shown to be 77.2% and that of AlN in TiN was 65.3% [32].

The atomic ratios of the alloyed target materials in this study were 1 : 4 and 1 : 2

for Cr/Al and Ti/Al targets, respectively. The resulting coatings showed a lower ratio as compared to their respective target materials and this was attributed to resputtering during deposition and growth [43].

5.1.3 Crystallographic Structure

The $\theta/2\theta$ patterns of the four nitride coatings are shown in Figure 4.2. Significant information on the crystal structure and crystallographic orientation of the coatings were provided by the XRD pattern.

All four of the XRD patterns were identified as the $B1$ $NaCl$ structure [44, 45, 46]. The stoichiometric phase of CrN and TiN with $B1$ $NaCl$ crystal structure occurs only in a limited range of nitrogen pressure. The cubic structures of $CrAlN$ and $TiAlN$ was expected because the $x = 0.67$ in $Cr_{(1-x)}Al_xN$ and $x = 0.5$ in $Ti_{(1-x)}Al_xN$ are less than the critical value for its crystalline structure to be changed from $B1$ to $B4$. The critical value was reported to be around 0.75 [32].

The diffraction peaks are shifted relative to the standard data of CrN and TiN as presented in Figure 4.2. This shift can be caused by residual stresses in the layer which were generated by ion bombardment during deposition and coefficient of thermal expansion mismatch between the substrate and coatings during cooling [40]. Any factor that changes the lattice parameters of crystalline materials can also distort their XRD spectra. Peak shifts in spectra occur when there is residual stress in a sample. Residual stress generates strain in the coatings by stretching or compressing bonds between the atoms. Thus, the spacing of crystallographic planes changes due to residual stress. When the spacing of the crystallographic plane changes, the Braggs angle should either increase or decrease. The residual stress, tensile in nature increases the atomic spacing thereby shifting the 2θ to a lower value whereas compressive residual stresses decrease the atomic spacing thereby shifting the 2θ to a higher value. It was also reported that the peak positions of a $CrAlN$ and $TiAlN$ coating may shift to higher angles compared to their standard 2θ positions because of a possible decrease in the lattice parameter of the coating structure caused by the partial replacement of Cr atoms with smaller sized Al atoms. Thus, the observed peak shifts could result from a combined effect of both residual stress and Al substitution [47]. The high intensity peak centered at 43.34^o was indexed to cubic CrN $\{200\}$, $CrAlN$ $\{200\}$ and $TiAlN$ $\{200\}$ planes, the peak with a lower intensity at 37.20^o was indexed to cubic CrN $\{111\}$, $CrAlN$ $\{111\}$ and $TiAlN$ $\{111\}$ planes. Other high angle reflections such as $\{220\}$ and $\{311\}$ were clearly shown. For TiN coating, the peak corresponding to $\{111\}$ planes was shifted to 35.12^o [41]. The peaks from the substrate overlapped that of the coatings at $\{200\}$ and $\{311\}$. Similar results were observed in coatings on stainless steel substrates [30]. For TiN the peak at $\{222\}$ was distinct from that of the substrate. The high bias voltage during deposition process resulted in high atom mobility and increased surface diffusion, which could facilitate alignment of the growth along the [200] direction for CrN, $CrAlN$ and $TiAlN$. TiN on the other hand was highly oriented in [111] direction [48, 49].

5.2 Mechanical and Tribological Characterization

5.2.1 Microhardness

The measured microhardness and modulus for the four nitride coatings, which were averaged from 10 measurements, are summarized in Table 4.2. The uncoated 304 stainless steel has a hardness of 330 Hv. The hardness of $CrAlN$ coating reached $2400HV$ that is about 700% increase compared to that of 304 stainless steel substrate; while CrN with the lowest hardness among the four nitride coatings increased the hardness to about 370% compared to the substrate. The penetration depths of the coatings at 20mN load were 160 nm, 130 nm, 106 nm and 119 nm, for CrN, TiN, $CrAlN$ and $TiAlN$, respectively and is about one-tenth of the average film thickness. Thus, the hardness of the coatings measured at the $20mN$ load therefore reflects the intrinsic property of the film with minimal substrate effect [49].

Vickers microhardness summarized in Table 4.2 shows that $CrAlN$ and $TiAlN$ are significantly harder than TiN, which is also harder than CrN. The hardness enhancement of the ternary nitride coatings was probably due to solid solution strengthening and the internal stresses arising from the partial replacement of the chromium and titanium atoms in the CrN and TiN lattice by the aluminum atoms. $CrAlN$ contains higher Al as compared to $TiAlN$ and hence higher hardness.

The indentation modulus of all coatings were in the range of $187 - 342$ GPa. The microstructure and internal stress levels in the coatings could affect the hardness of the coatings [50].

5.2.2 Scratch

The onset of coating failure during scratch was determined from the acoustic emission signal which was characterized by a sudden increase in the acoustic signal as illustrated in Figures 4.5 and 4.6. Acoustic emission signal spike was matched to the point of failure of the coating by utilizing an optical microscope attached to the equipment. The critical loads of the coatings averaged after three different scratches were in the range of $3.50 - 7.40$N and are summarized in Table 4.3.

The damages encountered during the scratch test were typically cohesive failure in the form of tensile and conformal cracks coupled with chipping at the edges of the scratch track. Spallation and delamination has not been observed in any of the coating.

There are two main factors that affect the critical load of a coating namely intrinsic and extrinsic factors. The intrinsic factors are those factors that are inherent to the test procedure whereas the extrinsic factors are those that depend on both the coating and the substrate system. The intrinsic parameters are the scratch speed, loading rate, indenter tip radius, and instrument compliance. The extrinsic factors are substrate properties (hardness, modulus, roughness, coefficient of thermal expansion) and coating properties (hardness, modulus, thickness, roughness, and friction coefficient, residual stress and interfacial properties) [51].

SEM micrographs of the scratch track are illustrated in Figures 4.7 and 4.8. The failure mechanism of coatings are usually a complex phenomenon and generally more than one failure mechanisms exist in a single coating.

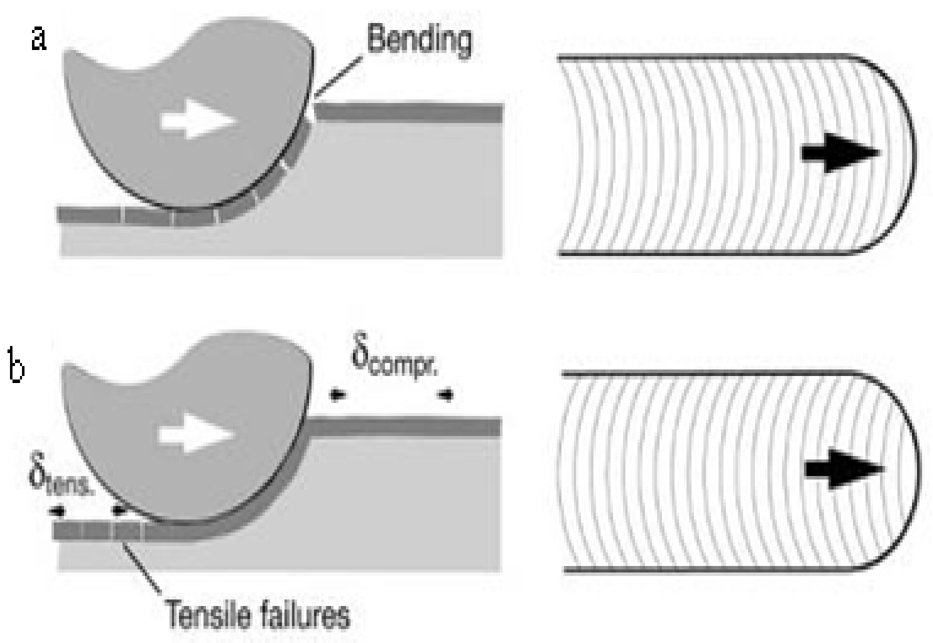

Figure 5.1: Schematics of conformal and tensile modes of failure during scratch.

The predominant failure mechanism observed in all the coatings was cohesive failure that manifested as tensile cracks in CrN, TiN and $CrAlN$ and manifested as compressive or conformal cracks in $TiAlN$. The schematics of the predominant failure modes are illustrated in Figure 5.1. Figure 5.1a shows conformal cracks that were generated due to high compressive stresses at the leading edge of the indenter while Figure 5.1b shows tensile cracks that were generated due to the high tensile stresses at the trailing edge of the indenter.

A partial cone crack initiates due to maximum tensile stresses at the trailing edge of the indenter. The formation of these partial cone cracks repeats with a regular interval as illustrated in Figure 5.1. Close observation of the SEM micrographs of the scratch track illustrated in Figures 4.7 and 4.8 shows similar trend in the repeatability of the cracks. The tensile stress intensified at the trailing edge due to the sliding contact whereas it was reduced at the leading edge of the scratch tip. This manifests as semicircular cracks that propagates outward of the crack centerline. This results in chipping of the coating along the edges of the scratch track. CrN was characterized by extensive tensile cracks as illustrated in Figure 4.7a. These cracks extend beyond the scratch track and are perpendicular to the scratch direction with less curvature. For TiN and $CrAlN$ the tensile cracks were mainly confined to the scratch track with few extensions beyond the scratch track as illustrated in Figures 4.7b and 4.7c. Compressive or conformal cracks in $TiAlN$ coating were due to buckling of the coating at the leading edge of the indenter with no observable delamination as illustrated in Figure 4.7d. This mode of failure is generally characterized by semicircular cracks in a direction opposite to that of scratch with chippings that are confined to the scratch track. Buckling of the coating occurs at the leading edge of the indenter due to the pile up of soft substrate material ahead of the indenter and the high compressive forces caused by tangential friction. There was formation of considerable amount of grooves as the indenter traverses the coating over the ductile substrate since the substrate deforms underneath the coating. This leads to the coating being cracked as it bends into the groove created by the deforming substrates under the scratch track thereby conforming to the groove. Also there was rounded region of coating removal extending laterally from the edges of the scratch groove and was found to be due to chipping. The images were further magnified to show the various modes of failure in 4.8.

The coefficient of friction for the coatings were determined up to the critical load for each coating as illustrated in Figure 4.9. This was done to prevent the cracks developed beyond the critical load from influencing the coefficient of friction value. The coefficient of friction values ranged from 0.19 for $TiAlN$ to 0.24 for TiN. Coefficient of friction for CrN and $CrAlN$ were 0.21 and 0.19 respectively.

5.2.3 Creep

Indentation data obtained at 50^oC, 75^oC and 100^oC are presented in Figures 4.10 to 4.15. The methodology employed in obtaining steady-state creep parameters from the indentation data followed the works of Mayo and Nix [16], Bower et al [52], Goodall and Clyne [17], and Choi et al [12]. It was based on the assumption that the stress and strain rate fields are similar, thus while the values of stress and strain at each point changes during deformation, the ratios between values at different points in the field will remain constant. The strain rates were therefore evaluated from the slopes of the plot of penetration depth with holding time at $15mN$, $20mN$ and $25mN$ for all the coatings using equation 2.3. The variation in penetration depth with load-holding time is illustrated in Figures 4.12 to 4.15. The strain rates obtained are shown in Table 4.4. The strain rate was shown to generally decrease with increasing penetration rate as the mean stress under the tip of the indenter decreases. The maximum strain rate occurred at the onset of creep during the beginning of the hold period and gradually decreases as the penetration depth increases until the coating deforms. As the temperature increases the hardness of the coatings decreases leading to an increased penetration depth and hence decreased creep rate. This phenomenon is consistent with early works in indentation creep assuming a steady state creep during the hold period [12, 17, 52, 53]. There are local variations in the strain rate from load to load due to the local variations on the surface of the coatings and the variation in concentration of macroparticles as well. The activation energy necessary for creep to occur were calculated from a semi logarithm plot of strain rate and inverse of temperature. These are illustrated in Figures 4.16 and 4.17 for CrN, TiN, CrAlN and TiAlN coatings. The stress exponent was also evaluated from a log-log plot of the strain rate and the mean stress as illustrated in Figures 4.18 and 4.19. The obtained values of the stress exponent are presented in Table 4.5. It was not possible to compare the activation energy and the stress exponent to other published works for the four coatings as they are not available. The stress exponents values obtained are consistent with a creep mechanism due to diffusion [54, 55]. $CrAlN$ and $TiAlN$ are highly resistant to creep deformation as compared to their binary counterparts. TiN showed significant resistance to creep as compared to CrN that showed the least resistance among the four coatings under investigation. The substitution of some of the Cr and Ti atoms to form $CrAlN$ and $TiAlN$ solid solution led to an increase in the dislocation density [32]. The increased dislocation density intend made diffusion much difficult and hence the high activation energy. $CrAlN$ exhibited the highest resistance to creep as the percentage of aluminum in $CrAlN$ is much higher than that of $TiAlN$ and hence the corresponding high activation energy.

5.2.4 Erosion

The performance of the coatings when subjected to solid particle erosion was evaluated using angular alumina particles shown in Figure 4.20 at a particle velocity of 60 m/s. The high hardness and angularity of alumina particles provided a severe environment for erosion to take place.

The erosion rates for hard coatings are commonly expressed in terms of mass loss per unit mass of erodent as shown in Figures 4.21 and 4.22. It can be seen that the overall erosion rates for the ternary nitride coatings ($CrAlN$ and $TiAlN$) are significantly lower, at various impingement angles, than those for the binary nitride coatings (CrN and TiN). This is mainly due to the mechanical properties, specifically higher hardness and elastic modulus.

Initial assessments during the early stages of erosion (150 seconds)reveal that the mass loss was not linear with erodent mass as shown in Figure 4.21 as compared to the intermediate stage (600 seconds) in which the mass loss increased linearly with erodent mass with a correlation factor between 0.94 and 0.99 as illustrated in Figure 4.22.

For the intermediate erosion testing, the ability of the coatings to retard further damage was considered as the substrate was already exposed in the center of the erosion scar. TiN, $CrAlN$ and $TiAlN$ showed excellent resistance in this regard as there was no further increase in the size of the erosion scar when compared to the early erosion operation whereas CrN exhibited continued damage with significant increase in the size of the erosion scar which was similar to that of the substrate. After 600 seconds erosion operation it was observed that there was a complete coatings removal from the substrate in all four coatings.

The morphology of the coatings before erosion operation is illustrated in Figure 4.1. The morphology of the erosion scar after 150 seconds erosion operation was studied at 30^o and 90^o impingement angles for each coating. Figures 4.24a and 4.25b shows extruded regions and deformation scratches at 30^o and craters at 90^o for CrN coating. The images were taken at the center of the erosion scar. At 30^o impingement angle there was a localized breakdown of the CrN coating as illustrated in Figure 4.24a. Figures 4.24c and 4.24d showed ploughed surfaces at 30^o and some craters on the surface at 90^o impingement angles for TiN coating. Figures 4.25a and 4.25b show ploughed surface with pits at 30^o and craters on the surface at 90^o for $CrAlN$ coating. Figures 4.25c and 4.25d show ploughing of the surface at 30^o and formation of craters on the surface at 90^o for $TiAlN$ coating. For the substrate it was observed that there was formation of craters and extruded regions at both 30^o and 90^o impingement angles as shown in Figure 4.26.

TiN, $CrAlN$ and $TiAlN$ coatings were still intact after the 150 seconds operation. There was no indication of brittle failure or crack at both 30^o and 90^o impingement angles. Material degradation through plastic deformation was observed under both conditions. The micrographs in Figure 4.24 and 4.25 show similar deformation mechanism as that of 304 stainless steel substrate in Figure 4.26.

The coatings undergo elasto-plastic indentation forming lips at the edges of the impact zone. These lead to material removal upon subsequent impacts through plastic cutting. This was because the substrates being ductile has effect on the thin coating. Deformation by ploughing was also observed as the coatings are being pushed ahead of grooves and pits formed by the impacting erodent particles. Two important parameters of the coatings that were suggested to affect the erosion rates are the hardness, H, and H^3/E^2, which is the resistance of a material to the onset of plastic deformation. The degree of correlation between the erosion rate and coatings parameter (H and H^3/E^2) was examined by plotting the erosion rates obtained with the coating parameters and fitted with an exponential function to obtain the dependency coefficient (r^2). Figure 5.2a illustrates the correlation of the hardness with erosion rates at 30^o and 90^o impingement angles. The dependency coefficient (r^2) obtained was $r^2 = 0.983$ at 90^o and $r^2 = 0.992$ at 30^o. The effect of the hardness on erosion was therefore represented by the function, Erosion rate $\propto e^{(-(0.2\pm0.04)H)}$. It was observed that the erosion rate decreases with increasing H^3/E^2 as illustrated in Figure 5.2b. This shows that the erosion rates were highly influenced by the degree of plastic deformation.

The effect of the impingement angle on the erosion rate of the coatings tested are presented in Figure 4.23 for early and intermediate assessments respectively. $TiAlN$ and $CrAlN$ were the best performing coatings against erosion for both 150 and 600 seconds erosion tests while CrN was the least. AISI 304 stainless steel has the highest erosion rates at low impingement angles but was much more resistant at higher angles far more than CrN.

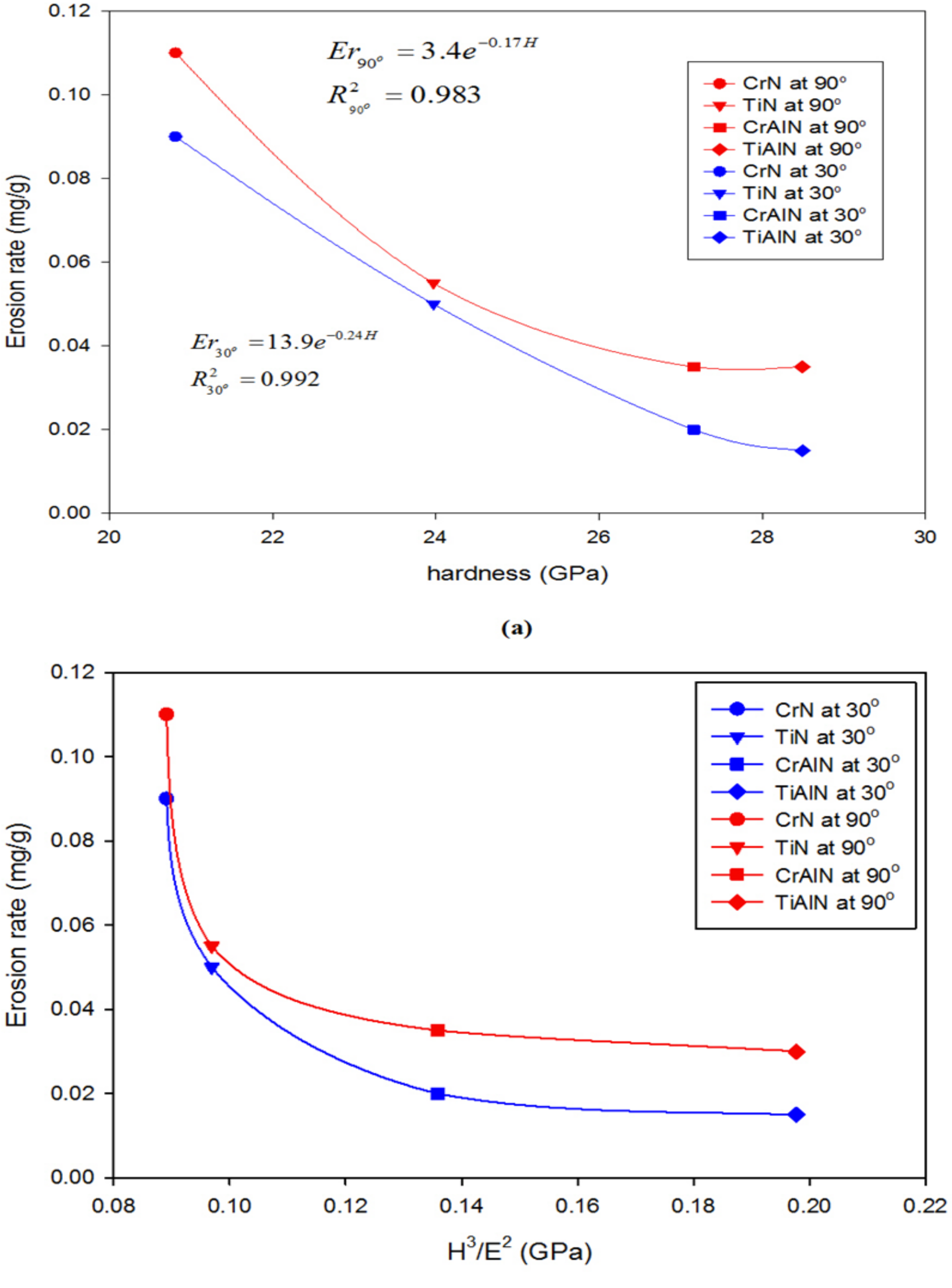

(a)

(b)

Figure 5.2: Variations of erosion rate with materials parameters (a) Hardness (b) H^3/E^2

5.2.5 Effect of Residual Stress

The XRD patterns of the coatings after being annealed at 800^oC are illustrated in Figure 4.27. Oxide scales were formed on CrN and TiN coatings. Cr_2O_3 peaks were observed in the XRD peaks for CrN coating whereas TiO_2 was observed for that TiN coating. The oxide peaks were distinctly identified as shown in Figure 4.27. $CrAlN$ and $TiAlN$ were not oxidized at this temperature.

It was also observed from the XRD results that there was no decomposition of any of the coatings and the crystal structure was FCC with $B1$ $NaCl$ structure. The crystallite size of the coatings after annealing were in the range of $110 - 170$ nm as presented in Table 4.6. TiN has largest crystallite size whereas $TiAlN$ has the least.

The residual stress evaluated from the XRD spectra illustrated in Table 4.5 shows that all four coatings possess compressive residual stresses. The residual stresses were in range of -3 to -43. The evaluated residual stress comprised of intrinsic stress resulting from the coating growth stage and thermal stress arising from the coefficient of thermal expansion mismatch between the coating and the substrate cooling from the deposition temperature.

The mechanical properties of the coatings were also evaluated after annealing as presented in Table 4.5. The hardness of the coatings were marginally affected as compared to the as deposited coatings shown in Table 4.2. The hardness of CrN and TiN were marginally reduced from 1236 to $1230Hv$ and 1591 to 1558 Hv respectively. $CrAlN$ and $TiAlN$ had their hardnesses slightly reduced from

2417 to 2225 Hv and 1926 to 1778 Hv respectively. However the modulus of elasticity was slightly increased for CrN and TiN from 187 and 242 GPa for the as deposited coatings to 228 and 282 GPa, respectively. $CrAlN$ and $TiAlN$ had their moduli reduced.

The critical loads after scratch test were in the range of $3.0 - 7.2N$ which were similar to the as deposited coatings. The critical load of CrN increases from $5.5N$ for the as deposited coating to $7.2N$ for the annealed coating. Similarly the as deposited $CrAlN$ has a critical load of $4.8N$ and this has increased to $6.1N$ for the annealed $CrAlN$ whereas the critical load for the as deposited $TiAlN$ increases from $3.5N$ to $4.9N$. The critical load was enhanced for the ternary coatings after annealing due to the relieving of the high copmpressive stresses in them while the formation of oxides on the binary coatings degrades the scratch resistance. The coefficient of friction after annealing followed similar trend as the as deposited coatings. Annealed CrN with the highest critical load also recorded the highest coefficient of friction whereas annealed TiN with the least critical load recorded the lowest coefficient of friction. Annealing the coatings at 800^oC does not have much influence the hardness as opposed to that of scratch resistance of the coatings.

CHAPTER 6

CONCLUSIONS

The focus of this study was to evaluate the mechanical properties,indentation creep and erosion resistance of cathodic arc deposited CrN, TiN, $CrAlN$ and $TiAlN$ coatings. The following conclusions can be drawn:

1. The four nitride coatings showed the B1 NaCl crystal structure. CrN, CrAlN and TiAlN revealed (200) preferred crystallographic texture while TiN exhibited (111) preferred texture.
2. The hardness of the coatings measured using 20mN load revealed that ternary coatings had higher hardness as compared to their binary counterparts. CrN exhibited the least hardness whereas CrAlN exhibited the highest. The high hardness of CrAlN compared to that of TiAlN was attributed to the higher content of Al in CrAlN.
3. The scratch resistance of the coatings evaluated from the critical load values showed that the binary nitride coatings (CrN and TiN) were better as

compared to the ternary nitride coatings. The coatings ranked in the order highest to lowest as TiN, CrN, CrAlN and TiAlN.

4. There was no indication of any brittle failure mechanism. The predominant failure mechanism observed in all four coatings was ductile failure. This failure was manifested in CrN, TiN and CrAlN as tensile cracks whereas in TiAlN it was dominated by conformal cracks.

5. The ternary coatings (CrAlN and TiAlN) exhibited higher activation energies as compared to their binary counterparts.

6. A typical stress exponents obtained within $50 - 100^oC$ showed that the dominant creep mechanism was that due to diffusion. CrAlN exhibited the highest creep resistance whereas CrN exhibited the least.

7. CrAlN and TiAlN coatings showed higher erosion resistance as compared to CrN and TiN.

8. It was observed that the addition of Al to CrN and TiN enhanced the erosion performance. $CrAlN$ and $TiAlN$ coatings showed higher erosion resistance as compared to CrN and TiN.

9. XRD patterns of the annealed coatings showed that there was no decomposition at the annealed temperature and the coatings possessed B1 NaCl crystal structure. Oxide scales were formed on the binary coatings (CrN and TiN) but none was observed in the XRD peak of the ternary coatings.

REFERENCES

[1] V. Vishnyakov, V. Bachurin, K. Minnebaev, R. Valizadeh, D. Teer, J. Colligon, V. Vishnyakov, and V. Yurasova, “Ion assisted deposition of titanium chromium nitride,” *Thin Solid Films*, vol. 497, no. 1-2, pp. 189–195, Feb. 2006.

[2] MDS Coating technology Corporation, “Protective Coatings for Compressors,” in *Sea King Symposium*, 2013.

[3] O. Knotek, F. Loffler, and H. Scholl, “Properties of arc-evaporated CrN and (Cr, Al)N coatings,” pp. 53–58, 1991.

[4] W. Tabakoff, “Protection of coated superalloys from erosion in turbomachinery and other systems exposed to particulate flows,” *Wear*, vol. 233-235, pp. 200–208, Dec. 1999.

[5] A. Andre, “Cathodic Arcs,” in *A joint worksop of Belgian and French Vacuum Society*, 2003, pp. 1–12.

[6] G. Erkens, J. Vetter, J. Muller, T. auf dem Brinke, M. Fromme, and A. Mohnfeld, *Plasma-Assisted Surface Coating- Processes, methods, systems and applications*, 2011.

[7] D. M. Sanders and A. Anders, "Review of cathodic arc deposition technology at the start of the new millennium," *Surface and Coatings Technology*, vol. 133-134, pp. 78–90, Nov. 2000.

[8] R. Boxman and S. Goldsmith, "Principles and applications of vacuum arc coatings," *IEEE Transactions on Plasma Science*, vol. 17, no. 5, pp. 705–712, 1989.

[9] H. Randhawa, "Cathodic arc plasma deposition technology," *Thin Solid Films*, vol. 167, no. 1-2, pp. 175–186, 1988.

[10] P. J. Martin and A. Bendavid, "Review of the filtered vacuum arc process and materials deposition," *Thin Solid Films*, 2001.

[11] B. Tay, Z. Zhao, and D. Chua, "Review of metal oxide films deposited by filtered cathodic vacuum arc technique," *Materials Science and Engineering: R: Reports*, vol. 52, no. 1-3, pp. 1–48, May 2006.

[12] I.-C. Choi, B.-G. Yoo, Y.-J. Kim, and J.-i. Jang, "Indentation creep revisited," *Journal of Materials Research*, vol. 27, no. 01, pp. 3–11, Aug. 2011.

[13] O. D. Sherby and P. E. Armstrong, "Prediction of Activation Energies for Creep and Self-Diffusion from Hot Hardness Data," *Metallurgical Transactions*, 1971.

[14] D. S. Stone, J. E. Jakes, J. Puthoff, and A. a. Elmustafa, “Analysis of indentation creep,” *Journal of Materials Research*, vol. 25, no. 04, pp. 611–621, Jan. 2011.

[15] W. B. LI, J. L. Henshall, R. Hooper, and K. Easterling, “The mechanisms of indentation creep,” *Acta Metall. mater.*, vol. 39, no. 12, pp. 3099–3110, 1991.

[16] M. J. Mayo, R. W. Siegel, A. Narayanasamy, and W. D. Nix, “Mechanical properties of nanophase TiO2 as determined by nanoindentation,” *Journal of Materials Research*, 1990.

[17] R. Goodall and T. Clyne, “A critical appraisal of the extraction of creep parameters from nanoindentation data obtained at room temperature,” pp. 5489–5499, 2006.

[18] W. R. Lafontaine, B. Yost, and R. D. Black, “Indentation load relaxation experiments with indentation depth in the submicron range,” *Journal of Materials Research*, vol. 14853, no. March, 1990.

[19] J. Bitter, “A study of erosion phenomena,” *Wear*, vol. 6, no. 3, pp. 169–190, 1963.

[20] I. Finnie, “Some observations on the erosion of ductile metals,” *Wear*, vol. 19, no. 1, pp. 81–90, Jan. 1972.

[21] I. Finnie, G. Stevick, and J. Ridgely, “The influence of impingement angle on the erosion of ductile metals by angular abrasive particles,” *Wear*, vol. 152, no. 1, pp. 91–98, Jan. 1992.

[22] W. G. Stachowiak and W. A. Batchelor, *Engineering Tribology*, 4th ed. Elsevier, 2014, vol. Volume 24.

[23] S. Jahanmir, “The mechanics of subsurface damage in solid particle erosion,” *Wear*, vol. 61, pp. 309–324, 1980.

[24] J. A. Williams and F. E. Kennedy, “Engineering Tribology,” 1998.

[25] J. Malik, I. H. Toor, W. H. Ahmed, Z. M. Gasem, M. a. Habib, R. Ben-Mansour, and H. M. Badr, “Evaluating the effect of hardness on erosion characteristics of aluminum and steels,” *Journal of Materials Engineering and Performance*, vol. 23, no. 6, pp. 2274–2282, 2014.

[26] G. D’Errico, S. Bugliosi, and D. Cuppini, “Performance of ceramics in erosion tests by solid particle impingement,” *Journal of Materials Processing Technology*, vol. 64, no. 96, pp. 85–92, 1997.

[27] A. V. Levy and W. Buqian, “Erosion of hard material coating systems,” *Wear*, vol. 121, no. 3, pp. 325–346, 1988.

[28] Q. Yang, D. Seo, L. Zhao, and X. Zeng, “Erosion resistance performance of magnetron sputtering deposited TiAlN coatings,” *Surface and Coatings Technology*, vol. 188-189, pp. 168–173, Nov. 2004.

[29] B. Jonsson, L. Akre, S. Johansson, and S. Hogmark, “EVALUATION OFHARDCOATINGSON STEEL BY PARTICLE,” *Thin Solid Films*, vol. 137, pp. 65–77, 1986.

[30] J. Sue and H. Troue, “Influence of residual compressive stress on erosion behavior of arc evaporation titanium nitride coating,” *Surface and Coatings Technology*, vol. 36, no. 3-4, pp. 695–705, 1988.

[31] M. Bromark, P. Hedenqvist, and S. Hogmark, “The influence of substrate material on the erosion resistance of TiN coated tool steel,” *Wear*, vol. 186187, pp. 189–194, 1995.

[32] L. Chen, Y. Du, S. Wang, and J. Li, “A comparative research on physical and mechanical properties of (Ti, Al)N and (Cr, Al)N PVD coatings with high Al content,” *International Journal of Refractory Metals and Hard Materials*, vol. 25, no. 5-6, pp. 400–404, Sep. 2007.

[33] S. PalDey and S. Deevi, “Properties of single layer and gradient (Ti,Al)N coatings,” *Materials Science and Engineering: A*, vol. 361, no. 1-2, pp. 1–8, Nov. 2003.

[34] J. Romero, M. Gómez, J. Esteve, F. Montalà, L. Carreras, M. Grifol, and A. Lousa, “CrAlN coatings deposited by cathodic arc evaporation at different substrate bias,” *Thin Solid Films*, vol. 515, no. 1, pp. 113–117, Sep. 2006.

[35] E. Spain, J. Avelar-Batista, M. Letch, J. Housden, and B. Lerga, “Characterisation and applications of CrAlN coatings,” *Surface and Coatings Technology*, vol. 200, no. 5-6, pp. 1507–1513, Nov. 2005.

[36] M. Doerner and W. Nix, “A method for interpreting the data from depth-sensing indentation instruments,” *Journal of Materials Research*, 1986.

[37] W. Oliver and G. Pharr, “An improved technique for determining hardness and elastic modulus using load and displacement sensing indentation experiments,” *Journal of materials research*, 1992.

[38] J. R. Laguna-camacho, “Solid Particle Erosion on Different Metallic Materials,” 2013.

[39] A. Ruff and L. Ives, “Measurement of solid particle velocity in erosive wear,” *Wear*, vol. 35, no. 1, pp. 195–199, 1975.

[40] B. Warcholiski, a. Gilewicz, Z. Kukliski, and P. Myśliski, “Arc-evaporated CrN, CrN and CrCN coatings,” *Vacuum*, vol. 83, no. 4, pp. 715–718, Nov. 2008.

[41] P. C. Johnson, H. Randhawa, and V.-t. Systems, “Zirconium nitride films prepared by cathodic arc plasma deposition process*,” *Surface and Coatings Technology*, vol. 33, pp. 53–62, 1987.

[42] J. Vetter, E. Lugscheider, and S. Guerreiro, “(Cr:Al)N coatings deposited by the cathodic vacuum are evaporation,” *Surface and Coatings Technology*, vol. 98, no. 1-3, pp. 1233–1239, Jan. 1998.

[43] A. Vlasveld, S. Harris, E. Doyle, D. Lewis, and W. Munz, “Characterisation and performance of partially filtered arc TiAlN coatings,” *Surface and Coatings Technology*, vol. 149, no. 2-3, pp. 217–223, Jan. 2002.

[44] J. Deng, F. Wu, Y. Lian, Y. Xing, and S. Li, "Erosion wear of CrN, TiN, CrAlN, and TiAlN PVD nitride coatings," *International Journal of Refractory Metals and Hard Materials*, vol. 35, pp. 10–16, Nov. 2012.

[45] H. C. Barshilia, N. Selvakumar, B. Deepthi, and K. Rajam, "A comparative study of reactive direct current magnetron sputtered CrAlN and CrN coatings," *Surface and Coatings Technology*, vol. 201, no. 6, pp. 2193–2201, Dec. 2006.

[46] R. R. Aharonov, B. F. Coll, and R. P. Fontana, "Properties of chromium nitride coatings deposited by cathodic arc evaporation," *Surface and Coatings Technology*, vol. 61, no. 1-3, pp. 223–226, 1993.

[47] L. Wang, X. Nie, J. Housden, E. Spain, J. Jiang, E. Meletis, A. Leyland, and A. Matthews, "Material transfer phenomena and failure mechanisms of a nanostructured CrAlN coating in laboratory wear tests and an industrial punch tool application," *Surface and Coatings Technology*, vol. 203, no. 5-7, pp. 816–821, Dec. 2008.

[48] F. Cai, "Tribological and Electrochemical Corrosion Behaviours of Titanium Nitride and Chromium Nitride Based PVD Coating Systems," Ph.D. dissertation, Carleton University, 2011.

[49] J.-n. Tu, J.-g. Duh, and S.-y. Tsai, "Morphology , mechanical properties , and oxidation behavior of reactively sputtered Cr N films," *Surface and Coatings Technologyy*, vol. 133-134, pp. 181–185, 2000.

[50] W. Herr, B. Matthes, E. Broszeit, M. Meyer, and R. Suchentrunk, "Influence of substrate material and deposition parameters on the structure, residual stresses, hardness and adhesion of sputtered CrxNy hard coatings," *Surface and Coatings Technology*, vol. 60, no. 1-3, pp. 428–433, 1993.

[51] B. M. Gabriel, "Synthesis-structure-property-performance relationships of TiN,CrN, and nanolayer (Ti,Cr)N coatings deposited by cathodic arc evaporation for hard particle erosion resistance," Ph.D. dissertation, The Pennsylvania State University, 2009.

[52] A. F. Bower, N. A. Fleck, A. Needleman, and N. Ogbonna, "Indentation of a power law creeping solid," *Proc. R. Soc. London. A*, 1993.

[53] A. El-Bediwi, K. Ismail, and M. Kamal, "Microstructure , indentation creep and mechanical properties of Sn-Sb rapidly solidified alloys," *Materials Science*, pp. 1–6, 2012.

[54] C. Su, "Measurement Of Power-law Creep Parameters By Instrumented Indentation Methods," Ph.D. dissertation, 2012.

[55] M. E. Kassner and M.-T. Pérez-Prado, *Fundamentals of Creep in Metals and Alloys.* Elsevier, 2004.

Vitae

- Name: **Nestor Kodzo Ankah**
- Nationality: **Ghanaian**
- Date of Birth: **16th December,1985**
- Email: *ankahnestor@yahoo.com*
- Permenant Address: **Selase Villa, Box HP 809, Ho, Ghana**

Education and Qualifications

- Name of Institution: **King Fahd University of Petroleum & Minerals, Dhahran, Saudi Arabia**

  Title of qualification awarded: **MSc Materials Sci & Engineering**

  Year: **January 2013-May 2015**

- Name of Institution: **Kwame Nkrumah University of Science and Technology, Kumasi, Ghana**

  Title of qualification awarded: **BSc. Materials Engineering**

  Year: **August 2005-June 2009**

Work History

- **September 2010-December 2012**

  Job Title: **Production Supervisor**

  Organization: **Blue Sea Ltd, Accra, Ghana**

  Key Roles And Responsibilities: **Supervises the day to day production of detergents**.

- **August 2009-July 2010**

  Job Title: **Teaching/Research Assistant**

  Organization: **Kwame Nkrumah University of Science And Technology, Kumasi, Ghana.**

  Key Roles And Responsibilities: **Organize tutorials, mark assignments and undertake laboratory works and research**

Publication

- **Scratch and Erosion resistance of CrN, CrAlN, TiN and TiAlN coatings deposited by Cathodic Arc Evaporation, Surface and Coatings technology, Submitted, April 2015.**